Summer 7-16-2021

The Impacts of Climate and Landscape Change on Catchment Scale Material Transport in High Mountain and Seasonally Cold Regions

John R. Slosson
Syracuse University

Recommended Citation

Slosson, John R., "The Impacts of Climate and Landscape Change on Catchment Scale Material Transport in High Mountain and Seasonally Cold Regions" (2021). *Dissertations - ALL*. 1534.
https://surface.syr.edu/etd/1534

General Abstract

Streamflow in high mountain and seasonally cold regions follows annual patterns that can make water quality and availability in these areas uniquely susceptible to changes in climate and land use. Precipitation in the form of snow accumulates during the winter months and gradually melts in the spring, leading to elevated streamflow that serves important ecological and human needs. This simple winter storage and spring release dynamic is especially sensitive to warming temperatures, which can result in a greater fraction of winter precipitation falling as rain and an earlier arrival of the hydrograph center of timing, with cascading effects on surrounding ecosystems. Changes in land use can similarly disrupt the natural storage and release balance by altering the pathways in which water is routed through a system. These changes necessarily impact the ways in which sediment and other solutes are delivered through stream systems. This dissertation investigates material fluxes at the watershed scale in high mountain and seasonally cold regions in an effort to better understand the processes impacting their magnitude, timing, and release and the broader implications for the management of water resources.

Chapter 1 investigates these dynamics in the present day through the lens of a small urban headwater stream in the Northeastern United States characterized by frequent winter snowfall. In the surrounding watershed, sodium chloride is used seasonally as a deicing agent on roads and sidewalks, as is common in colder regions. Excess chloride loading poses a problem, however, because it can compromise sources of drinking water and threaten the health of surrounding ecosystems. The timing of chloride storage and release can also be altered in urban environments through the installation of armored stream channels and by increases in impervious surface cover. To investigate these landscape changes on chloride transport and storage, two years of streamflow and chloride concentration data were used to create continuous chloride load estimates for two

contrasting reaches of an urban stream. The upstream reach is characterized by channelization and armored banks and is largely disconnected from groundwater while the downstream reach flows through a riparian floodplain and has a strong groundwater connection. Results from this study show that chloride loads in the channelized reach were similar to chloride application rates in the surrounding watershed. In contrast, chloride loads in the downstream reach were 50% lower than those delivered from upstream due to stream-groundwater interactions and water losses through subsurface flow paths. These findings show that longitudinal load estimates can be helpful in identifying areas of chloride storage and release, the magnitude of which may not always be apparent in urban settings.

Chapters 2 and 3 consider both future and past influences on catchment scale sediment flux in the high Andes Mountains of Argentina and Chile. In this region, high mountain glaciers buffer streamflow during drier times of the year and water sourced from the uplands is critical to serving the needs of millions of people living in downstream communities such as Mendoza, San Juan, and Santiago. However, the high Andes are tectonically active, and sediment loads in regional streams and rivers can be high, posing a threat to the surrounding environment and human infrastructure alike. The area is also expected to face increases in temperature and decreases in precipitation in the coming decades. As a response, reservoirs have been built throughout the Andes, although the length of their usable lifespans is impacted by rates of sediment accumulation.

In Chapter 2, future changes in streamflow and catchment scale sediment flux in the high Andes are modeled based a suite of end-member climate projections for temperature and precipitation in the coming decades. Results from this study show that reductions in precipitation propagate into even larger decreases in streamflow and sediment flux, although results from scenarios modeling warming without a change in precipitation were much more variable. In Chile, where annual precipitation is concentrated in the winter months, warming lead to an increase in high magnitude streamflow events as more storms that would have delivered snow in the high Andes delivered rain instead. These events were also associated with high sediment loads and could be connected to an increased risk in geohazards such as landslides. In Argentina, however, where the Andes act as an orographic barrier to winter storm events originating from the Pacific, the streamflow and sediment flux response to warming was more akin to simulations with reduced precipitation. These results show that different water management strategies may be needed on either side of the Andes in the coming decades.

Chapter 3 takes a different approach, and investigates how sediment moves through the landscape over much longer timescales by utilizing cosmogenic radionuclides in several watersheds in the Argentine high Andes. First, ^{10}Be in river sand was used to estimate catchment-wide erosion rates at the millennial scale and compared to decadal scale erosion rates from steam gauge data, with comparisons generally showing favorable agreement. Erosion rate estimates were also used to predict how long water reservoirs sited at the foot of the Andes can be expected to last before becoming filled with sediment, with predictions from ^{10}Be for five different reservoirs occupying a fairly narrow range from 129 to 127 years. Finally, ^{10}Be samples were paired with an analysis of in situ ^{14}C in an effort to investigate sediment transport dynamics from the hillslope to catchment outlet. Low ^{14}C/^{10}Be ratios in this study suggest that despite agreement between decadal and millennial scale erosion rates, sediment transport times through these complex watersheds may range from a minimum of 10,000 to 19,000 years. This finding further indicates that sediments carried by streams out of the mountain front in the present may have been eroded from high elevation hillslopes in the early Holocene or even the late Pleistocene, connecting events in the geologic past to processes impacting humans today.

THE IMPACTS OF CLIMATE AND LANDSCAPE CHANGE ON CATCHMENT SCALE MATERIAL TRANSPORT IN HIGH MOUNTAIN AND SEASONALLY COLD REGIONS

by

John Russell Slosson

B.A., University of Virginia, 2006
J.D., University of Virginia, 2009

Dissertation

Submitted in partial satisfaction of the requirements for the degree of
Doctor of Philosophy in Earth Sciences

Syracuse University
July 2021

Acknowledgements

I would like to thank Greg Hoke, Laura Lautz, and Christa Kelleher for providing invaluable advice and for their willingness to help mentor an attorney on the road to becoming a scientist. I am also thankful for the assistance of many colleagues in the Department of Earth and Environmental Sciences. I am especially grateful for the support of my wife and family during the course of my studies.

This work has been supported by the National Science Foundation under Grant DGE-1449617, by the Geological Society of America John T. and Carol G. McGill Award, and by Syracuse University's and the Education Model Program on Water-Energy Research (EMPOWER), Collaboration for Unprecedented Success and Excellence (CUSE), and Research Excellence Doctoral Funding (REDF) programs.

Table of Contents

List of Figures

Chapter 1

Chapter 2

Chapter 3

List of Tables

Chapter 1

Chapter 2

Chapter 3

Chapter 1

Chloride Load Dynamics along Channelized and Intact Reaches in a Northeastern United States Headwater Stream

Chapter 1 has been published as:

Slosson, J.R., Lautz, L.K., & Beltran, J. 2021. Chloride load dynamics along channelized and intact reaches in a northeastern United States urban headwater stream. *Environmental Research Letters*, 16: 025001. https://doi.org/10.1088/1748-9326/abd8ab

Abstract

Sodium chloride has long been used for winter deicing, although its legacy use has resulted in rising chloride concentrations in urban watersheds. Persistently high chloride levels impair drinking water resources and threaten the health of aquatic life and vegetation. In urban areas, chloride fate and transport is impacted by human modification of the environment, including increased impervious surface cover and disconnection of stream corridors from riparian groundwater. Continuous streamflow records were coupled with weekly chloride concentration data over two water years to create continuous chloride load estimates at three locations along a degraded, urban stream in upstate New York with contrasting channelized and intact reaches. Results show that degraded reaches characterized by channelized, armored banks and minimal groundwater connection deliver chloride loads closer to chloride application rates in the surrounding watershed. In contrast, stream-groundwater interactions in intact reaches adjacent to riparian floodplains, including surface water losses to subsurface flow paths, result in stream chloride loads that are 50% less than those delivered from upstream channelized reaches. These findings show that longitudinal chloride load estimates along a stream channel can be valuable in identifying the timing and magnitude of chloride sources and sinks, which may be common but less apparent in urban environments.

1. Introduction

Sodium chloride (NaCl), commonly known as road salt when used as a deicer, is widely used in the United States to improve traffic safety (CMA, 1991). However, in recent years more has become known about the detrimental impacts of road salt on the environment, including compromised sources of potable water (Pieper et al., 2018; Kaushal, 2016; Jackson & Jobbágy, 2005; Ramakrishna & Virarghavan, 2005), corrosion of automobiles and infrastructure (Pieper et al., 2018; Stets et al., 2018; CMA, 1991), and harm to aquatic life and vegetation (Arnott et al., 2020; Patykowski et al., 2018; Jackson & Jobbágy, 2005; Kaushal et al., 2005; Marsalek 2003). Accordingly, the U.S. Environmental Protection Agency (USEPA) has established chronic (four-day average) and acute (one-hour average) ambient water quality limits for chloride of 230 mg L^{-1} and 860 mg L^{-1}, respectively (USEPA 1988).

The impacts of road salt usage can be magnified in urban settings, where application rates are elevated due to increased road density. In these environments, increases in impervious surface cover are linked with flashier hydrographs (Walsh et al., 2005; Paul & Meyer, 2001) and road salt runoff can be more rapidly conveyed to streams and rivers, leading to short-term surges in chloride concentrations that exceed acute toxicity levels (Ledford & Lautz, 2015; Kaushal et al., 2005). These problems are further compounded by stream channelization and the installation of artificial bank armoring, disconnecting streams from groundwater (Ledford et al., 2016; Walsh et al., 2005). Numerous studies have also reported increasing freshwater chloride concentrations near urban areas over time, including in streams and rivers (Corsi et al., 2015; Cooper et al., 2014; Shaw et al., 2012; Howard & Maier, 2006; Kaushal et al., 2005), groundwater (Cooper et al., 2014; Cassanelli & Robbins, 2013), entire watersheds (Novotny et al., 2009), and even the Great Lakes (Chapra et al., 2009).

Stream-groundwater interactions can mitigate the impacts of road salt in multiple ways by regulating water quality and buffering environmental perturbations (Krause et al., 2008). First, in the winter, saline stream water can be exchanged with riparian groundwater, which serves as a temporary reservoir for high chloride loads and can dilute chloride through mixing of saline stream water with lower chloride groundwater. Such short-term storage of saline stream water in the subsurface can occur as temporary loss in flow from the stream to riparian aquifers, or as hyporheic flow. Second, in gaining streams, groundwater discharge of relatively fresh water can dilute chloride concentrations in water that is delivered to urban streams from surface runoff (Ledford & Lautz, 2015, Paul & Meyer, 2001). Long-term road salt usage can also reduce the benefits of stream-groundwater interactions, however. Both the exchange of saline stream water with near-stream zones, as well as groundwater recharge by infiltration of saline water, introduce road salt to groundwater systems, which is not easily mitigated. Road salt cannot easily be removed from groundwater (Meriano et al., 2009) and may persist in aquifers long after the winter season (Gabor *et al* 2017), in some cases for years (Robinson & Hasenmueller., 2017) or even decades (Kelly et al., 2019). More detailed spatiotemporal estimates of chloride outputs from urban streams, relative to salt inputs, will provide insights into road salt transport and storage in degraded urban streams.

Meadowbrook Creek, a headwater stream in central New York, offers an opportunity to study the impacts of road salt usage in an urban stream with contrasting channelized and intact reaches. Along a sizeable and continuous upstream reach, Meadowbrook Creek is characterized by channelized, artificial banks with minimal groundwater flow. Along a distinct downstream reach, the creek flows through a riparian floodplain with a strong groundwater connection. Prior studies in Meadowbrook Creek have investigated the transport and fate of chloride (Ledford et al., 2016; Ledford & Lautz, 2015) and other contaminants (Ledford et al., 2017). Ledford and Lautz (2015) observed that stream chloride concentrations were highest in the channelized portion of the reach during the winter deicing season, but concentrations declined as the stream flowed through the riparian floodplain due to the moderating impact of stream-groundwater interactions. In the summer, however, chloride concentrations in the stream remained elevated along the riparian floodplain. Ledford et al. (2016) hypothesized that riparian groundwater was periodically recharged during the winter by high salinity, overbank flooding events, and subsequently discharged to the stream during the summer.

In this study, high-frequency estimates of chloride load were made at multiple sites to quantify spatiotemporal differences in chloride fluxes in the contrasting reaches of Meadowbrook Creek and to compare the dynamics of road salt transport between stream reaches with and without stream-groundwater exchange. Prior work in this watershed focused on chloride concentrations (Ledford et al., 2016; Ledford & Lautz, 2015), as is common in studies investigating the impacts of winter road salt usage (e.g., Corsi et al., 2015; Kaushal et al., 2005). While concentrations are important for understanding when contaminant levels pose a threat to aquatic life or human health (USEPA, 1988), loads provide additional insight about the magnitude of contaminant fluxes through a system and source versus sink dynamics, which may not always be readily apparent in urban environments.

2. Methods

2.1. Study Site

Meadowbrook Creek is a 5.6 km, first-order stream in central New York with an 11.2 km^2 contributing area. It drains to a feeder channel for the Erie Canal and ultimately to Butternut Creek (Figure 1). The upper 4.1 km of Meadowbrook Creek starts below a stormwater retention basin in the City of Syracuse and flows through an armored channel with minimal groundwater connection ("disconnected reach"). For most of its length, the disconnected reach is bordered by one lane of Meadowbrook Drive on either side. The lower 1.5 km of Meadowbrook Creek meanders through a riparian floodplain and has a strong groundwater connection ("connected reach"). Average road densities are similar in the contributing areas of the disconnected and connected reaches, at 8.5 and 9.0 km road/km^2, respectively. However, along a 200 m corridor surrounding either reach, road density is much higher in the disconnected reach, measuring 13.6 km road/km^2, versus 6.1 km road/km^2 in the connected reach (Ledford & Lautz, 2015). Many homes in the surrounding neighborhoods are older, especially within the disconnected reach, with some dating to the late 1800s and early 1900s (City of Syracuse, 2010). Area homes are served by sanitary gravity sewer lines and a dedicated trunk sewer line adjacent to Meadowbrook Creek. A series of stormwater drains empty directly into Meadowbrook Creek, but are rarely observed flowing except during storm events (Ledford et al., 2017).

Geologically, Meadowbrook Creek originated as a meltwater channel following the Last Glacial Maximum. The surrounding watershed is underlain by Silurian-aged bedrock (Muller, 1964) and unconsolidated glacial deposits cover much of the Syracuse area (Kantrowitz, 1964). The surficial geology in a narrow corridor running along the length of the stream channel consists of alluvium ranging from silty clay to fine sand and gravel emplaced by modern streams, while the surrounding hillslopes are layered by thin till or lodgment till. In the connected reach, however, Meadowbrook Creek flows through an area predominantly covered by outwash sand and gravel (Winkley, 1989). Drill cuttings in a floodplain adjacent to the stream channel in the connected reach revealed a silty-clay surface layer overlying a more permeable sandy-silt layer, with the transition to the sandy-silt layer occurring at around 1 m depth (Ledford et al., 2016).

The Syracuse area has a temperate climate strongly impacted by seasonal snowfall, receiving an average of 248 cm of snow annually. The local transportation department relies exclusively on road salt to treat roadways during winter (Ledford & Lautz, 2015), with the City of Syracuse applying an average of over 2.7 x 10^7 kg of road salt annually. Road salt is applied as a pretreatment before and during winter precipitation events while municipal plows clear roads during and after snowfall (City of Syracuse ,2020). In some cases, snow is removed by dump trucks to centralized locations, especially after prolonged periods of colder temperatures when snow does not melt (Coin, 2015).

2.2. Field Methods

Water level, conductivity, and stream temperature were recorded at fifteen-minute intervals by Seametrics CT2X loggers installed at three automated gauging station locations on Meadowbrook Creek in the summer of 2017. The first station is less than 0.2 km below the retention basin ("disconnected headwater"). The second gauging station sits just below the end of the channelized portion of Meadowbrook Creek in the transition area between the disconnected reach and the connected reach ("transition site"). The third gauging station is near the outlet of the connected reach ("connected outlet"). The contributing areas of the disconnected headwater, transition site, and connected outlet are 3.4, 9.2, and 10.6 km^2, respectively, calculated based on area topography using ESRI ArcGIS 10.7.

Streamflow was measured at all three sites using a SonTek-IQ Plus and additional streamflow measurements were collected at the connected outlet with a handheld SonTek/YSI FlowTracker Acoustic Doppler Velocimeter. Streamflow measurements were paired with stage measurements to create rating curves for each site. Rating curves were used in conjunction with all available stage data to generate hydrographs for water years 2018-2019 at fifteen-minute intervals. Additional details on stream gauging are available in supplementary information S1.

Grab samples were collected in 60 ml high-density polyethylene bottles at each site at approximately weekly intervals throughout water years 2018-2019. A total of 98 samples were collected at each location during this period. Samples were filtered in the field with 0.45 µm nylon Millipore Millex-NH syringe filters and stored at 4 °C. Chloride concentrations were measured using a Dionex ICS-2000 Ion Chromatograph.

2.3. Load Estimation

The United States Geological Survey's LOAD ESTimator ("LOADEST") was used to model chloride loads at hourly intervals at each site for water years 2018-2019. LOADEST is a Fortran program that creates a linear regression model of a given constituent load when supplied with streamflow, time, and other user-selected explanatory variables (Runkel et al., 2004). LOADEST has been used to estimate a variety of different pollutant loads in streams and rivers (Park & Engel, 2015; Duan et al., 2013; Jones & Schilling, 2013), including chloride loads (Brown et al., 2015). A description of the methods used within LOADEST is available in supplementary information S2. LOADEST models for each site were calibrated using observed chloride concentrations from field samples and their corresponding stream discharge rates to create point measurements of chloride load. Daily snow depth as recorded at the Syracuse airport was included as an additional calibration variable for all three sites. Specific conductivity was included as a calibration variable at the transition and connected outlet sites. Instantaneous estimates of chloride load were calculated at hourly intervals using the calibrated regression models and the full time series of explanatory variables for each site for water years 2018-2019.

3. Results

3.1. Streamflow and Stream Temperature

Streamflow behaved differently in the connected versus the disconnected reach and exhibited contrasting seasonal patterns (Figure 2, Table 1). Total annual streamflow was lowest at the disconnected headwater, where baseflow is low and instantaneous streamflow rates spike during precipitation events, producing a flashy hydrograph. There were also periodically observable but minor (≤ 0.01 m^3/s) "step changes" in low flows, which may be the result of adjustments to an outlet valve draining the upstream retention basin. Annual streamflow was higher at the transition site than the disconnected headwater. Streamflow rates were often highest at the transition site during the winter season when temperatures are colder, evaporation is at a minimum, and precipitation falls as snow. In contrast, streamflow rates at the connected outlet were generally lower than at the transition site from early fall until late spring and summer. During the summer, the pattern reversed and streamflow rates at the connected outlet exceeded those at the transition site, although apparent gains during the summer were not enough to offset apparent losses during the winter. In total, streamflow observed at the connected outlet was only 64% and 66% of annual streamflow observed at the transition site during water years 2018 and 2019, respectively (Table 1).

Average monthly stream temperatures at the disconnected headwater and transition site were closely aligned, and within 0.5 °C of one another during 70% of the months in the study period (Table 2). Average monthly stream temperatures at the connected outlet, however, were more than 2 °C warmer or cooler than at the transition site for over 50% of the study period. Stream temperatures also showed more annual variance at the disconnected headwater and transition sites than at the connected outlet, with the connected outlet generally being cooler during the summer and warmer in the winter as compared to the two upstream sites (Table 2).

3.2. Surface Water Chloride Concentrations

Stream chloride concentrations were highest in the winter, typically coincident with winter precipitation and snowmelt events (Figure 3, Table 3). The highest chloride concentrations were observed at the transition site, reaching 2888 and 2734 mg L^{-1} in water years 2018 and 2019, respectively. Chloride concentrations were typically lowest at the disconnected headwater site, with maximum recorded values of 1339 and 967 mg L^{-1} during the winters of water years 2018 and 2019, respectively. Chloride concentrations were much lower at all sites in the summer (<430 mg L^{-1}), although summer concentrations were consistently higher at the connected outlet than the other two sites during this time. Summer chloride concentrations also increased at the connected outlet between water years 2018 and 2019. Concentrations never exceeded 330 mg L^{-1} at the connected outlet from May through September in water year 2018, but five samples contained concentrations between 400 and 430 mg L^{-1} during that same period in water year 2019.

Chloride Load Models

Streamflow, centered decimal time and snow depth were all statistically significant ($p < 0.05$) predictive variables in the regression model used to estimate chloride loads at each site. Specific conductivity was also a significant variable in the models for the transition site and connected outlet. R-squared values for the disconnected headwater, transition site, and connected outlet models were 85.8%, 90.8%, and 72.0%, respectively (Table 4).

The models show that chloride loads peak in the winter, but unlike the concentration data alone, the load models also reflect overall trends in streamflow (Figure 4). The timing of the highest average streamflow at the transition site occurred closer to the timing of peak chloride concentrations, resulting in very large chloride loads in winter at the transition site. Average monthly chloride loads during January, February, and March were highest at the transition site than any other time of the year and accounted for 60-65% of the total chloride load observed at that location during each of the two water years investigated (Figure 5, Table S1). In contrast, at the connected outlet, seasonal variations in streamflow were smaller in magnitude and offset relative to peak chloride concentrations (Figures 2-3, Table 1). The result is that, in some cases, peak chloride loads at the connected outlet occurred later in the year. Combined January, February, and March loads at the connected outlet only accounted for 28-35% of the total loads observed at that site during the two water years. During the months of July, August, and September, however, loads were slightly higher at the connected outlet than the transition site during both water years (Figure 5, Table S1). For water year 2018, total loads at the disconnected headwater, transition site, and connected outlet, respectively, were 0.54 x 10^6 kg, 2.1 x 10^6 kg, and 0.86 x 10^6 kg. For water year 2019, the respective total loads were 0.45 x 10^6 kg, 2.0 x 10^6 kg, and 1.0 x 10^6 kg (Table 5).

4. Discussion

4.1. Spatiotemporal Streamflow Patterns and Stream-Groundwater Interactions

The contrasting patterns of streamflow between the disconnected and connected reaches reflect seasonal changes within the watershed and the different hydrologic characteristics of the two reaches. Streamflow in the disconnected reach reflects the urbanized nature of the watershed and efficient conveyance of water to the stream channel (Walsh et al., 2005). Annual runoff ratios (streamflow expressed as a percentage of total precipitation) for the disconnected reach subwatershed are higher than for the watershed as a whole (42% vs 24% in both water years; Table 1). These higher runoff ratios indicate that a higher percentage of precipitation in the disconnected reach subwatershed becomes streamflow, versus being lost to evapotranspiration or changes in groundwater storage, than in the watershed as a whole. This is particularly true in winter months, when runoff ratios in the disconnected reach subwatershed routinely exceed 50% but rarely exceed 50% in the watershed as a whole. Streamflow is comparatively high at the transition site during the winter, when evapotranspiration in the Syracuse area is minimal (Squier-Babcock & Davidson, 2020) and rain-on-snow events and winter thaws rapidly convey water to the stream channel.

In contrast, streamflow in the connected reach is lower than at the transition site throughout the winter, indicating that it is a seasonally losing reach. Moderated stream temperatures in the connected reach suggest that observed surface water losses between the transition site and the connected outlet may be due to the presence of hyporheic and groundwater flow paths (Kaandorp et al., 2019, Menichino & Hester, 2014). Some stream cooling in the connected reach relative to the disconnected reach during the summer may be due to shading from leaf cover, however (Dugdale et al., 2018). Unconsolidated glacial and floodplain deposits in the connected reach are likely conducive to the development of flow paths outside of the stream channel, given their hydraulic conductivity (~2 x 10^{-6} m/s to 2 x 10^{-4} m/s, Ledford et al., 2016). Previous piezometer observations in the connected reach floodplain show that chloride concentrations in groundwater within 3.7 m of the stream channel peak during the winter, showing similar geochemistry to the stream channel. Further from the stream, at the toe of a hillslope, groundwater chloride concentrations are lower overall and do not peak until April, around the end of the snowmelt season, reflecting groundwater concentrations impacted by direct infiltration and groundwater recharge (Ledford & Lautz, 2015).

High flows from the disconnected reach may recharge groundwater in the connected reach during the winter months. Particularly high flow events likely result in bank storage in the connected reach and reduced channel flow at the connected outlet, as is seen in other snow-dominated catchments (Huntington & Niswonger, 2012; Pinder & Saur, 1971). In prior work, Ledford and Lautz also hypothesized that the floodplain in the connected reach is periodically recharged by wintertime overbank flooding events that are observed in the catchment, as well as lateral exchange between the stream and bank (2015, Ledford et al., 2016). Using a modeling approach, Ledford *et al* estimated that the mean residence time of chloride in groundwater originating from stream channel overbank flooding during the winter was 55 days (2016). Around the time that high flows from the disconnected reach begin to subside in the spring, groundwater discharge of water temporarily stored in the connected reach begins to contribute to elevated flows at the connected outlet during the summer.

Although short-term storage of streamwater in the near-stream zone explains some of the winter water loss from the connected reach, the total annual changes in streamflow between the transition and connected outlet gauges cannot be explained by this mechanism alone because there is not sufficient capacity to store this volume of water in the floodplain. 36% and 34% of the total streamflow at the transition site in water years 2018 and 2019, respectively, was lost between the transition site and the connected outlet gauge. Given the topography of the lower reaches of the watershed, it is probable that some of this water loss is to groundwater flow that ultimately discharges directly to the Erie Canal feeder channel and Butternut Creek near the outlet of the watershed. It is also hypothesized that the hyporheic zone in the connected reach, which is absent in the concrete-lined disconnected reach, conveys some of the streamflow through the connected reach and effectively bypasses the gauging station, which only captures flow in the stream channel itself.

Along the nearly 1.5 km that Meadowbrook Creek travels from the transition site to the connected outlet, the stream flows through grass-covered open floodplains, tree-lined banks, and several meanders. Given the moderated stream temperatures, loss of streamflow, and moderated chloride concentrations during the winter, it is possible that gross streamwater losses and gains occur simultaneously along different sections of the reach (Payn et al., 2009). While the full extent of subsurface flow paths are beyond on the scope of this work, they likely contribute to the movement of water originating from the disconnected reach and warrant further research given their impact on contaminant fluxes through the watershed.

4.2. LOADEST Models

The goodness-of-fit metrics indicate that the LOADEST models used in this study are well suited to comparing seasonal surface water chloride loads between the connected and disconnected reaches. All modeled R-squared values were over 70% and two sites, the disconnected headwater and connected outlet, had R-squared values over 85%. Time series of modeled and observed loads at the three sites are in strong agreement across loading values that span an order of magnitude (Figure 4). While all regression variable p-values were less than 0.05, snow depth was particularly significant, with a p-value below 0.001 at each site (Table 4), likely reflecting the impact of road deicing efforts undertaken in close proximity to winter precipitation events. The 95% confidence intervals for annual loading rates also show that net loads at the transition site are always higher than at the connected outlet (Table 5).

4.3. Chloride Load Dynamics in Contrasting Reaches

Modeled chloride loads reflect both the seasonal nature of chloride application in the watershed and streamflow dynamics between the different reaches. High seasonal chloride loads at the transition site are consistent with other studies showing that road salts are rapidly mobilized and flushed through stream corridors in urban environments. Winter chloride loads and concentrations in streams increase with increases in watershed road density and development (Brown et al., 2015; Gardner & Royer, 2010), particularly when major highways and heavily trafficked roads are close to stream channels (Cooper et al., 2014). Elevated chloride loads at the connected outlet during the summer are also consistent with short-term storage of chloride in groundwater. This observation is common in both rural and urban stream corridors with a groundwater connection where road salt is used seasonally (Gabor et al., 2017; Gutchess et al., 2016; Cooper et al., 2014; Kelly et al., 2008).

In the disconnected reach, chloride loads at the transition site are a closer reflection of estimated chloride inputs from road salting efforts than at the connected reach, and likely reflect the conservative nature of the chloride ion (Lehman, 2018). Normalizing average annual road salt usage in the City of Syracuse by its 66.3 km^2 area and assuming the road salt is 60% chloride by weight, the average annual road salt usage by the City equates to approximately 2.4 x 10^5 kg of chloride per km^2 (City of Syracuse, 2020). With an average road density in Syracuse of 12.8 km road/km^2, this equates to an application rate of 19,000 kg per km of road. Normalizing the total load at the transition site by its 9.2 km^2 contributing area and average road density of 8.5 km road/km^2 results in average application rates of 27,000 and 26,000 kg/km road for water years 2018 and 2019, respectively. These rates are higher than the City rate by 37-42%, implying a total excess of chloride in the disconnected reach ranging from 5.2 x 10^5 to 6.1 x 10^5 kg each water year. However, comparisons with the average City salt application rate do not account for sources of chloride beyond municipal application, such as private residences, businesses, and parking lots (Oswald et al., 2019, Evans et al., 2018, Kelly et al., 2008), as well as other sources of chloride in addition to road salt. The average City usage also likely varies from actual application rates in the disconnected reach, and the busy Meadowbrook Drive, adjacent to Meadowbrook Creek in the disconnected reach, may receive a comparatively high application of road salt. Road salt usage by the City also varies annually, and the City has used as much as 4.1 x 10^7 kg of road salt per year in the past – 150% of its more recent average (Weiner, 2000). Nonetheless, future investigation to identify potential additional sources of chloride in the disconnected reach are warranted. Overall, however, these comparisons suggest that in the disconnected reach most of the annual chloride load applied to the contributing area makes its way into Meadowbrook Creek within the same water year. This is consistent with the high water yields for the disconnected reach watershed discussed earlier, which indicate that over 50% of winter precipitation in the disconnected reach contributing area becomes streamflow, and only a small percentage is lost to evapotranspiration or groundwater recharge.

Annual loads in the connected reach are less of a reflection of annual inputs to the system than the disconnected reach and are smaller by total volume than the disconnected reach despite corresponding to a larger contributing area. Indeed, of the total 2.1 x 10^6 kg of road salt discharged from the disconnected reach in water year 2018, only 41% was subsequently discharged in streamflow at the outlet of the connected reach. Similarly, in water year 2019 only 50% of the total 2.0 x 10^6 kg of chloride measured at the disconnected reach was ultimately discharged through surface water at the connected reach (Table 5). Nearly all of this difference in total load occurred from November to April in both water years (Figure 5, Table S1), when observed surface water flows at the connected outlet were lower than at the transition site. It is hypothesized that during this time a fraction of the total chloride delivered from upstream likely moved through the connected reach watershed through groundwater and hyporheic flow paths outside of the stream channel or accumulated as short-term storage in riparian areas. The difference in loads observed at the disconnected and connected reaches highlights the complicated nature of tracing chloride through urban systems and indicates that loads observed in surface waters may not always fully represent annual chloride inputs (Lam et al., 2020).

The study results also indicate that the use of chloride concentrations as an indicator of chloride movement through an environment can mask the total magnitude of possible chloride sources and sinks if the peak concentrations do not correspond to peak streamflow rates. At all three sites in this study, chloride concentrations peaked in close proximity to winter precipitation events (Figure 3, Table 3). However, while stream hydrographs also show that total streamflow at the disconnected headwater and transition site were also highest during the winter, streamflow at the connected outlet increased during the spring (Figure 2, Table 1). As a consequence, winter loads at the transition site in particular were very high in the winter, while some of the highest chloride loads at the connected outlet occurred in the spring when streamflow there was higher, even though peak chloride concentrations were typically observed earlier in the year (Figure 5, Table 3, Table S1).

4.4. Long-Term Implications

Because the patterns of streamflow and annual chloride loads in Meadowbrook Creek are strongly seasonal, they could be sensitive to a changing climate. Many parts of the northeastern United States are warming and experiencing a loss of seasonal snow cover (Contosta et al., 2019; Burakowski et al., 2008). These climatic shifts could translate to increased winter precipitation in the form of rain, changes in the timing of large streamflow events, and alterations in stream-groundwater interactions in the connected reach. Less seasonal snow cover would also likely result in decreased anthropogenic chloride inputs to the watershed, however (Gutchess et al., 2018). These potential changes will likely impact urban stream corridors with riparian floodplain connections throughout the northeastern United States in the coming decades and warrant additional study.

We also observed that summer month (July-September) grab sample chloride concentrations at all three sites increased from water year 2018 to water year 2019 (Table 3). This increase was greatest at the connected outlet, where concentrations over this three-month period rose from 245 mg L^{-1} in water year 2018 to 319 mg L^{-1} in water year 2019 (Figure 6). Notably, these concentrations are higher than the USEPA's chronic ambient water quality limit of 230 mg L^{-1}, even though they occurred months after the end of the road de-icing season. The average grab sample chloride concentration during these three months was also higher than that reported by Ledford at al. (2016) at the connected outlet during the same time span during water year 2012 (175 mg L^{-1}). Total summer month loads also increased at the transition site and connected outlet from water year 2018 to water year 2019, but declined slightly at the disconnected headwater (Figure 5, Table S1). Flow-weighted mean concentrations, calculated by dividing total monthly load by total monthly streamflow, were comparatively equal from water year 2018 to 2019 during the summer, however, and within 2 mg L^{-1} from one year to the next at each site during this time (Table S1).

While continued monitoring is required to determine if the increases in observed grab sample concentrations and loads during the summer are part of a larger trend, increasing chloride concentrations are common in other urban areas in snow-impacted regions (Corsi et al., 2015; Cooper et al., 2014; Shaw et al., 2012; Howard & Maier, 2006; Kaushal et al., 2005). It is possible that the increased summer month grab sample concentrations and loads at the connected outlet during the course of this study are a result of rising groundwater salinity in the connected reach aquifer (Cooper et al., 2014, Howard & Maier., 2006). This increased salinity could result from infiltration of saline water throughout the watershed from road runoff, ultimately entering the groundwater system beneath the connected reach floodplain via subsurface flow paths. Increasing groundwater salinity could also result from the short-term storage of saline water from the stream channel during the winter as a result of stream-groundwater interactions in the connected reach. The specific mechanisms of groundwater salinization in this watershed are an open question for future research. Moreover, because a significant amount of chloride is lost from the stream channel in the connected reach and could negatively impact the surrounding ecosystem, future efforts should also focus on more fully identifying and quantifying subsurface transport and storage of chloride within the watershed.

5. Conclusion

The findings of this study highlight the complicated nature of chloride transport through urban systems. While chloride loads observed in the disconnected reach appear closer to estimated road salt application rates within the upstream contributing area than at the connected reach, they exceed estimated municipal road salt usage by 37-42%. In contrast, comparatively small loads in the connected reach suggest the presence of flow paths outside of the stream channel and possible short-term groundwater storage. The results of this study also suggest that chloride sources and sinks may be common in urban environments and indicate that longitudinal chloride load estimates can be helpful in identifying their magnitude and duration. Elevated summer month grab sample chloride concentrations in the connected reach above the USEPA ambient water quality chronic limit during the two years of this study are similar to the findings in other urban areas in snow-dominated regions and is a potential cause for concern. The unique interactions between urban stream systems with significant contrasting characteristics, such as the channelized and intact reaches of Meadowbrook Creek, warrant continued research and monitoring of these dynamic and important environments.

Acknowledgements

This work was supported by the National Science Foundation under Grant DGE-1449617 and by Syracuse University's Collaboration for Unprecedented Success and Excellence (CUSE), Education Model Program on Water-Energy Research (EMPOWER), and Research Excellence Doctoral Funding (REDF) programs.

Figures

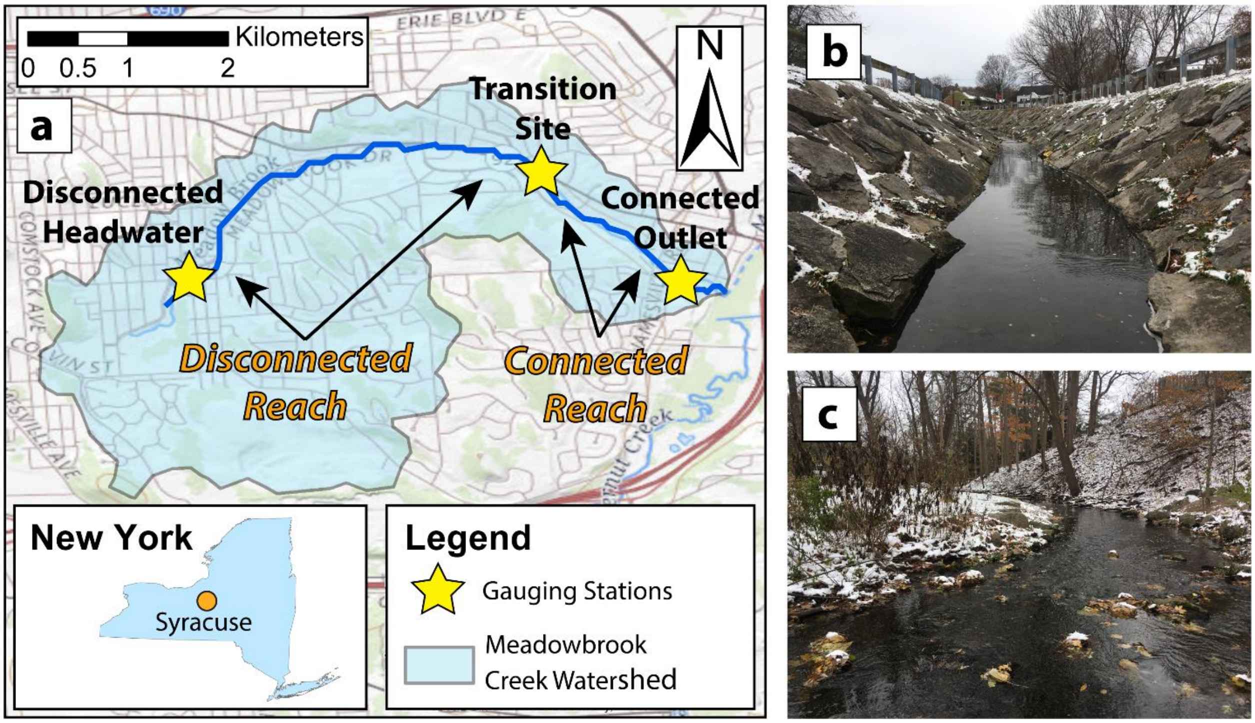

Figure 1. (a) Meadowbrook Creek watershed. Inset map shows the location of the City of Syracuse in New York State. (b) Disconnected headwater gauging station, lined with armored banks and roadways. (c) Connected outlet gauging station location, surrounded by a natural floodplain.

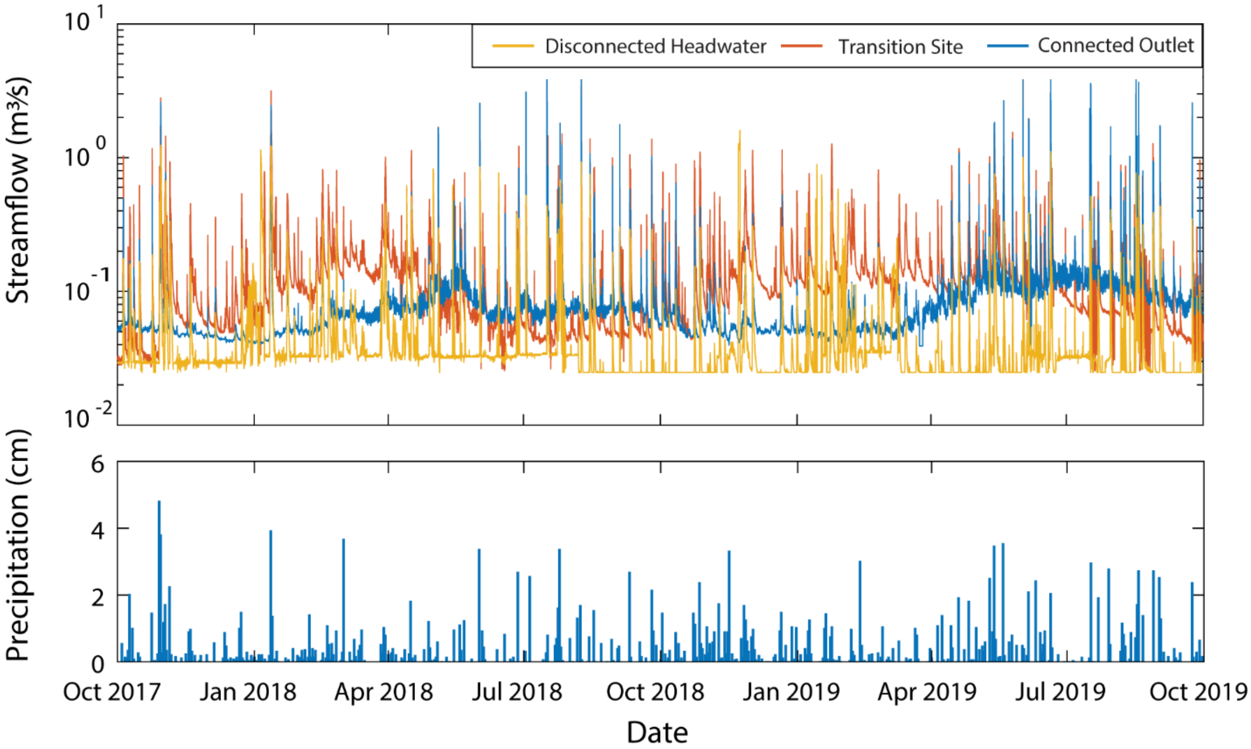

Figure 2. Hydrographs for Water Years 2018-2019 for all three Meadowbrook Creek monitoring sites. Streamflow is higher at the transition site than at the connected outlet during the winter and early spring months. During the summer months, streamflow is higher at the connected outlet than all other sites. Daily precipitation totals for both water years as recorded at the nearby Syracuse Hancock International Airport is shown on the bottom panel.

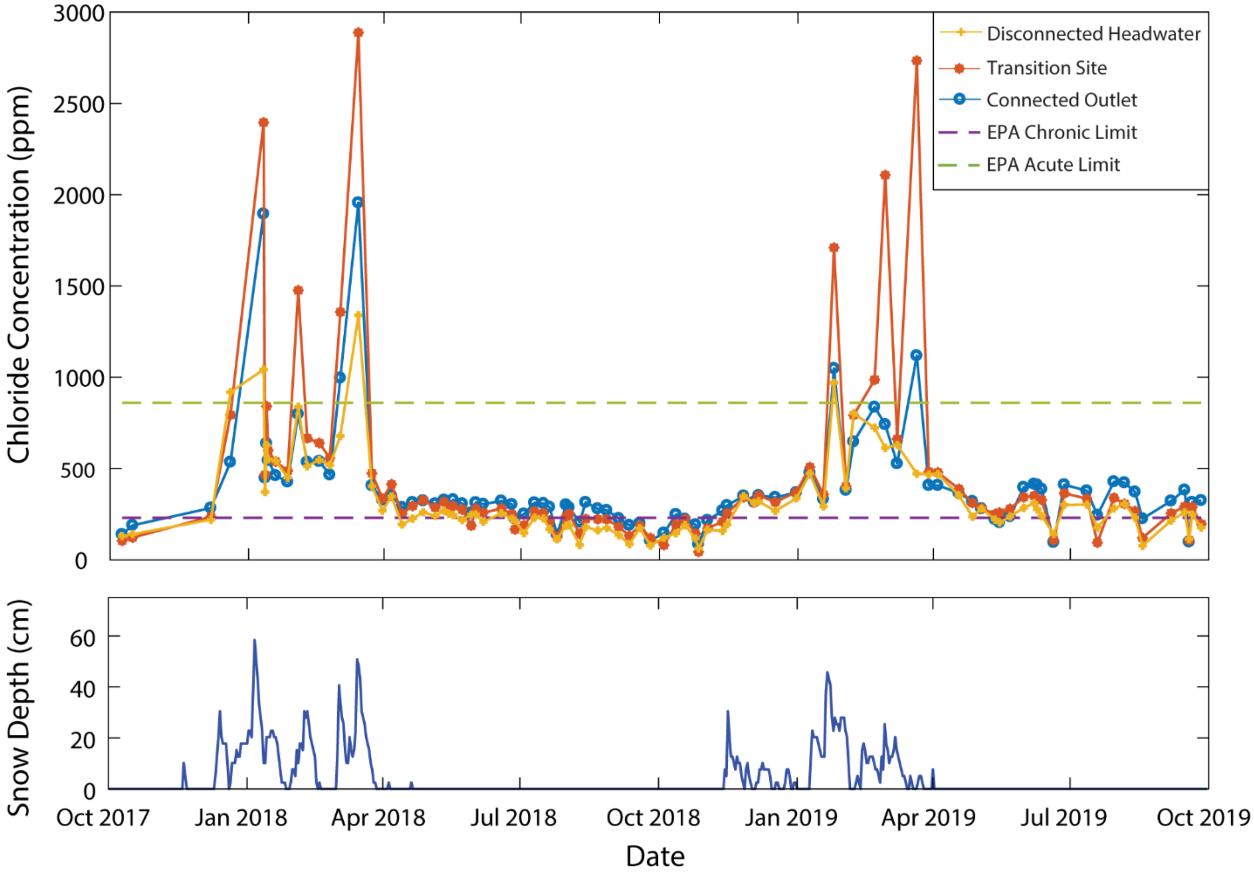

Figure 3. Grab sample chloride concentrations for Water Years 2018-2019 at all three Meadowbrook Creek monitoring sites. Measured concentrations are highest at the transition site during the road deicing season. During the summer months, concentrations are highest at the connected outlet. EPA chronic and acute ambient water quality limits are shown for comparison. Daily snow depth as recorded at the Syracuse Hancock International Airport is shown on the bottom panel.

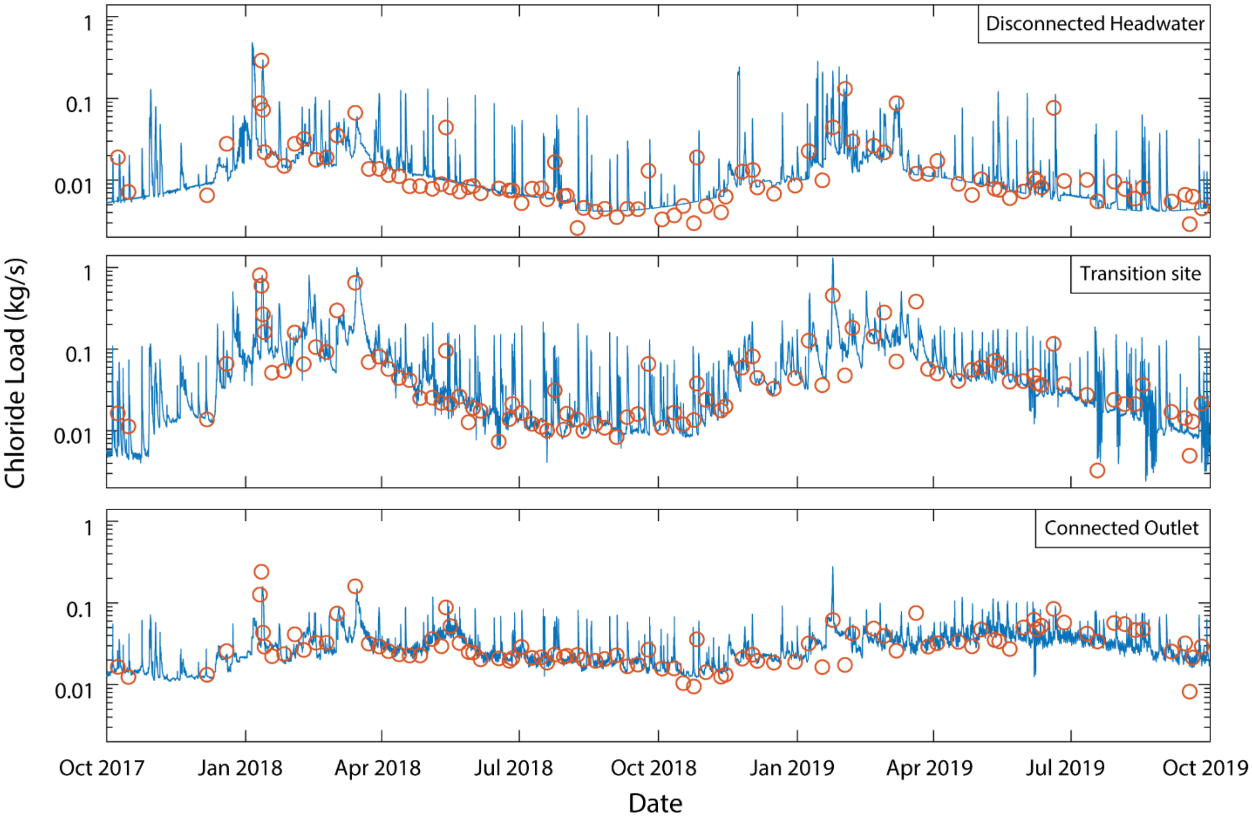

Figure 4. Instantaneous chloride loads for Water Years 2018-2019 for all three Meadowbrook Creek monitoring sites calculated at hourly intervals using LOADEST. Instantaneous observed loads for individual grab samples are shown as open circles for model comparison.

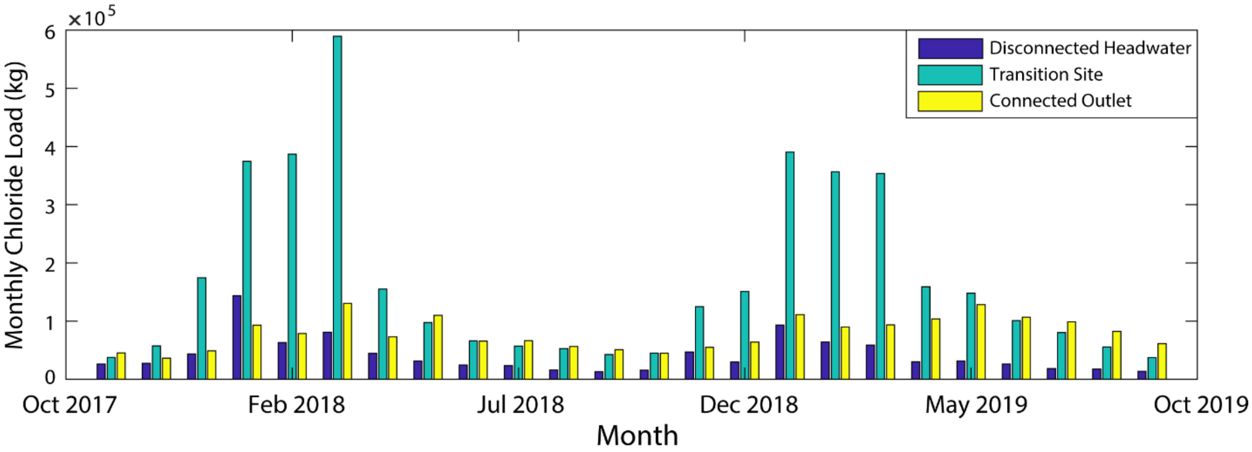

Figure 5. Monthly loads for Water Years 2018-2019 for all three Meadowbrook Creek monitoring sites as calculated using LOADEST.

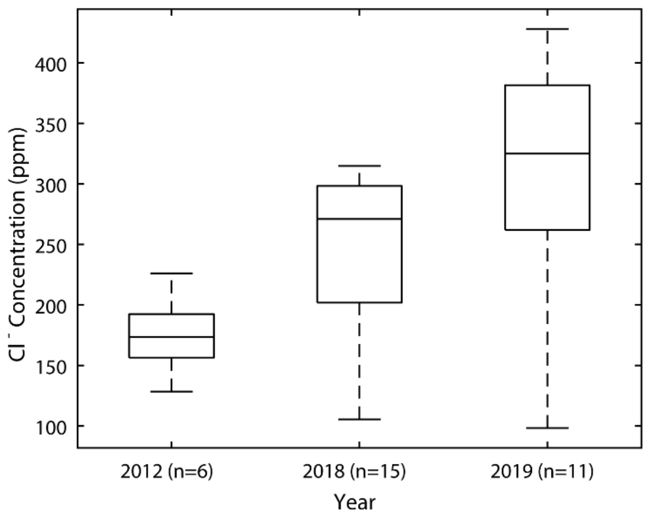

Figure 6. Summer (July-September) grab sample chloride concentrations at the connected outlet for 2012, 2018, and 2019 (2012 data from Ledford *et al* 2016). Average concentrations increased in all years sampled.

Tables

Table 1(a). Precipitation and snowfall measured at the Syracuse Hancock International Airport and streamflow (Q) for all three monitoring sites for water year 2018.

Month	**Total Precip (cm)**	**Total Snowfall (cm)**	**Disconnected Headwater Total Q (m^3)**	**Disconnected Headwater Area-Normalized Total Q (cm)**	**Transition Site Total Q (m^3)**	**Transition Site Area-Normalized Total Q (cm)**	**Connected Outlet Total Q (m^3)**	**Connected Outlet Area-Normalized Total Q (cm)**
October	15.5	0.0	167,897	4.94	276,316	3.00	214,209	2.02
November	9.3	13.2	129,372	3.81	307,237	3.34	153,837	1.45
December	5.9	86.9	107,254	3.15	210,204	2.28	122,002	1.15
January	8.0	113.0	297,642	8.75	531,970	5.78	194,159	1.83
February	7.5	59.9	126,942	3.73	414,242	4.50	155,382	1.47
March	9.8	110.7	144,705	4.26	513,123	5.58	200,680	1.89
April	6.3	6.4	131,645	3.87	431,931	4.69	217,369	2.05
May	4.8	0.0	113,236	3.33	294,703	3.20	312,866	2.95
June	9.0	0.0	122,519	3.60	241,050	2.62	221,419	2.09
July	10.8	0.0	153,928	4.53	287,144	3.12	290,196	2.74
August	7.5	0.0	114,023	3.35	246,185	2.68	264,588	2.50
September	8.3	0.0	82,312	2.42	238,371	2.59	216,963	2.05
WY 2018 Total	102.6	390.1	1,691,474	49.75	3,992,475	43.40	2,563,668	24.19

Table 1(b). Precipitation and snowfall measured at the Syracuse Hancock International Airport and streamflow (Q) for all three monitoring sites for water year 2019.

Month	**Total Precip (cm)**	**Total Snowfall (cm)**	**Disconnected Headwater Total Q (m^3)**	**Disconnected Headwater Area-normalized Total Q (cm)**	**Transition Site Total Q (m^3)**	**Transition Site Area-normalized Total Q (cm)**	**Connected Outlet Total Q (m^3)**	**Connected Outlet Area-normalized Total Q (cm)**
October	10.6	0.0	81,238	2.39	297,732	3.24	177,888	1.68
November	16.1	57.9	225,252	6.63	406,863	4.42	149,567	1.41
December	8.3	37.3	88,731	2.61	416,896	4.53	158,248	1.49
January	8.3	83.8	180,249	5.30	440,204	4.78	147,188	1.39
February	7.2	69.1	123,421	3.63	427,026	4.64	136,673	1.29
March	4.1	37.6	116,861	3.44	397,176	4.32	157,237	1.48
April	8.8	6.4	78,573	2.31	386,397	4.20	246,260	2.32
May	16.5	0.0	119,114	3.50	571,106	6.21	416,014	3.92
June	11.2	0.0	135,650	3.99	500,869	5.44	440,095	4.15
July	8.6	0.0	111,953	3.29	317,567	3.45	415,587	3.92
August	13.2	0.0	128,008	3.76	352,790	3.83	409,476	3.86
September	8.9	0.0	86,843	2.55	214,119	2.33	263,628	2.49
WY 2019 Total	121.7	292.1	1,475,893	43.41	4,728,747	51.40	3,117,861	29.41

Table 2. Average monthly stream temperature for each monitoring site.

Water Year 2018				Water Year 2019			
Month	**Disconnected Headwater (°C)**	**Transition Site (°C)**	**Connected Outlet (°C)**	**Month**	**Disconnected Headwater (°C)**	**Transition Site (°C)**	**Connected Outlet (°C)**
October	15.21	14.78	13.91	October	11.76	12.64	12.48
November	6.48	7.08	8.35	November	5.46	6.26	7.35
December	2.56	2.33	4.57	December	3.77	4.32	6.44
January	1.90	1.50	3.45	January	1.38	1.75	4.18
February	3.97	3.55	5.44	February	1.81	2.11	4.67
March	5.50	4.82	6.33	March	3.95	4.32	5.75
April	7.53	7.43	8.38	April	9.74	9.93	9.99
May	17.20	16.89	14.14	May	14.46	14.29	12.80
June	19.64	20.01	16.00	June	19.30	18.75	15.52
July	24.34	23.78	18.98	July	23.37	23.23	17.96
August	23.26	23.10	19.09	August	21.97	21.53	18.07
September	19.95	20.23	17.62	September	18.72	18.52	16.20

Table 3. Average monthly chloride concentration for each monitoring site from grab samples. Grab samples were collected on an approximately weekly basis, although grab samples were not collected in November 2018.

Water Year 2018				Water Year 2019			
Month	**Disconnected Headwater (mg L^{-1})**	**Transition Site (mg L^{-1})**	**Connected Outlet (mg L^{-1})**	**Month**	**Disconnected Headwater (mg L^{-1})**	**Transition Site (mg L^{-1})**	**Connected Outlet (mg L^{-1})**
October	136	113	164	October	127	137	179
November	-	-	-	November	217	245	283
December	569	515	410	December	309	339	345
January	597	888	736	January	578	858	619
February	604	835	585	February	633	1072	652
March	673	1264	922	March	523	1293	684
April	257	322	319	April	353	393	365
May	246	272	302	May	246	283	268
June	231	247	294	June	254	296	344
July	179	214	267	July	254	257	350
August	157	212	272	August	205	232	340
September	118	154	180	September	203	228	289

Table 4. LOADEST model fit, variables, coefficient values, and variable significance for each monitoring site.

Site and Model R-Squared	**Model Variables**	**Coefficient Value**	**P-Value**
Disconnected Headwater	Ln(Q)	0.8039	<0.001
85.8%	sin(2*π*decimal time)	0.3569	<0.001
	cos(2*π*decimal time)	-0.3996	<0.001
	Snow depth	0.0543	<0.001
Transition Site	Ln(Q)	0.9759	<0.001
90.8%	$Ln(Q)^2$	-0.1655	<0.001
	cos(2*π*decimal time)	-0.1700	0.005
	Snow depth	0.0576	<0.001
	$Ln(Conductivity)^2$	0.0831	<0.001
Connected Outlet	Ln(Q)	0.8204	<0.001
72.0%	$Ln(Q)^2$	-0.1543	0.043
	sin(2*π*decimal time)	0.1783	0.018
	cos(2*π*decimal time)	-0.2573	<0.001
	Snow depth	0.0695	<0.001
	$Ln(Conductivity)^2$	0.0131	0.005

Table 5. Total and area-normalized chloride loads by water year for each monitoring site.

Site	**Chloride Load (kg)**	**Area-normalized Chloride Load (kg/km^2)**
Disconnected Headwater		
Mean Daily Load	1,351	397
95% Conf. Interval	1,214 – 1,499	357 – 441
WY 2018 Total	0.54×10^6	1.6×10^5
WY 2019 Total	0.45×10^6	1.3×10^5
Transition Site		
Mean Daily Load	5,609	610
95% Conf. Interval	5,011 – 6,258	545 – 680
WY 2018 Total	2.1×10^6	2.3×10^5
WY 2019 Total	2.0×10^6	2.2×10^5
Connected Outlet		
Mean Daily Load	2,596	245
95% Conf. Interval	2,422 – 2,779	228 – 262
WY 2018 Total	0.86×10^6	0.81×10^5
WY 2019 Total	1.0×10^6	0.98×10^5

Supplementary Information

S1. Stream Gauging Techniques

Streamflow measurements were collected at all sites using a SonTek-IQ Plus (IQ-Plus). The IQ-Plus uses four acoustic beams to measure stream velocity along the channel width and length and a fifth acoustic beam to measure channel depth. Channel depth is also measured using a pressure sensor, so that channel depth measurements are self-calibrating. Velocity and flow volume are calculated internally based on a user-supplied measurement of channel geometry and were recorded hourly during each deployment. At each site, the SonTek-IQ Plus was mounted to the bottom of a concrete culvert in close proximity to each automated stream gauging station for ease of calculating channel geometry. The manufacturer-listed velocity measurement accuracy of the IQ-Plus is +/- 1% of measured velocity or +/- 0.5 cm/s (SonTek 2017).

Efforts were made to capture the highest streamflow events by deploying the IQ-Plus at each site for several days during the late summer when large storm events are more common. The highest stage values recorded by the automated gauging stations during deployment of the IQ-Plus were higher than or equal to 97.9%, 99.8%, and 99.9% of observed stage values recorded throughout the two water years of the study at the disconnected headwater, transition site, and connected outlet, respectively. Additional streamflow measurements were taken using a SonTek/YSI FlowTracker Acoustic Doppler Velocimeter (ADV) at the connected outlet during the winter months because observed stage values at this particular site were lower at this time of the year than during the summer months when the IQ-Plus was deployed. ADV streamflow measurements at all three sites verify the IQ-Plus measurements at similar stages.

Final rating curves were constructed by pairing observed streamflow and stage measurements (Figure S1). At the disconnected headwater and transition sites, rating curve streamflow measurements were compiled solely from the IQ-Plus. At the connected outlet, the rating curve was compiled by using low flow measurements from the ADV and high flow measurements from the IQ-PLUS.

S2. Load Estimation

LOADEST allows users to make instantaneous estimates of the mass flux of a given chemical constituent from continuous measurements of streamflow and irregular, periodic measurements of concentrations. LOADEST uses linear regression to estimate the solution to the below equation:

$$Load = \Delta t \sum_{i=1}^{n} Q_i C_i \qquad \text{(Equation 1)}$$

where Q equals streamflow, C equals constituent concentration, Δt is a uniform interval of time, and n equals the number of points in time, even though measurements of Q and C are made at different frequencies.

Conceptually, LOADEST uses a linear regression approach to create a model of the log of instantaneous load based on a series of explanatory variables selected by the user, as in the following simplified equation:

$$\ln(Load) = a_0 + \sum_{i=1}^{n} a_i x_i \qquad \text{(Equation 2)}$$

where n is the number of user-selected explanatory variables with continuous data available, a_0 and a_i are model coefficients, and x is an explanatory variable. Because load is necessarily a function of streamflow, continuous streamflow measurements are included as one of the explanatory variables. Other variables can be included based on local hydrogeology and stream characteristics. Once a set of explanatory variables is chosen, the model is calibrated using a time series of observed constituent concentrations along with paired measurements of the explanatory variables using a regression approach to develop model coefficients. Finally, instantaneous load estimates are obtained for the full period of interest by exponentiating the above equation and using it in conjunction with the full time series of explanatory variables (Runkel *at al* 2004).

We included specific conductivity as a potential explanatory variable because it was measured continuously at the gauging stations and is often strongly correlated with chloride concentrations (Kelly *et al* 2019, Oswald *et al* 2019). Additional variables were also included in the LOADEST models if they were significant in estimating chloride load. For this study, explanatory variables were included in the final regression model for each site only when they were statistically significant ($p < 0.05$). These explanatory variables included centered decimal time and snow depth at all three sites and specific conductivity at the transition and connected outlet sites. Including a time element reflects the seasonal nature of road salt usage while changes in snow depth highlight specific times when road salt is more likely to be used. Different combinations and transformations of these variables were tested to create models with the highest R-squared at each site.

Because load estimation can result in a variety of biases, such as retransformation bias, Equation 2 is modified within LOADEST to include bias correction factors as described more fully in Runkel *et al* (2004). Two bias correction approaches within LOADEST are appropriate where model residuals are normally distributed: the Maximum Likelihood Estimation (MLE) and the Adjusted Maximum Likelihood Estimation (AMLE). A probability plot correlation coefficient (PPCC) close to 1.0 is indicative of a normal distribution (Runkel *et al* 2004). PPCC values calculated within LOADEST for the disconnected headwater and connected outlet were 0.996 and 0.993, respectively, both with significance levels of over 0.25. The PPCC value for the transition site of 0.985 has a significance level of 0.025 (Helsel and Hirsch 2002). For consistency across all sites and because AMLE is the primary estimation method used in LOADEST, load estimates in this study are reported using this method. Additionally, when constituent concentration data is uncensored, as is the case in this study, AMLE load estimates converge to MLE load estimates (Runkel et al 2004). Modeled AMLE load estimates are compared with observed loads in Figure S2.

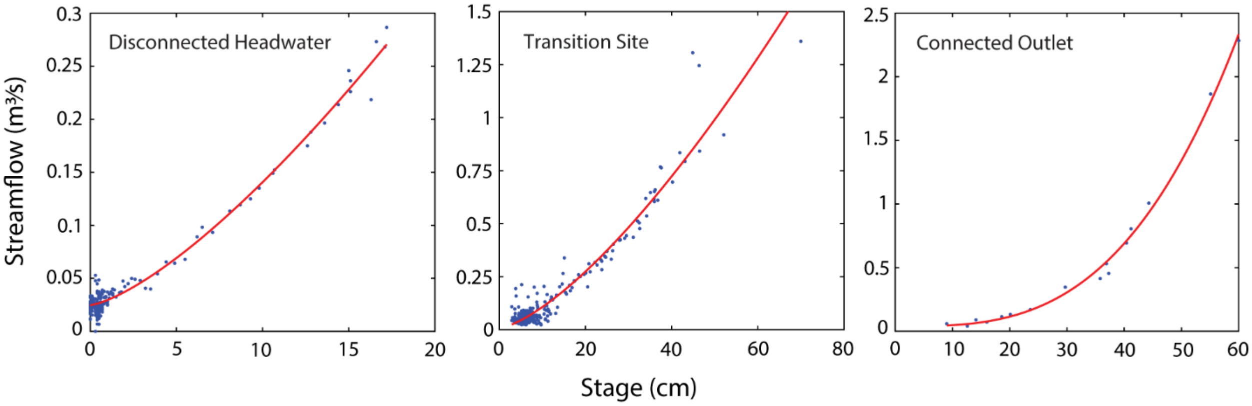

Figure S1. Rating curves used for the disconnected headwater, transition site, and connected outlet. Observation data are shown as blue dots.

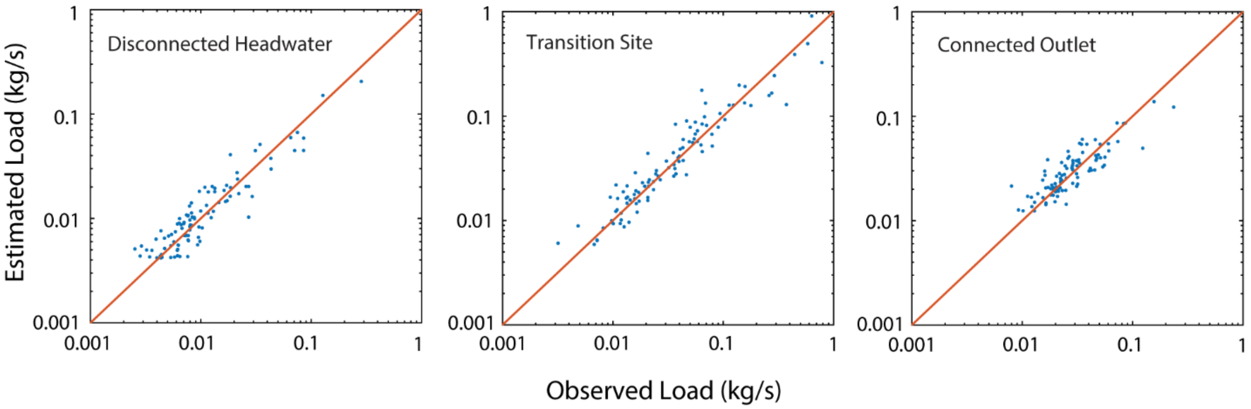

Figure S2. Modeled versus observed instantaneous loads for the disconnected headwater, transition site, and connected outlet with 1:1 line shown for comparison.

Table S1(a). Monthly load estimates and average chloride concentrations from LOADEST models for water year 2018. Monthly concentrations are calculated by dividing the monthly load estimate by the observed total streamflow for the month.

Month	**Disconnected Headwater Total Load (kg)**	**Disconnected Headwater Avg Cl^- ($mg\ L^{-1}$)**	**Transition Site Total Load (kg)**	**Transition Site Avg Cl^- ($mg\ L^{-1}$)**	**Connected Outlet Total Load (kg)**	**Connected Outlet Avg Cl^- ($mg\ L^{-1}$)**
October	26,407	157	37,441	135	45,480	212
November	27,468	212	57,369	187	36,457	237
December	43,624	407	174,552	830	48,962	401
January	143,573	482	374,806	705	93,022	479
February	63,258	498	386,804	934	78,654	506
March	81,201	561	589,314	1,148	130,374	650
April	44,779	340	155,263	359	72,972	336
May	21,411	277	97,652	331	109,904	351
June	24,595	201	66,189	275	65,596	296
July	23,383	152	57,088	199	66,545	229
August	16,087	141	52,737	214	56,444	213
September	13,297	162	42,580	179	50,823	234

Table S1(b). Monthly load estimates and average chloride concentrations from LOADEST models for water year 2019. Monthly concentrations are calculated by dividing the monthly load estimate by the observed total streamflow for the month.

Month	**Disconnected Headwater Total Load (kg)**	**Disconnected Headwater Avg Cl^- ($mg L^{-1}$)**	**Transition Site Total Load (kg)**	**Transition Site Avg Cl^- ($mg L^{-1}$)**	**Connected Outlet Total Load (kg)**	**Connected Outlet Avg Cl^- ($mg L^{-1}$)**
October	15,829	195	45,107	152	45,008	253
November	47,035	209	124,845	307	54,874	367
December	29,882	337	150,946	362	63,960	404
January	93,126	517	390,435	887	111,213	756
February	64,322	521	356,535	835	89,986	658
March	58,682	502	353,838	891	93,649	596
April	30,259	385	159,116	412	103,628	421
May	31,468	264	147,816	259	128,276	308
June	26,241	193	100,893	201	106,689	242
July	18,533	166	80,265	253	98,672	237
August	17,780	139	55,786	158	82,273	201
September	13,802	159	37,202	174	61,281	232

References

Arnott, S.E., Celis-Salgado, M.P., Valleau, R.E., DeSellas, A.M., Paterson, A.M., Yan, N.D., Smol, J.P., & Rusak, J.A. 2020. Road Salt Impacts Freshwater Zooplankton at Concentrations below Current Water Quality Guidelines. *Environmental Science & Technology*, 54: 9398-9407. https://doi.org/10.1021/acs.est.0c02396

Brown, C.J., Mullaney, J.R., Morrison, J., Martin, J.W., & Trombley, T.J. 2015. Chloride Concentrations, Loads, and Yields in Four Watersheds Along Interstate 95, Southeastern Connecticut, 2008-11 – Factors That Affect Peak Chloride Concentrations During Winter Storms. United States Geological Survey Scientific Investigations Report 2015-5057. https://doi.org/10.3133/sir20155057

Burakowski, E.A., Wake, C.P., Braswell, B., & Brown, D.P. 2008. Trends in wintertime climate in the northeastern United States: 1965-2005. *Journal of Geophysical Research: Atmospheres*, 113: D20114. https://doi.org/10.1029/2008JD009870

Cassanelli, J.P. & Robbins, G.A. 2013. Effects of Road Salt on Connecticut's Groundwater: A Statewide Centennial Perspective. *Journal of Environmental Quality*, 42: 737-748. https://doi.org/10.2134/jeq2012.0319

Chapra, S.C., Dove, A., & Rockwell, D.C. 2009. Great Lakes chloride trends: Long-term mass balance and loading analysis. *Journal of Great Lakes Research*, 35: 272-284. https://doi.org/10.1016/j.jglr.2008.11.013

City of Syracuse. 2010. Syracuse Housing Plan. Department of Neighborhood & Business Development and Bureau of Planning and Sustainability. 124 p. Available at:

http://www.syracuse.ny.us/uploadedFiles/Departments/CommunityDevelopment/Content/Documents/2010%20Syracuse%20Housing%20Plan.pdf

City of Syracuse. 2020. Snow Operations: How the City prepares for and cleans up after a snow event [accessed 2020 Mar 5]. http://www.syracuse.ny.us/snow-removal-operations.html

Coin, G. 2015. Snow job: 10,000 tons of it. The Post-Standard (Syracuse, New York). March 10, 2015. Page A-7.

Committee on the Comparative Costs of Rock Salt and Calcium Magnesium Acetate for Highway Deicing (CMA). 1991. Special Report 235: Highway Deicing: Comparing Salt and Calcium Magnesium Acetate. National Research Council, Transportation Review Board: Washington, DC.

Contosta, A.R., Casson, N.J., Garlick, S., Nelson, S.J., Ayres, M.P., Burakowski, E.A., et al. 2019. Northern forest winters have lost cold, snowy conditions that are important for ecosystems and human communities. *Ecological Applications*, 29(7): e01974. https://doi.org/10.1002/eap.1974

Cooper, C.A., Mayer, P.M., & Faulkner, B.R. 2014. Effects of road salts on groundwater and surface water dynamics of sodium and chloride in an urban restored stream. *Biogeochemistry*, 121: 149-166. https://doi.org/10.1007/s10533-014-9968-z

Corsi, S.R., De Cicco, L.A., Lutz, M.A., & Hirsch, R.M. 2015. River chloride trends in snow-affected urban watersheds: increasing concentrations outpace urban growth rate and are common among all seasons. *Science of the Total Environment*, 508: 488-497. https://doi.org/10.1016/j.scitotenv.2014.12.012

Duan, W., Takara, K., He, B., Luo, P., Nover, D., & Yamashiki, Y. 2013. Spatial and temporal trends in estimates of nutrient and suspended sediment loads in the Ishikari River, Japan, 1985 to 2010. *Science of the Total Environment*, 461-462: 499-508. https://doi.org/10.1016/j.scitotenv.2013.05.022

Dugdale, S.J., Malcolm, I.A., Kantola, K., & Hannah, D.M. 2018. Stream temperature under contrasting riparian forest cover: Understanding thermal dynamics and heat exchange processes. *Science of the Total Environment*, 610-611: 1375-1389. https://doi.org/10.1016/j.scitotenv.2017.08.198

Evans, D.M., Villamaga, A.M., Green, M.B., & Campbell, J.L. 2018. Origins of stream salinization in an upland New England watershed. *Environmental Monitoring and Assessment*, 190: 523 https://doi.org/10.1007/s10661-018-6802-4

Gabor, R.S., Hall, S.J., Eiriksson, D.P., Jameel, Y., Millington, M., Stout, T., et al. 2017. Persistent Urban Influence on Surface Water Quality via Impacted Groundwater. *Environmental Science and Technology*, 51: 9477-9487. https://doi.org/10.1021/acs.est.7b00271

Gardner, K.M. & Royer, T.V. 2010. Effect of Road Salt Application on Seasonal Chloride Concentrations and Toxicity in South-Central Indiana Streams. *Journal of Environmental Quality*, 39: 1036-1042. https://doi.org/10.2134/jeq2009.0402

Gutchess, K., Jin, L., Ledesma J.L.J., Crossman, J., Kelleher, C., Lautz, L., & Lu, Z. 2018. Long-Term Climatic and Anthropogenic Impacts on Streamwater Salinity in New York State: INCA Simulations Offer Cautious Optimism. *Environmental Science and Technology*, 52: 1339-1347. https://doi.org/10.1021/acs.est.7b04385

Gutchess, K., Jin, L., Lautz, L., Shaw, S.B., Zhou, X., & Lu, Z. 2016. Chloride sources in urban and rural headwater catchments, central New York. *Science of the Total Environment*, 565: 462-472. https://doi.org/10.1016/j.scitotenv.2016.04.181

Helsel, D.R., & Hirsch, R.M. 2002. Statistical Methods in Water Resources: U.S. Geological Survey Techniques of Water Resources Investigations, book 4, chapter A3. 510 p. https://doi.org/10.3133/twri04A3

Howard, K.W.F., & Maier, H. 2006. Road de-icing salt as a potential constraint on urban growth in the Greater Toronto Area, Canada. *Journal of Contaminant Hydrology*, 91: 146-170. https://doi.org/10.1016/j.jconhyd.2006.10.005

Huntington, J.L., & Niswonger, R.G. 2012. Role of surface-water and groundwater interactions on projected summertime streamflow in snow dominated regions: An integrated modeling approach. *Water Resources Research*, 48: W11524. https://doi.org/10.1029/2012WR012319

Jackson, R.B., & Jobbágy, E.G. 2005. From icy roads to salty streams. *Proceedings of the National Academy of Sciences of the United States of America*, 104(41): 14487-14488. https://doi.org/10.1073/pnas.0507389102

Jones, C.S. & Schilling, K.E. 2013. Carbon Export from the Raccoon River, Iowa: Patterns, Processes, and Opportunities. *Journal of Environmental Quality*, 42: 155-163. https://doi.org/10.2134/jeq2012.0159

Kaandorp, V.P., Doornebal, P.J., Kooi, H., Broers, H.P., & de Louw, P.G.B. 2019. Temperature buffering by groundwater in ecologically valuable lowland streams under current and future climate conditions. *Journal of Hydrology X*, 3: 100031. https://doi.org/10.1016/j.hydroa.2019.100031

Kantrowitz, I. 1964. Ground-water Resources of the Syracuse Area. New York State Geological Association 36th Annual Meeting Guidebook, Prucha J (ed). 36-38.

Kaushal, S.S. 2016. Increased Salinization Decreases Safe Drinking Water. *Environmental Science and Technology*, 50: 2765-2766. https://doi.org/10.1021/acs.est.6b00679

Kaushal, S.S., Groffman, P.M., Likens, G.E., Belt, K.T., Stack, W.P., Kelly, V.R., Band, L.E., & Fisher, G.T. 2005. Increased salinization of fresh water in the northeastern United States. *Proceedings of the National Academy of Sciences*, 102(38); 13517-13520. https://doi.org/10.1073/pnas.0506414102

Kelly, V.R., Findlay, S.E., Hamilton, S.K., Lovett, G.M., & Weathers, K.C. 2019. Seasonal and Long-Term Dynamics in Stream Water Sodium Chloride Concentrations and the Effectiveness of Road Salt Best Management Practices. *Water, Air, and Soil Pollution*, 230: 13. https://doi.org/10.1007/s11270-018-4060-2

Kelly, V.R., Lovett, G.M., Weathers, K.C., Findlay, S.E.G., Strayer, D.L., Burns, D.J., & Likens, G.E. 2008. Long-Term Sodium Chloride Retention in a Rural Watershed: Legacy Effects of Road Salt on Streamwater Concentration. *Environmental Science and Technology*, 42: 410-415. https://doi.org/10.1021/es071391l

Krause, S., Jacobs, J., Voss, A., Bronstert, A., & Zehe, E. 2008. Assessing the impact of changes in landuse and management practices on the diffuse pollution and retention of nitrate in a riparian floodplain. *Science of the Total Environment*, 389: 149-164. https://doi.org/10.1016/j.scitotenv.2007.08.057

Lam, W.Y., Lembcke, D., & Oswald, C. 2020. Quantifying chloride retention and release in urban stormwater management ponds using a mass balance approach. *Hydrological Processes*, 34(23): 4459-4472. https://doi.org/10.1002/hyp.13893

Ledford, S.H., Lautz, L.K., Vidon, P.G., & Stella, J.C. 2017. Impact of seasonal changes in stream metabolism on nitrate concentrations in an urban stream. *Biogeochemistry*, 133: 317-331. https://doi.org/10.1007/s10533-017-0336-7

Ledford, S.H., Lautz, L.K., & Stella, J.C. 2016. Hydrogeologic Processes Impacting Storage, Fate, and Transport of Chloride from Road Salt in Urban Riparian Aquifers. *Environmental Science and Technology*, 50: 4979-4988. https://doi.org/10.1021/acs.est.6b00402

Ledford, S.H., & Lautz, L.K. 2015. Floodplain connection buffers seasonal changes in urban stream water quality. *Hydrologic Processes*, 29: 1002-1016. https://doi.org/10.1002/hyp.10210

Lehman, J.T. 2018. Variable retention times and in-stream nutrient sinks. *Lake and Reservoir Management*, 34(1): 1-6. https://doi.org/10.1080/10402381.2017.1402227

Marsalek, J. 2003. Road salts in urban stormwater: an emerging issue in stormwater management in cold climates. *Water Science and Technology*, 48(9): 61-70.

Menichino, G.T., & Hester, E.T. 2014. Hydraulic and thermal effects of in-stream structure-induced hyporheic exchange across a range of hydraulic conductivities. *Water Resources Research*, 50: 4643-4661. https://doi.org/10.1002/2013WR014758

Meriano, M., Eyles, N., & Howard, K.W.F. 2009. Hydrogeological impacts of road salt from Canada’s busiest highway on a Lake Ontario watershed (Frenchman’s Bay) and lagoon, City of Pickering. *Journal of Contaminant Hydrogeology*, 107: 66-81. https://doi.org/10.1016/j.jconhyd.2009.04.002

Muller, E. 1964. Surficial Geology of the Syracuse Field Area. New York State Geological Association 36th Annual Meeting Guidebook, Prucha J (ed). 25-35.

Novotny, E.V., Sander, A.R., Mohseni, O., & Stefan, H.G. 2009. Chloride ion transport and mass balance in a metropolitan area using road salt. *Water Resources Research*, 45: W12410. https://doi.org/10.1029/2009WR008141

Oswald, C.J., Giberson, G., Nicholls, E., Wellen, C., & Oni, S. 2019. Spatial distribution and extent of urban land cover control watershed-scale chloride retention. *Science of the Total Environment*, 652: 278-288. https://doi.org/10.1016/j.scitotenv.2018.10.242

Park, Y.S. & Engel, B.A. 2015. Analysis for Regression Model Behavior by Sampling Strategy for Annual Pollutant Load Estimation. *Journal of Environmental Quality*, 44: 1843:1851. https://doi.org/10.2134/jeq2015.03.0137

Patykowski, J., Kolodziejek, J., & Wala, M. 2018. Biochemical and growth responses of silver maple (Acer saccharinum L.) to sodium chloride and calcium chloride. *PeerJ*, 6: e5958. https://doi.org/10.7717/peerj.5958

Payn, R.A., Gooseff, M.N., McGlynn, B.L., Bencala, K.E., & Wondzell, S.M. 2009. Channel water balance and exchange with subsurface flow along a mountain headwater stream in Montana, United States. *Water Resources Research*, 45: W11427. https://doi.org/10.1029/2008WR007644

Paul, M.J. & Meyer, J.L. 2001. Streams in the Urban Landscape. *Annual Review of Ecological Systems*, 32: 333-365. https://doi.org/10.1146/annurev.ecolsys.32.081501.114040

Pieper, K.J., Tang, M., Jones, C., Weiss, S., Greene, A., Mohsin, H., Parks, J., & Edwards, M.A. 2018. Impact of Road Salt on Drinking Water Quality and Infrastructure Corrosion in Private Wells. *Environmental Science and Technology*, 52: 14078-14087. https://doi.org/10.1021/acs.est.8b04709

Pinder, G.F. & Sauer, S.P. 1971. Numerical Simulation of Flood Wave Modification Due to Bank Storage Effects. *Water Resources Research*, 7: 63-70. https://doi.org/10.1029/WR007i001p00063

Ramakrishna, D.M. & Virarghavan, T. 2005. Environmental Impact of Chemical Deicers – A Review. *Water, Air, and Soil Pollution*, 166: 49-63. https://doi.org/10.1007/s11270-005-8265-9

Robinson, H.K. & Hasenmueller, E.A. 2017. Transport of road salt contamination in karst aquifers and soils over multiple timescales. *Science of the Total Environment*, 603-604: 94-108. https://doi.org/10.1016/j.scitotenv.2017.05.244

Runkel, R.L., Crawford, C.G., & Cohen, T.A. 2004. Load Estimator (LOADEST): A FORTRAN Program for Estimating Constituent Loads in Streams and Rivers. United States Geological Survey Techniques and Methods Book 4, Chapter A5. https://doi.org/10.3133/tm4A5

Shaw, S.B., Marjerison, R.D., Bouldin, D.R., Parlange, J., & Walter, M.T. 2012. A Simple Model of Changes in Stream Chloride Levels Attributable to Road Salt Applications. *Journal of Environmental Engineering*, 138(1): 112-118. https://doi.org/10.1061/(ASCE)EE.1943-7870.0000458

Squier-Babcock, M. & Davidson, C.I. 2020. Hydrologic Performance of an Extensive Green Roof in Syracuse, New York. *Water*, 12: 1535. https://doi.org/10.3390/w12061535

Stets, E.G., Lee, C.J., & Schock, M.R. 2018. Increasing chloride in rivers of the coterminous U.S. and linkages to potential corrosivity and lead action level exceedances in drinking water. *Science of the Total Environment*, 613-614: 1498-1509. https://doi.org/10.1016/j.scitotenv.2017.07.119

SonTek. 2017. SonTek-IQ®Series Intelligent Flow Featuring Smart Pulse^{HD} User's Manual.

U.S. Environmental Protection Agency (USEPA). 1988. Ambient Water Quality Criteria for Chloride – 1988 (Washington, DC). Available from: https://www.epa.gov/wqc/aquatic-life-ambient-water-quality-criteria-chloride-1988

Walsh, C.J, Roy, A.H., Feminella, J.W., Cottingham, P.D., Groffman, P.M., & Morgan, R.P. 2005. The urban stream syndrome: current knowledge and the search for a cure. *Journal of the North American Benthological Society*, 24(3): 706-723. https://doi.org/10.1899/04-028.1

Weiner G. 2000. City, CNY set for salt as snow peppers area. The Post-Standard (Syracuse, New York). December 29, 2000. Page C-3.

Winkley S. 1989. The Hydrogeology of Onondaga County, New York. M.S. Thesis. Syracuse University, Syracuse, New York. 172 p.

Chapter 2

Contrasting Impacts of a Hotter and Drier Future on Streamflow and Catchment Scale Sediment Flux in the High Andes

Chapter 2 has been submitted for publication to *Journal of Geophysical Research: Earth Surface*

Abstract

Fluvial sediment transport in high mountain regions is uniquely sensitive to changes in hydroclimate that alter the timing and magnitude of streamflow contributions from snowmelt, glaciers, and other cryoforms. In the high Andes of Argentina and Chile, mountain river systems serve millions of people in foothill communities and large metropolitan areas alike, yet these same rivers can also carry high sediment loads that compromise water quality and infrastructure. Regional climate predictions are also increasingly forecasting a warmer and drier future that is likely to alter hydrologic regimes and sediment transport dynamics. This study utilizes hydrologic modeling techniques to propagate a suite of endmember climate projections to estimate changes in streamflow and consequent impacts on catchment scale sediment transport on both the Argentine and Chilean sides of the high Andes. Results show reductions in streamflow of up to 57% under scenarios with reduced precipitation and even larger decreases in sediment flux, while outcomes under a warming scenario with no changes to precipitation are highly variable. Study results further show that high winter streamflow events may increase in magnitude in Chile while mountain communities in Argentina may increasingly face water shortages. These results indicate that different adaptation and mitigation strategies may be needed on either side of the Andes in response to a changing hydroclimate.

1. Introduction

Warming temperatures and future changes in precipitation across high mountain regions will have cascading effects through fluvial networks affecting the timing and magnitude of sediment exported from high relief catchments. These regions are uniquely sensitive to hydroclimatological changes due to the important contributions of glaciers, snow, and other cryoforms to fluvial sediment transport networks and the regulation of these processes by air temperature (Hirschberg et al., 2021; East & Sankey, 2020; Wulf et al., 2012). While efforts to quantify the impacts of climate change on sediment fluxes from mountain and higher altitude regions have increased in recent years (e.g., Hirschberg et al., 2021; Li et al., 2021; Li, D., et al., 2020; Wulf et al., 2012), efforts to understand these processes in the high Andes Mountains of Argentina and Chile are still relatively sparse (e.g., Carrillo & Mao, 2020).

High relief, tectonically active mountainous regions like the Andes, where non-volcanic peaks reach altitudes of over 6000 m, can generate significant quantities of sediment. Although suspended sediments from these areas help deliver important mineral nutrients to downstream ecological communities (McClain & Naiman, 2008), excess sediment loads can have negative impacts on aquatic environments. High sediment loads can impair aquatic biota (Bilotta & Brazier, 2008) and transport high concentrations of heavy metals (Dawson & Macklin, 1998), a particular concern for the copper rich Andes. Excess sediment loads also pose problems for human consumption and infrastructure, requiring costly removal from drinking water sources (Bilotta & Brazier, 2008) and accumulating behind dams and reservoirs (Snyder et al., 2004). These impacts potentially pose threats to existing and projected critical infrastructure in and adjacent to the high Andes, where several large dams have been built due to limited freshwater resources. In these areas, feasibility studies for additional dams are already underway.

Sediment export in in the high Andes is strongly seasonal and closely connected with fluvial processes (Carrillo & Mao, 2020; Mao & Carrillo, 2017; Pepin et al., 2010). Snowmelt is the primary source of streamflow in the high mountains, although high elevation glaciers buffer streamflow during warmer and drier times of the year (Ayala et al., 2020; Carrillo & Mao, 2020; Crespo et al., 2020; Masiokas et al., 2006). Mountain rivers also support a thriving agricultural sector, hydropower generation, and millions of people living in foothill communities, including the major metropolitan areas of Mendoza and Santiago (Crespo et al., 2020; Masiokas et al., 2006).

As the timing and amount of annual runoff in the high Andes depends heavily on snowfall and glacier melt, water resources in the area are sensitive to changing climate (Ragettli et al., 2016; Viviroli et al., 2011; Cortés et al 2011). Researchers have observed rising air temperatures as well as shrinking snowpack and glacier mass over the last several decades in the high Andes (Ayala et al., 2020; Dussaillant et al., 2019). These trends are anticipated to persist in future decades, with increases of 1.2 to 4.0°C in mean annual temperature and decreases of 3 to 30% in mean annual precipitation predicted for catchments in the high Andes by end of the twenty-first century (Bozkurt et al., 2018; Vicuña et al., 2011). In addition, glaciers in the high Andes are estimated to have passed the point where further increases in temperature will lead to increases in streamflow from glacier melt, with glaciers already receding at high elevations (Ragettli et al., 2016). Under a hypothetical constant climate scenario, glacier mass reductions of nearly 20% were predicted for some parts of the high Andes by the end of the twenty-first century (Ayala et al., 2020), although these numbers climb to 70% under higher emissions scenarios (Ragettli et al., 2016). Likewise, annual runoff is predicted to decrease by 2 to 3% under lower emissions scenarios and by as much as 40 to 62% under higher emissions scenarios (Bozkurt et al., 2018, Ragettli et al., 2016). These changes are all likely to have concomitant impacts on water quality and sediment export.

Quantifying how changing climate and streamflow patterns may impact sediment flux can help anticipate mitigation needs for downstream communities, such as infrastructure changes or measures to preserve water quality. Climate can strongly influence erosion and sediment transport (Carrillo & Mao, 2020; Starke et al., 2020; Carretier et al., 2013), although few studies to date have considered the impacts of climate change on sediment flux in the high Andes (Carrillo & Mao, 2020). Due to the interconnected nature of sediment flux and fluvial processes in the region (Carrillo & Mao, 2020; Mao & Carrillo, 2017; Pepin et al., 2010), quantifying climate-induced shifts in hydrology can be a key to understanding future changes in sediment transport. In mountainous environments, these shifts include changes in the proportion of precipitation occurring as rain versus snow and loss of seasonal snow cover at lower elevations, altering the magnitude and timing of sediment delivery to stream channels (Iida et al., 2012).

Because the Andes act as an orographic barrier to precipitation originating from the Pacific (Masiokas et al., 2006), the western and eastern sides of the Andes have distinct climate regimes, potentially necessitating different responses to climate change. This study utilizes hydrologic models of eight catchments in the high Andes of Argentina and Chile to predict how streamflow will behave in an environment that is warmer, drier, or warmer and drier. Outputs from these models are utilized to analyze how sediment transport through fluvial systems might change in comparison to a modern baseline period. The results offer insights into how broad shifts in precipitation or temperature trends may impact different parts of the Andes with contrasting hydroclimatologies.

2. Methods

2.1. Study Region

The study region encompasses eight catchments in the high Andes – four in Argentina and four in Chile – ranging from approximately 32° to 35° S (Figure 1). Catchments were selected based on the availability of paired streamflow and sediment flux data from gauge station sites. No dams are located within the contributing areas of any of the catchments. Each catchment outlet was defined using the location of its respective stream gauge station (Table 1). Catchment boundaries were delineated using a D8 flow routing algorithm in ESRI ArcGIS 10.7 (ArcGIS) using the Shuttle Radar Topography Mission (STRM) 1 arc second digital elevation model (DEM). Gaps in the SRTM DEM were filled using the International Centre for Tropical Agriculture 250 m DEM (Jarvis et al., 2008).

National agencies in both Argentina and Chile collect streamflow and sediment data. These data were obtained in Argentina from the Base de Datos Hidrilógica Integrada (BDHI, 2020; SMRH, 2021), a publicly available resource maintained by the Secretaría de Infraestructura y Política Hídrica de la Nación. Streamflow data for the Chilean catchments were obtained from the Catchment Attributes and MEteorology for Large-sample Studies dataset in Chile (CAMELS_CL) (Alvarez-Garreton et al., 2018), which includes a compilation of data from stream gauges maintained by the Dirección General de Aguas de Chile (DGA). Suspended sediment load data for Chile were obtained from the DGA (DGA, 2020).

The eight study catchments range in size from approximately 1000 to 7000 km^2 and encompass elevations ranging from 573 m to 6961 m (Table 1). The catchments generally have either sparse or no vegetation, although there are small regions of shrubland or herbaceous vegetation near some trunk streams and at lower elevations (Buchhorn et al., 2019). Glaciers are present at higher elevations, but do not exceed 10% of the total area of any single watershed (Table 1; RGI Consortium, 2017). Across the study region, precipitation broadly increases from north to south (Bozkurt et al., 2018) and from lower to higher elevations (Vicuña et al., 2011), with the western side of the Andes receiving more annual precipitation than the eastern side (Masiokas et al., 2006). In the Mediterranean climate of central Chile (Pepin et al., 2010), precipitation is winter-dominated, and increases from 290 mm annually in Santiago at 33° S in the Central Valley (Masiokas et al., 2006) to over 1500 mm annually between 35° and 36° S on the western slopes of the Andes (Bozkurt et al., 2018). Winter storms in Chile can be severe, sometimes delivering over 100 mm of precipitation in a single event (Viale & Norte 2009). In Argentina, precipitation during the winter months spills over from the west at higher elevations. A different pattern prevails during the summer in the eastern Andes, with precipitation increasing at lower elevations due to convective storms and moist air masses originating from the northeast (Viale & Nuñez, 2011; Masiokas et al., 2006). Annual precipitation also exhibits significant interannual variability on either side of the range, with higher annual precipitation associated with El Niño events and lower annual precipitation associated with La Niña (Bozkurt et al., 2018; Cortés et al., 2011; Masiokas et al., 2006). Previous estimates of catchment-averaged erosion rates in the high Andes approach 0.30 mm/a and are identical within uncertainty using either ^{10}Be or stream gauge data (Val et al., 2018; Carretier et al., 2013). Erosion rates reflect tectonic processes within the region and are highest between 33° and 34° S (Starke et al., 2020; Val et al., 2018; Carretier et al., 2013).

2.2. Hydrologic Models

Simulations and predictions of were generated streamflow using the Hydrologiska Byråns Vattenavdelning (HBV) catchment-runoff model (Bergström, 1992; Seibert & Vis, 2012). While there are many versions of HBV, this study implemented a semi-distributed framework with 15 parameters and requiring daily precipitation, temperature, and potential evapotranspiration (PET) as inputs and producing streamflow as output for a given catchment. To account for the impact of elevation on snow accumulation and melt, each modeled catchment was divided into a series of 500 m vertical elevation bands in ArcGIS. Within each band, precipitation falls as snow at elevations where the observed temperature is below a specified threshold temperature (model parameter), typically close to 0°C. Precipitation stored as snow melts at a rate determined by the degree-day factor (model parameter) when the temperature exceeds this threshold. Melt is then treated (like rainfall) as an input to a soil moisture store, which is routed to subsurface stores before finally being routed to streamflow. Figure 2 shows a conceptual diagram of the HBV model used in this study. Additional information on model mechanics is available in supplementary information.

Climate data for the Argentine and Chilean catchments were obtained using similar methods, where practicable. For Chile, all climate data and a variety of watershed attributes were obtained via CAMELS_CL (Alvarez-Garreton et al., 2018). Precipitation data for the Argentine catchments were compiled using the Climate Hazards Group InfraRed Precipitation with Stations database (CHIRPS), which provides daily precipitation estimates at a 0.05° resolution (Funk et al., 2015) and has been validated by other studies in the high Andes (Rivera et al., 2018). These data were clipped to the Argentine catchments and averaged to create a single daily value per catchment. CHIRPS data for the Chilean catchments were obtained via the CAMELS_CL database. For Argentina, air temperature data were compiled from individual gauging stations within or in close proximity to each catchment. The national CR2MET dataset, accessed via CAMELS_CL, was used for daily air temperature data for Chile. Monthly PET values for the Argentina catchments were calculated using the Thornthwaite method (Thornthwaite & Mather, 1955) applied to gauge station air temperature observations. For the Chilean catchments, monthly PET data were obtained from a temperature-based compilation via CAMELS_CL. Temperature inputs to the HBV models were scaled vertically across each catchment elevation band using a lapse rate of 0.6°C per 100 m, similar to observed average lapse rates in the region (Ibañez et al., 2020). A precipitation gradient of 10% per 100 m was used to reflect orographic effects in the Andes (Viale & Garreaud, 2015).

Because all of the catchments except the Río Choapa contain glaciers, a simple glacier model was coupled to the HBV framework to account for the glacier contribution to streamflow. For the Argentine catchments, the extent of glacial coverage within each catchment was calculated using the Randolph Glacier Inventory (v. 6.0; RGI Consortium, 2017). For the Chilean catchments, these data were obtained from CAMELS_CL. The glacier area was then divided into elevation bands using the same methods as for the HBV routine. In the model, glaciers produce meltwater whenever the temperature rises above a temperature threshold (equivalent to the melt threshold for snow) at a rate equal to a calibrated melt coefficient multiplied by the glacier area. Glacier melt is routed directly to streamflow. In models of future streamflow coupled with reductions in glacier area, total glacier area was reduced by a specified percentage based on assumptions for a given climate outcome. This reduction was achieved by removing glacier coverage from the lowest elevation band containing glacier mass in each catchment until the total glacier area in that elevation band was removed. This process was repeated through progressively higher elevation bands until the total specified percentage reduction was achieved.

2.3. Model Calibration

Models were calibrated to observed streamflow for each catchment using a baseline period of April 1, 2005 to March 31, 2015. The period of April 1 through March 31 corresponds to the regional water year (Alvarez-Garreton et al., 2018, Cortés et al., 2011). This baseline period includes the 2010-2015 “mega drought” in the high Andes (Rivera et al., 2017, Garreaud et al., 2017), which enabled model calibration to both wet and dry years. Daily observed streamflow records were at least 85% complete for all catchments during this interval. An initial set of model parameters for each catchment was optimized using a Genetic Algorithm and Powell (GAP) optimization routine, as described in supplementary information. To account for potential equifinality (i.e., different combinations of parameters generating equivalent performance metrics), 2000 parameter sets were then generated using Latin hypercube sampling from ranges of +/- 30% applied to optimized parameter values (to the extent allowable within individual parameter limits in HBV) and corresponding simulations for the baseline period. Within each catchment, the top 100 parameter sets were identified corresponding to the highest Nash-Sutcliffe efficiency (NSE) (Nash & Sutcliffe, 1970). The top 100 values for the glacier melt coefficient were determined similarly, based on Latin hypercube sampling of 1000 values evaluated and ranked based on NSE from an initial parameter space determined through trial and error. These top 100 parameter sets were used as the basis for subsequent scenario analysis. Instead of using a single, optimized parameter set, multiple parameter sets were included to account for parameter uncertainty as well as uncertainty introduced when modeling future periods based on historical performance. NSE was selected as the primary error metric based on visual observation of model performance and the strong seasonality of the annual hydrographs. Kling-Gupta efficiency (KGE) was calculated as a secondary error metric (Gutpta et al., 2009). The selected parameter sets were assumed to captured historical variability and used to predict streamflow response to future climate scenarios (Singh et al., 2014). Additional details on the calibration routine and error metrics are included in supplementary information.

2.4. Scenario Analysis

Three end-member climate scenarios were used to model changes in streamflow and sediment flux based on temperature and precipitation forecasts for the region reported in prior studies (Bozkurt et al., 2018; Vicuña et al., 2011). Although exact dates are not assigned to these climate outcomes, the precipitation and temperature forecasts are keyed to expectations under higher emissions scenarios by the end of the twenty-first century. Three scenarios are used due to uncertainty as to whether changes in precipitation, temperature, or both will dominate. The drier scenario models a 30% reduction in mean annual precipitation but no change in mean annual temperature. This scenario includes a 20% reduction in total glacier area based on prior work in the region modeling glacier retreat under steady-state assumptions (Ayala et al., 2020). The drier and warmer scenario models a 30% reduction in mean annual precipitation coupled with 4°C mean annual temperature increase. Finally, the warmer scenario features a 4°C mean annual temperature increase but no change in mean annual precipitation. In both the drier and warmer scenario and the warmer scenario, total glacier area is reduced by 70%, an assumption in line with projections for the region based on higher IPCC emissions scenarios (Ragettli et al., 2016).

For each scenario and for each catchment, 50 time series of daily weather data were created using the daily stochastic weather generator WeaGETS, which also simulates interannual variability (Chen et al., 2012). Observed daily weather data for the baseline period were used as inputs to the weather generator, uniformly modified by the increases in temperature or decreases in precipitation noted above, both for simplicity and based on prior modeling work showing that decreases in precipitation occurred in each month of the year under higher emissions scenarios (Bozkurt et al., 2018). The top 100 parameter sets were combined with the 50 climate time series generated for each scenario, resulting in 5,000 simulations of streamflow for each climate scenario per catchment.

2.5. Hydrologic Signatures and Erosion Rates

To obtain a holistic view of how changes to precipitation and temperature alter streamflow dynamics in each watershed, several hydrologic signatures were calculated for the baseline period and for each future modeled time series of streamflow. These signatures include:

- The highest observed daily discharge for each time series, as these events can be particularly important for transporting sediment (Molnar et al., 2006, Leopold et al., 1964).
- The center of volume (Court, 1962), to investigate how warming temperatures affect streamflow timing due to snow and glacier melt. This was calculated as the day, beginning with the April 1 water year, on which half of the total streamflow for a given water year passes the catchment gauge station (Court, 1962).
- Unit stream power (Bagnold, 1966), a metric of each stream's ability to perform geomorphic work, using the following formulation:

$$\omega = \frac{\Omega}{channel\ width} = \frac{\rho g Q S}{channel\ width} \quad \text{(Eq 1)}$$

where ω is unit stream power (W m^{-2}), Ω is total stream power (W m^{-1}), ρ is the density of water (1000 kg m^{-3}), g is gravitational acceleration (9.8 m s^{-2}), Q is streamflow (m^3 s^{-1}), and S is the slope of the streambed (m m^{-1}) (Bagnold, 1966). Streambed slope was calculated in ArcGIS by measuring the change in elevation along a ~500 m long stream channel segment centered on each gauge station location and channel width was assessed using satellite imagery.

- The average position of the 0°C isotherm during the winter months, to interpret how warming temperatures affect the distribution of rain versus snow events. Observed temperature data from the baseline period and simulated temperature data for the warming scenarios were used in these calculations. Following other regional studies, the winter season is defined as June through September (JJAS) (Rusticucci et al., 2014).
- The relative change in catchment areas exposed to temperatures above freezing, on average, from the baseline period to the warming scenarios, calculated by comparing the change in the location of the JJAS 0°C isotherm in each catchment to the respective catchment hypsometry derived from ArcGIS.
- The average slope of each catchment below the baseline period JJAS 0°C isotherm and for the area between the baseline period JJAS 0°C isotherm and warming scenario JJAS 0°C isotherms, to investigate areas of potential slope instability.
- Erosion rates, calculated using observed and simulated hydrographs and sediment rating curves developed for each catchment (Li, L., et al., 2020; Gao, 2008; Runkel et al., 2004), as a normalized metric of sediment flux and for ease of comparison with prior studies. A power law fit was applied to paired river discharge and sediment load data per catchment and then applied to streamflow for the baseline period and model outputs, using the following formulation:

  $$Q_s = aQ^b \qquad \text{(Eq 2)}$$

  where Q_s is sediment flux, Q is streamflow, and a and b are rating curve parameters (Gao, 2008). Other researchers in the region have followed this approach using similar datasets (Val et al., 2018). Rating curves were corrected for bias, as appropriate, using methods described in supplementary information (Runkel et al., 2004; Ferguson, 1986).

3. Results

3.1. Water Year 2005-2014 Climate Variables and Streamflow

Precipitation, temperature, and streamflow data for the baseline period are representative of the climate characteristics across the study region. Monthly averaged precipitation was higher and peaked during the winter months in Chile, while average precipitation was lower in Argentina (Figure 3, Table 1). On both sides of the Andes, precipitation generally increased heading south. Following the winter season, average monthly streamflow increased during the austral spring in association with snowmelt and peaked during the summer, although peak flows arrived earlier in the unglaciated Río Choapa catchment. Peaks in average monthly sediment flux were strongly correlated with streamflow and, with the exception of the Río Tinguiririca, very little sediment was transported in the fluvial system from April through October (Figure 3).

Hydrographs for all eight catchments reflect the snowmelt-dominated regime of each basin (Figure 4). On both sides of the range, the catchments with the highest mean elevations also generally had the greatest total glacier contribution to streamflow by volume (Tables 1, 2). Total annual streamflow showed an observable decline in each catchment starting around water year 2010, coincident with the regional "mega-drought" spanning from 2010-2015.

In Chile, there were several large, singular discharge events that are distinct from the sustained snowmelt portion of the annual hydrograph. These events were pronounced in the Río Colorado, Río Aconcagua, and Río Tinguiririca catchments and appear to occur nearly simultaneously in all three catchments. In the case of the Río Tinguiririca, discharge associated with these events in some cases exceeded the maximum daily discharge associated with the snowmelt portion of the hydrograph. One such event on August 27, 2005 is coincident with a large and well-documented winter storm that caused landsliding at lower elevations, flooding in Santiago, and led to the evacuation of city residents (Viale & Norte, 2009). Such singularly large discharge events are not as evident in the Argentine hydrographs.

Visually, the models of streamflow for the baseline period from the top 100 parameter sets are similar to observed annual patterns of streamflow for the different catchments (Figure 4). Model performance is summarized for all catchments in Table 2. Observed mean annual streamflow and maximum daily streamflow values for the baseline period were within the range of modeled values for nearly all catchments (Tables 2, S5). The highest NSE values for the top 100 simulations ranged from 0.61 (Río Tinguiririca) to 0.80 (Río Atuel); the highest performing KGE values ranged from 0.75 (Rio Aconcagua) to 0.89 (Río Atuel; Table 2).

3.2. Future Climate Scenario Streamflow Simulations

Future simulations broadly show reductions in streamflow for all scenarios (Table 2). Reductions are highest for the drier and warmer scenario. Average annual streamflow reductions under this scenario range from -36% to -57%, with higher reductions observed on the drier Argentine side of the range. Reductions in streamflow under the drier scenario are also large, ranging from -33% to -44%. The reductions in streamflow under the drier scenario and drier and warmer scenario exceed the 30% reduction in precipitation used in these scenarios.

Reductions in annual streamflow are considerably more variable for the warmer scenario. On the drier Argentine side of the range, predicted streamflow reductions range from -19% to -32% for the four catchments. In contrast, streamflow reductions on the wetter, winter-precipitation driven Chilean side are modest, ranging from -11% for the Río Aconcagua to -2% for the Río Tinguiririca. In the Río Choapa catchment, which does not contain glaciers and therefore did not lose this important water supply, average annual streamflow increases under the warmer scenario by 13%. Changes in streamflow in the future scenarios are mirrored by reductions in unit stream power for nearly all of the catchments, with a modest increase in unit stream power for the Río Choapa under the warmer scenario (Figure 5a, Table S6).

Maximum daily stream discharge decreases in the drier scenario and drier and warmer scenario for all catchments except the Río Tinguiririca (Figure 5b, Table S5). These decreases are more modest in the wetter Chilean catchments as compared to the Argentine catchments. In contrast, there is more variability in maximum discharge events under Scenario 3. For the Chilean catchments, these events are also typically larger in magnitude. For all of the Chilean catchments, the median from the range of maximum daily discharge events under Scenario 3 is higher than the baseline period. The very highest maximum daily discharge events from the range of Scenario 3 simulations is also nearly twice as high as the Scenario 3 medians. While the Argentine catchments also displayed increased variability in maximum discharge under the warmer scenario, these changes are more modest compared to those in Chile. Indeed, the median from the range of maximum discharge events under Scenario 3 is lower for the Argentine catchments than the baseline period.

3.3. Center of Volume and 0°C Isotherm

As compared to baseline conditions, the center of volume timing (averaged across all simulations) is predicted to shift earlier in the year for all scenarios on both sides of the Andes (Figure 5c, Table S7). This shift is modest for a drier future, but more pronounced for both warming scenarios. For all of the Argentine catchments combined, results predict that the median of the average center of volume will arrive one week earlier for the drier scenario and five weeks earlier for both warming scenarios as compared to baseline. This earlier shift in the center of volume is more pronounced for the Chilean catchments. In these catchments, the center of volume is predicted to arrive approximately three weeks earlier for the drier scenario and eight weeks earlier for both warming scenarios.

Model-predicted changes to center of volume timing associated with both future warming scenarios are predicted to be accompanied by a several hundred meters retreat in the JJAS 0°C isotherm for all catchments (Figure 6). Based on the hypsometry of each watershed, this exposes an average of 19% to 36% of total catchment area to temperatures above freezing during the period when precipitation is more likely to fall as snow today; the magnitude of these changes are similar for both the Argentine and Chilean catchments. The topographic slope of this newly exposed area is also steeper for 75% of the catchments than the area below the average JJAS 0°C isotherm for the baseline period. For all catchments, the average slope of the newly exposed area is over 20°; for five catchments, the average slope exceeds 25° (Table S9).

3.4. Sediment Fluxes and Erosion Rates

Baseline erosion rates calculated using observed streamflow are highest for the Río Colorado on the Chilean side of the range and the Río Tunuyán on the Argentine side of the range and decrease to the north and south (Figure 7, Table S8). Median erosion rates calculated using the simulated streamflow time series for the baseline period are within error of the erosion rates calculated with observed streamflow data. The erosion rates calculated using modeled streamflow reproduce the trends calculated from observed streamflow from the baseline period.

Under future climate scenarios, reductions in streamflow and stream power in the drier scenario (-30% precipitation) and drier and warmer scenario (-30% precipitation + 4°C) propagate into large declines in sediment fluxes and erosion rates in every catchment (Figure 7, Table S8). Declines are largest on the drier Argentine side of the Andes, ranging from 77 to over 90% as compared to baseline. Even on the Chilean side of the Andes, declines in erosion rates still range from 44 to 77%. The range of these predicted erosion rates is impressively narrow under these two scenarios.

The warmer scenario (+ 4°C) produced variable responses with a greater range than both wetter future scenarios, reflecting increased variability in streamflow, stream power, and maximum discharge events. On the dry Argentine side of the range, reductions in erosion rates are still large, exceeding 70% for the high, glaciated Río Mendoza and Río Tunuyán catchments. On the wetter Chilean side, the Río Aconcagua and Río Colorado catchments were predicted to have modest decreases in erosion rates of < 15% relative to the baseline period. Erosion rates increased in the unglaciated Río Choapa catchment and also in the Río Tinguiririca catchment, where mean annual precipitation is highest.

4. Discussion

4.1. Changing Streamflow Regimes and Longitudinal Contrasts across the High Andes

A variety of different hydrologic modeling approaches have been used to model streamflow in the high Andes, including the Water Evaluation and Planning (WEAP) (Vicuña et al., 2011), Variable Infiltration Capacity (VIC) (Bozkurt *et al* 2018), and the TOPKAPI-ETH version of the TOPographic Kinematic APproximation and Integration (TOPKAPI) models (Ayala et al., 2020, Ragettli et al., 2016). While these modeling frameworks all have varying degrees of complexity, an advantage of HBV is the relative ease of adaptation for use in modeling multiple catchments. The static nature of the assumptions used in this study mean that the framework is not suitable for modeling catchment behavior on a continuum through time, but rather as an investigation of potential endmember responses to future change. Use of weather generator-based precipitation and temperature inputs scaled by elevation also mean that some real-world differences in weather patterns across individual catchments, such as storm events that may only reach upper or lower elevations, are necessarily simplified.

Despite differences across modeling frameworks, streamflow results from this study show broad similarities with prior work. Importantly, results from this study expand upon prior works by extending an analysis to additional catchments, including on the Argentine side of the Andes. In a study of four different basins on the Chilean side of the Andes stretching from 33 to 38° S, Bozkurt et al. (2018) predicted reductions in runoff of 40% by the end of the twenty-first century under the IPCC representative concentration pathway (RCP) 8.5 "business-as-usual" emissions scenario. Similarly, in a study of the Río Juncal catchment in Central Chile, a tributary of the Río Aconcagua, Ragettli et al. (2016) predicted that annual runoff would decrease by between 40% (RCP 4.5) and 60% (RCP 8.5) by the end of the twenty-first century. For the Chilean catchments, study results suggest that annual streamflow will decline by 36-52% under the drier and warmer scenario, most akin to RCP 8.5 "business-as-usual" assumptions (Table 2). The similarity of predictions in this study to prior works confirms that streamflow reductions in the Andes will be significant and exceed forecast reductions in precipitation (Bozkurt et al., 2018; Ragettli et al., 2016; Vicuña et al., 2011). Results from this study further show that declines in streamflow may be even larger on the Argentine side of the range (Table 2), indicating that different mitigation and adaptation strategies may need to be employed for catchments draining either side of the Andes.

For the glaciated catchments, future anticipated streamflow reductions are exacerbated by shrinking glacier mass (Ragettli et al., 2016). In addition, enhanced evapotranspiration under the warming scenarios likely amplifies future streamflow response (Vicuña et al., 2011). Finally, with less annual precipitation, a greater fraction of incoming precipitation may simply replenish groundwater stores that are likely to become increasingly depleted (Thomas & Famiglietti, 2019).

Surface water losses in the future may mean that the groundwater system will become an even more important source of freshwater in these high mountain catchments (Somers et al., 2019). While some efforts have been made to analyze the groundwater contribution to streamflow in the Argentine high Andes (e.g., Crespo et al., 2020), this may become an even more critical need in the coming decades.

Prior studies also predict an earlier arrival of peak runoff volume by weeks to months (Bozkurt et al., 2018, Ragettli et al., 2016), though results from this study show meaningful differences between the Chilean and Argentine catchments. While the average center of volume is predicted to arrive over a month earlier for the Argentine catchments under the drier and warmer scenario and warmer scenario, this shift was nearly two months earlier for the Chilean catchments (Figure 5, Table S7). The earlier center of volume timing is linked with the upwards retreat of the mean elevation of the JJAS 0°C isotherm (Figure 6). With a higher 0°C isotherm, an increased fraction of precipitation falls as rain rather than being stored as snow at higher elevations and precipitation that does fall as snow melts earlier in the season (Vicuña et al., 2011). In Chile, where most of the annual precipitation falls in winter (Masiokas et al., 2006), this effect is magnified relative to the Argentine catchments. The periodic occurrence of intense, high magnitude winter precipitation events in Chile (Viale & Norte, 2009) further contributes to increased variability in high flows as more of these events are anticipated to occur as rain.

4.2. Erosion Rates and Sediment Transport Implications

Erosion rates calculated for the baseline period are in general agreement with previously published erosion rates for the region using both river gauge data and ^{10}Be (Val et al., 2018, Carretier et al., 2013). With the exception of the Río Choapa, the catchment with the lowest observed erosion rates, erosion rate estimates from prior studies using gauge data are within error of the range of estimates produced using both observed and simulated streamflow values in this study (Figure 7, Table S8). Minimal sediment transport from April through October (Figure 3), excluding the high precipitation Río Tinguiririca catchment, is also consistent with previous work investigating sediment fluxes in a high Andean basin (Mao & Carrillo, 2017).

Currently, sediment fluxes in high Andean basins are tied principally to snow and glacier melt. Snowmelt is the dominant source of sediment transfer as temperatures warm through the spring, with glaciers taking on a gradually more important role as air temperatures reach their zenith in the summer (Mao & Carrillo, 2017). With both of these sources expected to decline in the future, researchers predict that both proglacial sources of sediment and hillslope sources delivering sediment via snowmelt will become increasingly disconnected from the fluvial system (Carrillo & Mao, 2020). Under the drier and warmer scenario modeled here, a retreating JJAS 0°C isotherm removes approximately 19-36% of each catchment area from a region of snow accumulation. With only intense rain events available to deliver sediment to a larger percentage of the stream channel, Carrillo & Mao (2020) predict that future sediment fluxes will become increasingly transport limited. In high elevation areas where vegetation is already sparse or nonexistent, increased aridity may also result in the downslope migration of stream channel heads and decreased drainage density, further disconnecting sediment supply from the fluvial system (Tucker & Bras, 1998). Predicted decreases in streamflow and stream power (Figure 5a, Table 2) further suggest that within the fluvial system, the potential for geomorphic work and channel incision could be reduced as the climate becomes more arid (Molnar et al., 2006).

If the high Andes do shift towards an increasingly transport limited environment, future sediment flux in this region could look very different than other higher altitude areas like the Alps or Tibetan Plateau or colder regions like the Arctic, where some studies predict net increases in sediment flux

(Li, D., et al., 2020; Costa et al., 2018; Kokelj et al., 2013; Lewis & Lamoureux, 2010; Syvitski et al., 2002). In these regions, increases in sediment flux are often linked with increases in air temperature, forcing increased melt from glaciers, snow, or permafrost and leading to increases in meltwater driven streamflow (Li, D., et al., 2020; Costa et al., 2018). In one catchment in the Alps, however, warming temperatures are predicted to lead to a decrease in landslide incidence originating from frost weathering (Hirschberg et al., 2021). The most important factor for the high Andes may be that they are possibly already past "peak water," so that further warming is not expected to yield greater runoff contributions from glaciers and streamflow is broadly expected to decline (Bozkurt et al., 2018; Ragettli et al., 2016).

A word of caution, of course, is that this analysis does not explicitly consider how hillslope processes might alter sediment supply dynamics in the future. Alterations in these dynamics could propagate into changes in the and *a* and *b* terms of the sediment rating curves (Yang et al., 2007; Asselman, 1999). For this reason, the results presented herein are more appropriately considered as floors on future sediment flux (Lewis & Lamoureux, 2010). While snowmelt is currently believed to be a key link between hillslope sediment sources and stream channels (Carrillo & Mao, 2020), a greater percentage of high precipitation events occurring as rain on exposed slopes could lead to rapid sediment mobilization (Iida et al., 2012). This effect could be pronounced in the Chilean high Andes, even if total annual precipitation is reduced, due to especially intense winter precipitation events (Viale & Norte, 2009). In addition, the average slope angle of the regions where JJAS snow cover may disappear exceeds 25° for most catchments, potentially placing these areas at a high risk of landslide incidence. While landslides are currently more likely to occur during summer storms in the high Andes (Sepúlveda et al., 2015; Morieras, 2005), a higher 0°C isotherm could make landsliding a greater risk during a longer portion of the year. Change in permafrost coverage could also influence both hillslope and streamflow dynamics, and prior studies indicate that conditions are favorable for the presence of permafrost at upper elevations in the high Andes, especially above 4000 m (Pereira et al., 2021; Bodin et al., 2010). Warming could subject these upslope regions to permafrost melt and consequent slope instability (Baldis & Liaudat, 2019). Figure 8 summarizes many of these possible changes. Quantification of how they may alter sediment supply dynamics in the future warrants further investigation.

In contrast to the two scenarios featuring reductions in precipitation, the warmer scenario shows that rising temperatures alone could produce highly variable future changes to sediment flux, even without explicitly accounting for changes in hillslope supply dynamics. This is especially true for Chile, where the median modeled erosion rates are predicted to increase for a subset of catchments. Increased sediment flux magnitude and variability for Chilean catchments are driven by an increase in the magnitude of outlier, high flow events (Figure 5), such as those associated with intense winter storms originating from the Pacific (Viale & Norte, 2009). In the absence of warming, the impacts of these large winter events, though significant, are nonetheless buffered by precipitation falling as snow at upper elevations, where total precipitation generally increases due to orographic effects. Conversion of some fraction of this high elevation precipitation to rain could contribute to more wintertime flooding in the Chilean catchments (Vicuña et al., 2013). Even if total annual streamflow decreases, the magnitude of these outlier events can accomplish substantial geomorphic work and mobilize significant volumes of sediment (Molnar et al., 2006, Leopold et al., 1964). A greater frequency of winter precipitation falling as rain instead of snow could also increase the frequency of high flow events, since snow is no longer stored to melt out gradually in the spring. Because high rainfall events are associated with regional landslide incidence (Sepúlveda et al., 2015; Morieras, 2005), this is a potential geohazard risk warranting increased study. These outlier events do not appear to have the same impact on the Argentine catchments, where spillover from storm events originating from the west often does not reach the lowlands and is largely concentrated in uninhabited upslope areas (Masiokas et al., 2006). However, even restricted to higher elevations, these events could still lead to short duration, high magnitude streamflow events and may be underestimated in the models. Changes in hillslope processes, such as permafrost melt, could enhance any of these outcomes and should be a focus of future research efforts in the region.

5. Conclusion

This study investigated endmember predictions of streamflow and fluvial sediment flux to future changes in air temperature and precipitation for eight catchments in the high Andes of Argentina and Chile. Considering only reductions in precipitation or only increases in air temperature yielded different catchment responses. Future declines in precipitation produced corresponding decreases in streamflow and sediment flux, suggesting that sediment mobilization could become increasingly transport limited, in contrast to other high mountain regions around the world. Considering only warming yielded differing responses in Argentina and Chile. Future warming conditions are expected to produce earlier streamflow arrival, and to even produce larger maximum discharge events in Chilean catchments. These characteristics bode for greater future variability in sediment flux in Chile. Importantly, changes in precipitation and temperature considered in this study could also alter sediment supply dynamics in ways not explicitly modeled through the rating curve method employed herein. Supply increases relating to landslide incidence and permafrost melt are two areas in particular warranting future study. Nonetheless, these results indicate that the different hydroclimatic characteristics on either side of the Andes, such as the prevalence of strong winter precipitation events originating from the Pacific, can lead to very different changes in fluvial transport capacity under different climate scenarios. As such, different mitigation strategies may need to be employed on either side of the range to protect water resources and prepare for a changing future.

Acknowledgements

This work was supported by the National Science Foundation under Grant DGE-1449617 and by Syracuse University's Education Model Program on Water-Energy Research (EMPOWER) and Research Excellence Doctoral Funding (REDF) programs.

Figures

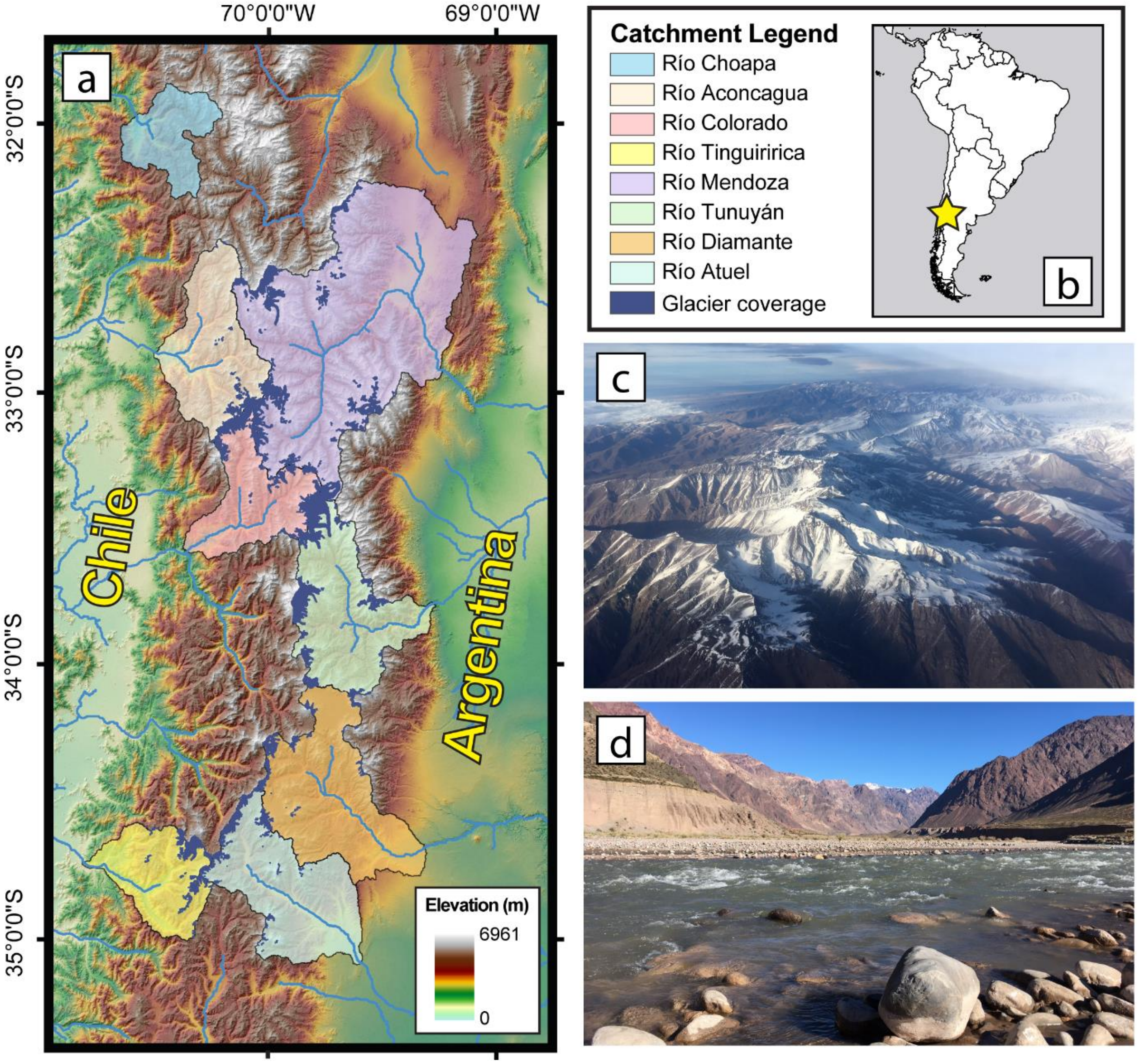

Figure 1: *(a)* Map of the study area in the high Andes of Chile and Argentina with shaded outlines of all eight catchments. The extent of glacier coverage within the catchments is shown in dark blue. Glacier coverage is from the Randolph Glacier Inventory (RGI Consortium, 2017). *(b)* Location of the study area within South America. *(c)* Aerial view of the study area looking south. *(d)* View of the Río Mendoza in the Andes Mountains between the towns of Uspallata and Polvaderas.

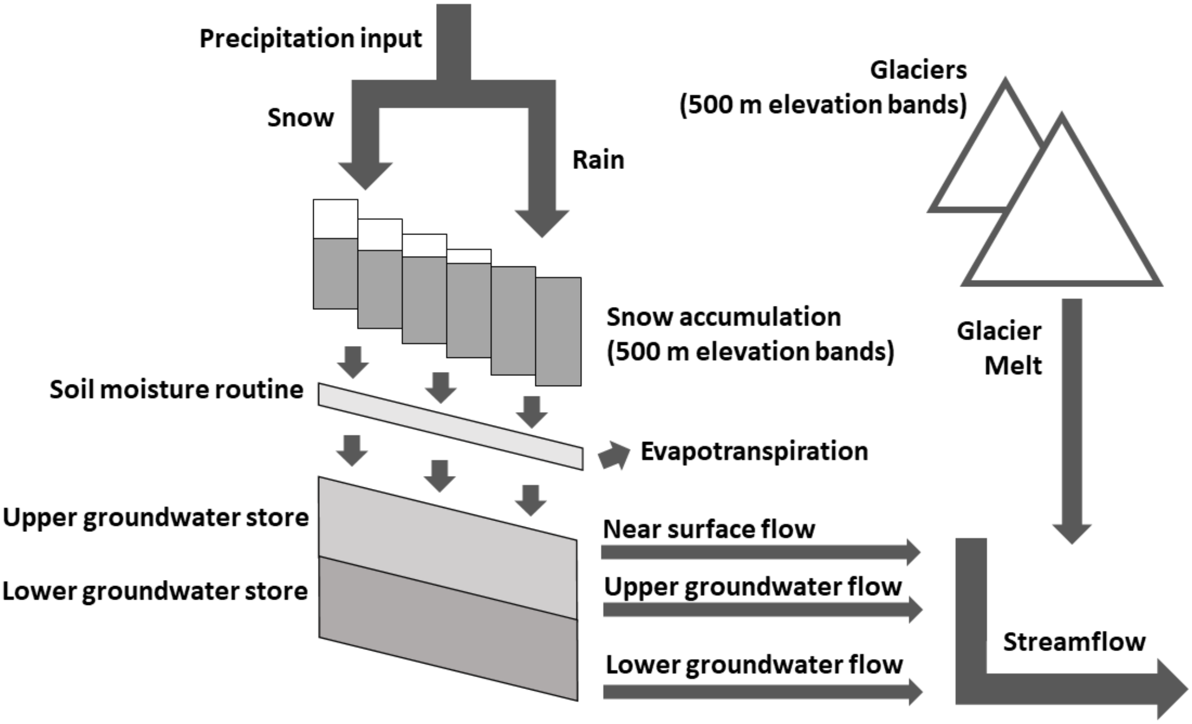

Figure 2. Simplified conceptual overview of the HBV model implementation used in this study, based on Seibert & Vis (2012).

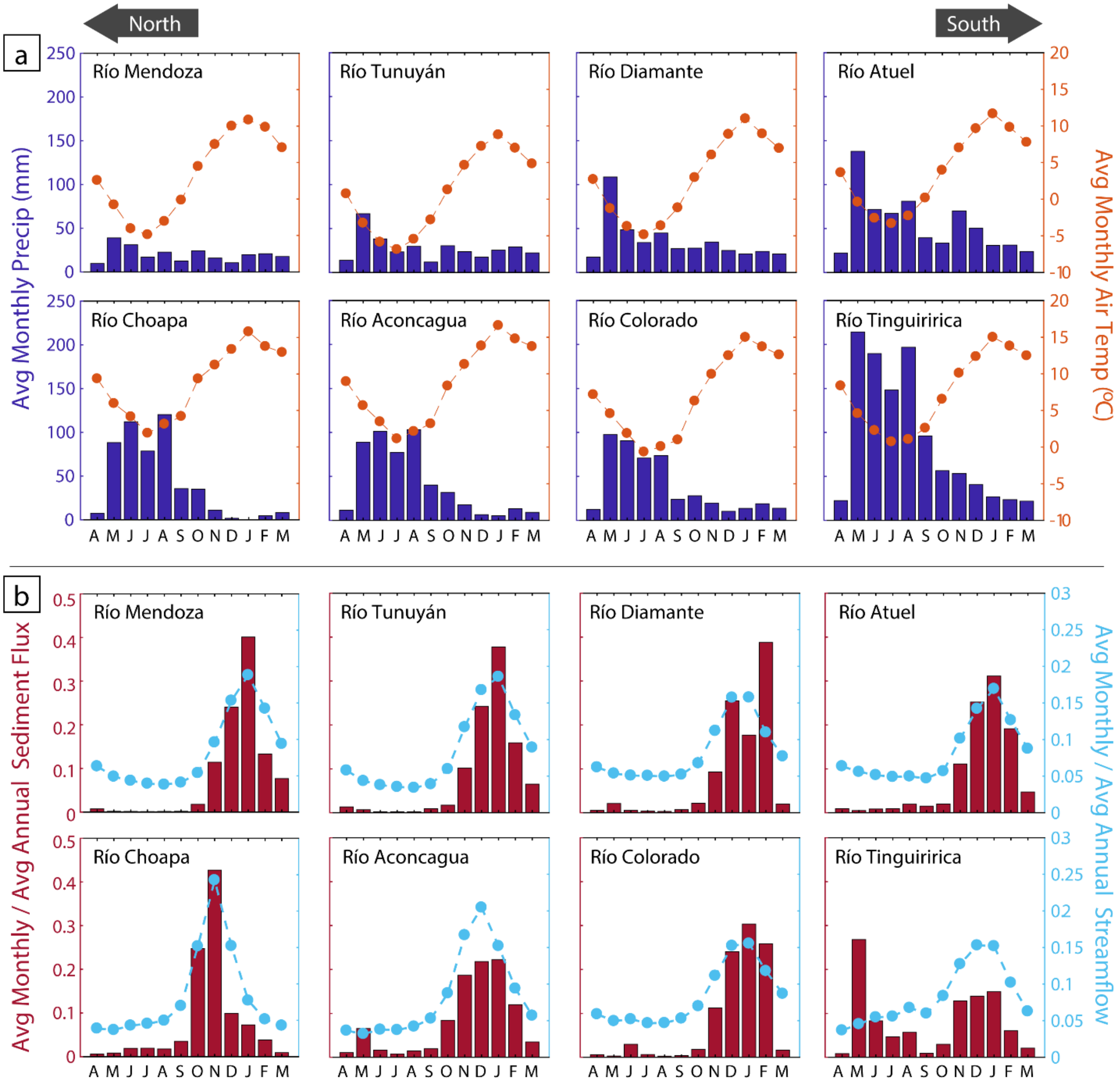

Figure 3: *(a)* Average monthly baseline period (water year 2005-2014) precipitation and temperature data for each watershed. *(b)* Average monthly baseline period streamflow and sediment flux data for each watershed, shown as the fraction of total average annual streamflow and sediment flux for each watershed for ease of comparison. Note that sediment flux data for the Río Colorado used in this study are only available through 2010 (Table S1). For *(a)* and *(b)*,

Argentine catchments appear on the first row, followed by Chilean catchments on the second row.

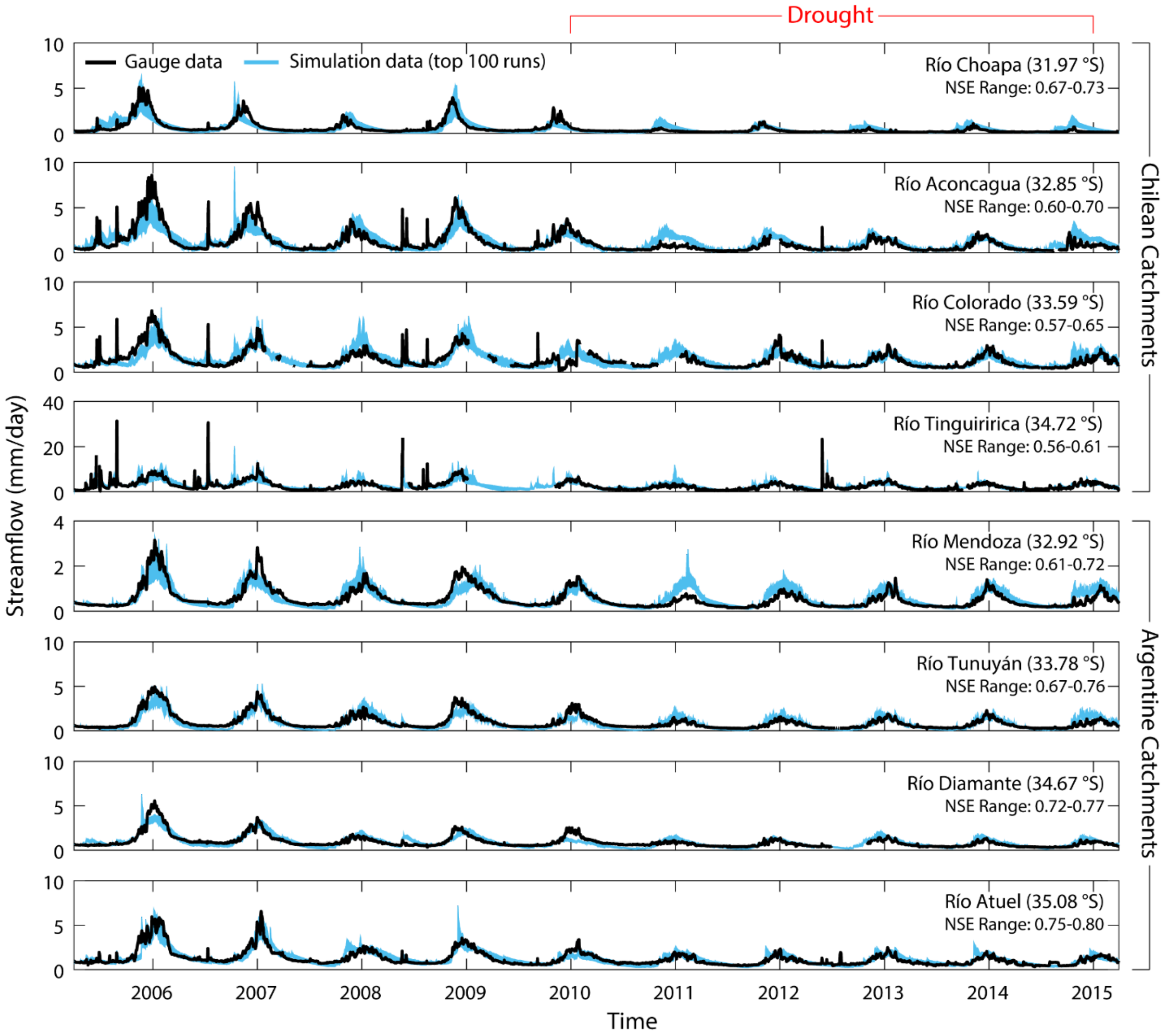

Figure 4: Streamflow (mm/day) from gauge data and all top 100 simulations for water year 2005-2014 baseline period. X-axis ticks denote start of each listed calendar year. Note differences in y-axis scale among catchments and reductions in peak flow during the 2010-2015 “mega drought.” Latitude of each catchment listed parenthetically. Nash-Sutcliffe Efficiency (NSE) ranges for the top 100 parameter sets are listed for each catchment.

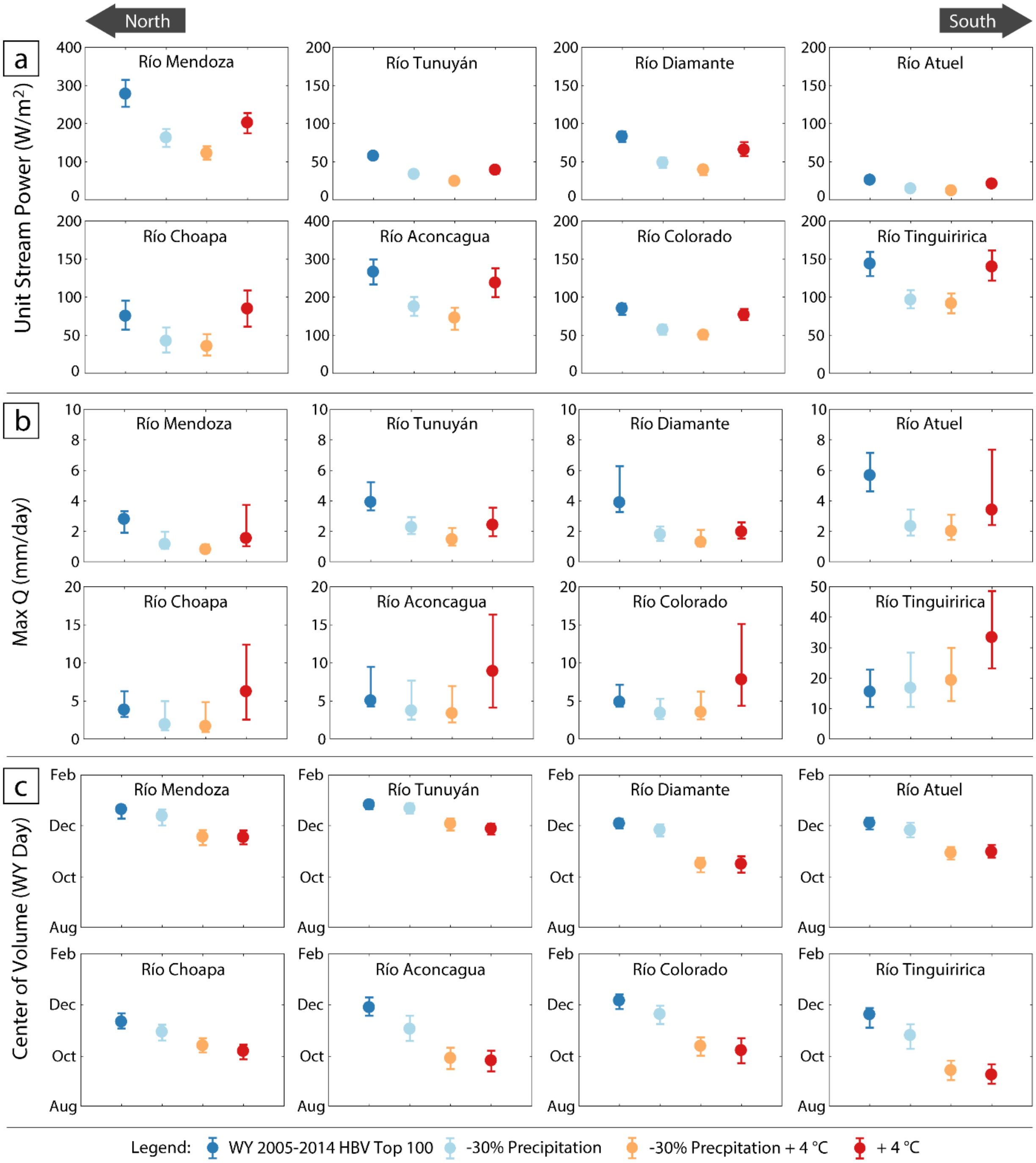

Figure 5: *(a)* Unit stream power, *(b)* maximum stream discharge, and *(c)* center of volume results for top baseline period model runs (n = 100) and range of all results from 5th to 95th percentiles for future climate scenarios (n = 4500). For each statistic, Argentine catchments appear on the first row, followed by Chilean catchments on the second row. In the results for

maximum stream discharge events, note different y-axis limits for the Argentine and Chilean catchments and the even larger y-axis limits for the Río Tinguiririca as compared to all other catchments. Also note different y-axis limits for the Río Mendoza and Río Aconcagua in the unit stream power results.

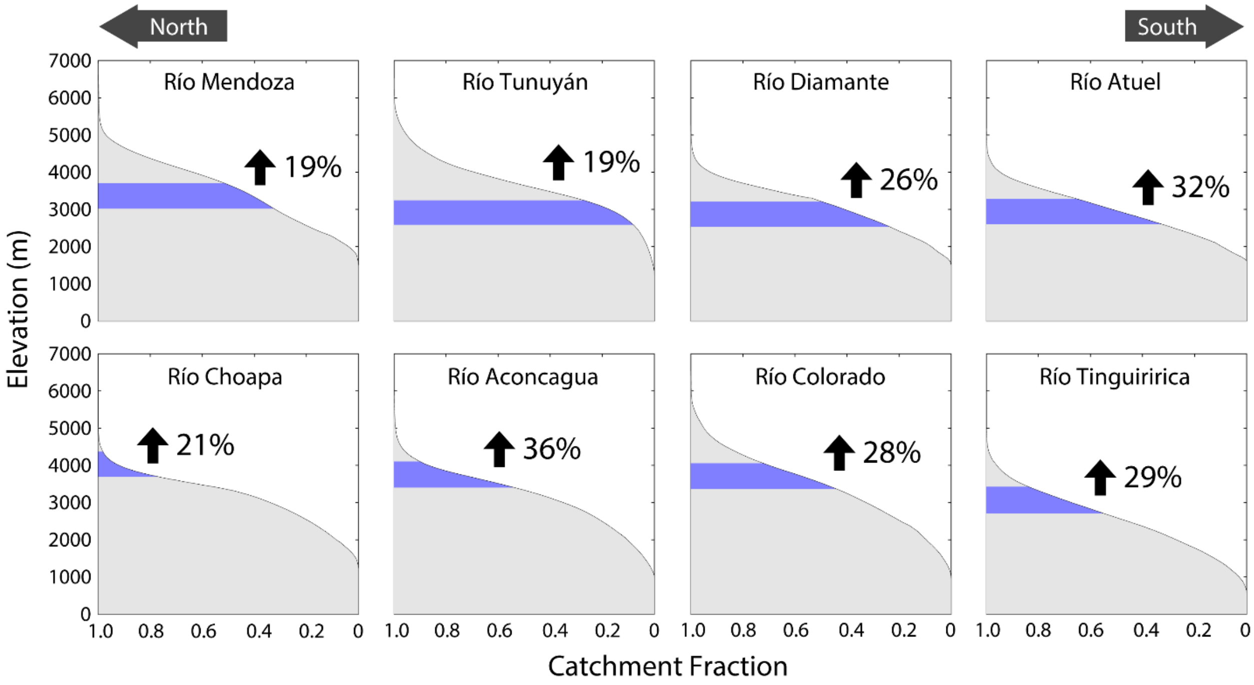

Figure 6: Catchment hypsometry and change in mean 0°C isotherm for each watershed for the June, July, August and September (JJAS) time period from the baseline period to plus 4°C warming scenarios (Scenarios 2 and 3). Argentine catchments appear on the first row, followed by Chilean catchments on the second row. Catchment hypsometry is shown in gray. The regions newly exposed to temperatures above freezing during this time period, on average, are shown in blue. The bottom of the blue shaded region represents the mean elevation of the JJAS 0°C isotherm during the baseline period and the top of the blue shaded region represents the mean elevation of the JJAS 0°C isotherm under the warming scenarios. The total percentage of the catchment area exposed to temperatures above freezing relative to the baseline period is also displayed for each catchment.

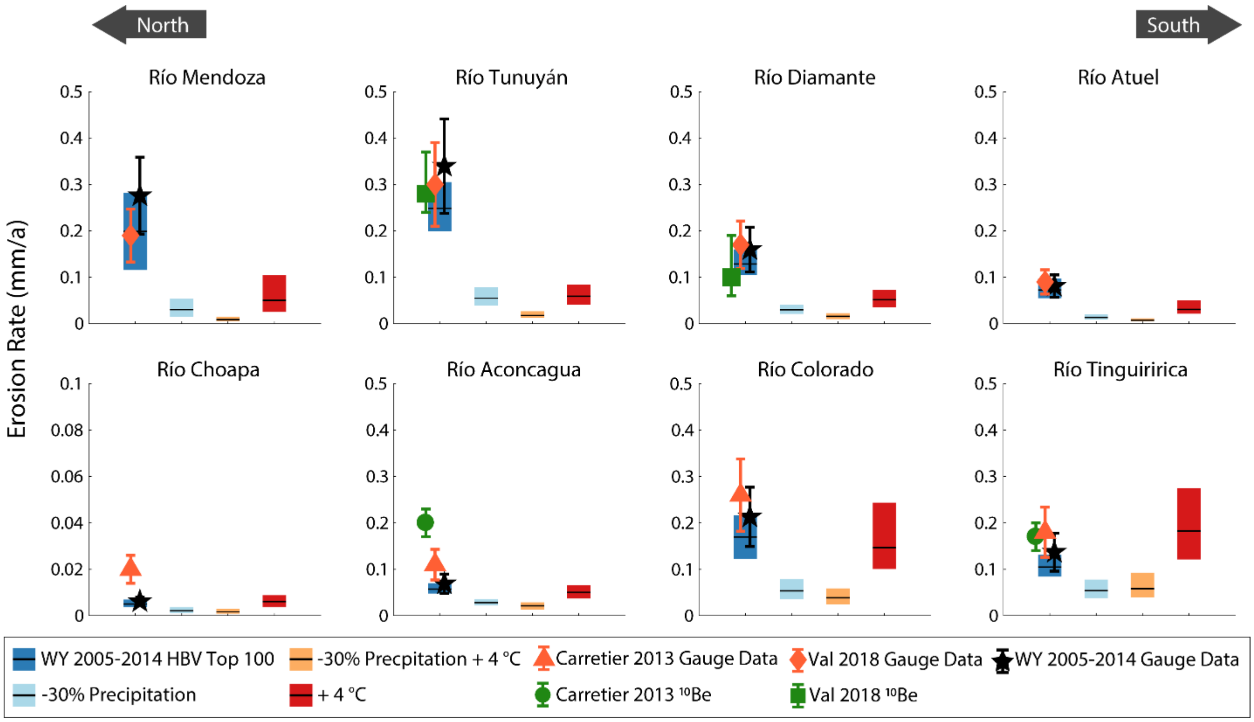

Figure 7: Simulated erosion rates for top baseline period model runs (n = 100) and future climate scenarios and range of all results from 5th to 95th percentiles for future climate scenarios (n = 4500). Argentine catchments appear on the first row, followed by Chilean catchments on the second row. Black lines across vertical bars represent median erosion rates for each scenario depicted. Erosion rates calculated using observed stream gauge data from this and other studies along with ^{10}Be results from other studies (Carretier et al., 2013; Val et al., 2018) are shown for comparison to the baseline period scenarios. Note different y-axis limits for the Río Choapa, the northernmost catchment in this study, which also has the lowest observed erosion rates.

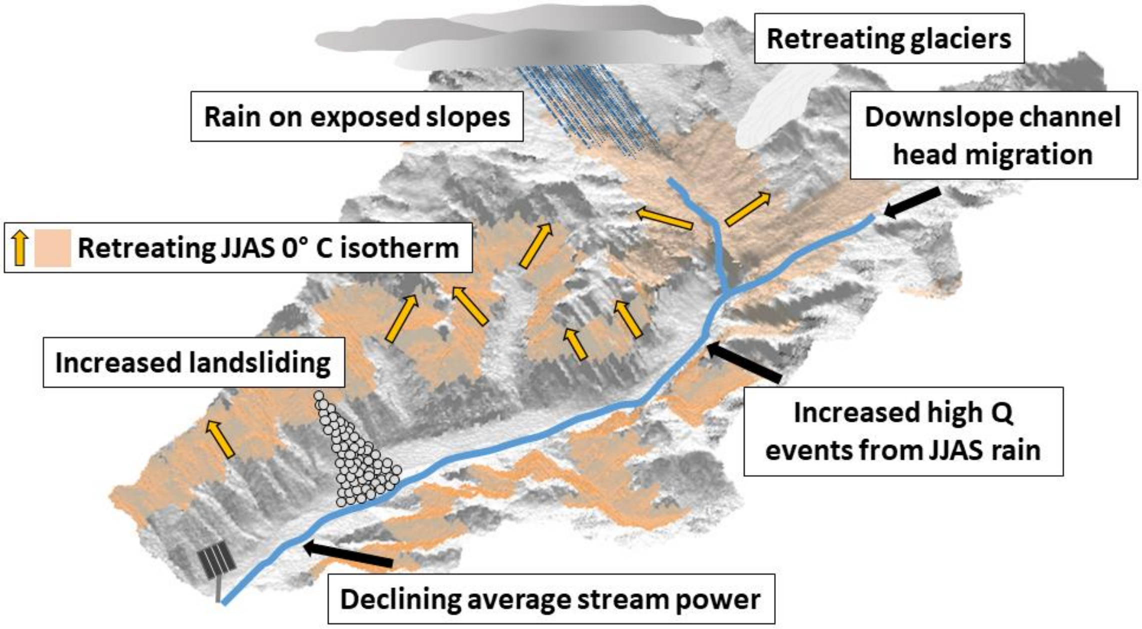

Figure 8: Conceptual diagram showing landscape changes under + 4°C of warming. A retreating JJAS 0°C isotherm (orange arrows) leads to an increase in precipitation events occurring as rain rather than snow on slopes without snow or ice cover. Large wintertime precipitation events on exposed slopes may lead to an increased incidence of landsliding. Reductions in glacier coverage and net annual precipitation are linked with declining stream power and downslope channel head migration.

Tables

Table 1. Stream gauge stations and associated watershed characteristics all eight catchments in this study. Latitude and longitude shown for location of gauge station at each catchment outlet. Total catchment glacier area from the Randolph Glacier Inventory (RGI Consortium, 2017). Mean annual precipitation for the water year 2005-2014 baseline period, averaged across each catchment, from the Climate Hazards Group InfraRed Precipitation with Stations (CHIRPS) dataset (Funk et al., 2015). Mean annual temperature for the Chilean catchments from the CR2MET database via the Catchment Attributes and MEteorology for Large-sample Studies dataset in Chile (CAMELS_CL) database (Alvarez-Garreton et al., 2018). Mean annual temperature for the Argentine catchments from individual gauge stations (BDHI, 2020) and adjusted to the mean catchment elevation using lapse rate of 0.6°C per 100 m.

Gauge Station	**Gauge station number**	**Lat (°S)**	**Lon (°W)**	**Gauge station elevation (m)**	**Catchment mean elevation (m)**	**Catchment max elevation (m)**	**Catchment area (km^2)**	**Glacier cover (%)**	**Mean annual precip (mm/a)**	**Mean annual temp (°C)**
Chile										
Río Choapa at Cuncumen	4703002	31.9667	70.5944	1204	3142	5038	1132	0.0	503	8.73
Río Aconcagua at Chacabuquito	5410002	32.8503	70.5094	939	3178	5924	2113	2.26	506	8.55
Río Colorado prior to confluence with Río Maipo	5707002	33.5875	70.3669	962	3419	6550	1663	9.12	473	6.96
Río Tinguiririca at Bajo Los Briones	6028001	34.7186	70.8267	573	2550	4962	1438	5.08	1090	7.45
Argentina										
Río Mendoza – at Guido	1413	32.9153	69.2378	1419	3528	6961	7155	4.24	240	3.23
Río Tunuyán – at Uco Valley	1419	33.7765	69.2725	1225	3649	6532	2458	9.83	332	0.81
Rio Diamante – at La Jaula	1423	34.6685	69.3163	1468	3094	5265	2832	2.33	434	2.70
Rio Atuel – at El Sosneado	1428	35.0839	69.6031	1602	2948	5176	2364	3.01	659	3.72

Table 2. Mean annual total runoff (Q) for each catchment for observed and top 100 simulated baseline period time series and all future climate scenarios. Drier scenario = -30% precipitation. Drier and warmer scenario = -30% precipitation + 4°C. Warmer scenario = + 4°C. Minimum and maximum Kling-Gupta Efficiency (KGE) and Nash-Sutcliffe Efficiency (NSE) values for top 100 models are also shown for each catchment. Percent changes for future climate scenarios are based on a comparison of mean simulated values for the baseline period to the mean of the future scenario. Both area-normalized and total volume of glacier contribution to baseline period streamflow are also shown.

Catchment	**Mean annual observed runoff (mm/a)**	**Mean annual model runoff & min, max (mm/a)**	**Mean annual glacier contribution & min, max (mm/a)**	**Mean annual glacier contribution (m^3/a)**	**Model KGE Range**	**Model NSE Range**	**Drier scenario mean annual Q (mm/a) & % change**	**Drier & warmer scenario mean annual Q (mm/a) & % change**	**Warmer scenario mean annual Q (mm/a) & % change**
Chile									
Choapa	196	178 (137, 228)	0	0	0.56, 0.84	0.67, 0.73	102 (-43%)	86 (-52%)	202 (+13%)
Aconcagua	410	411 (358, 458)	72 (67, 77)	152 x 10^6	0.58, 0.75	0.60, 0.70	268 (-35%)	222 (-46%)	364 (-11%)
Colorado	492	488 (442, 528)	39 (26, 52)	65 x 10^6	0.64, 0.80	0.57, 0.65	329 (-33%)	289 (-41%)	442 (-9%)
Tinguiririca	952	954 (852, 1064)	37 (30, 44)	53 x 10^6	0.60, 0.76	0.56, 0.61	645 (-33%)	612 (-36%)	937 (-2%)
Argentina									
Mendoza	201	205 (181, 223)	20 (4, 36)	140 x 10^6	0.65, 0.84	0.61, 0.72	121 (-41%)	91 (-56%)	149 (-27%)
Tunuyán	340	297 (276, 316)	43 (33, 54)	106 x 10^6	0.74, 0.85	0.67, 0.76	174 (-41%)	127 (-57%)	201 (-32%)
Diamante	336	332 (296, 349)	21 (16, 26)	60 x 10^6	0.76, 0.87	0.72, 0.77	189 (-41%)	152 (-53%)	256 (-20%)
Atuel	451	450 (404, 503)	11 (5, 16)	25 x 10^6	0.75, 0.89	0.75, 0.80	250 (-44%)	203 (-55%)	362 (-19%)

Supplementary Information

S.1. Sediment Data and Sediment Rating Curves

Sediment data in Argentina and Chile are collected, maintained, and made publicly available by national government agencies. In Chile, these data are compiled by the Dirección General de Aguas de Chile (DGA, 2020). In Argentina, they are compiled by the Secretaría de Infraestructura y Política Hídrica de la Nación (BDHI, 2020). Sediment data in Chile are collected daily and reported as suspended sediment yield using US D-74 or US D-59 depth integrating samplers (Carretier et al., 2013). In Argentina, suspended sediment data are collected with US D-49 or US D-77 depth integrating samplers (SMRH, 2021). These data are reported as daily values, sorted by grain size, as either "caudal solido grueso" (coarse) or "caudal solido fino" (fine), with the boundary between the two defined as 62 μm. Collectively, these are some of the most robust sources of sediment data in the region, where sediment data is often scarce (Pepin et al., 2010), and these datasets have been used in several prior studies estimating sediment flux and erosion rates (e.g., Val et al., 2018; Carretier et al., 2013; Pepin et al., 2010). The length of each sediment record and number of individual observations from each gauge station are shown in Table S1. A 30% error is ascribed to all sediment flux estimates, keeping in practice with previous work in the region (Val et al., 2018; Carretier et al., 2013; Pepin et al., 2010). This error estimate is based on uncertainty inherent in the temporal gaps between individual data points and uncertainty associated with measuring sediment flux across an entire stream channel from discrete measurements (Carretier et al., 2013; Pepin et al., 2010). As prior researchers have noted, a 30% error is higher than the 7-10% error often associated with depth integrating samplers (Carretier et al., 2013).

As stated in the Methods, sediment data were paired with observed streamflow data for each catchment to create sediment rating curves for each catchment in the form:

$$Q_s = aQ^b$$

where Q_s is sediment flux, Q is streamflow, and a and b are rating curve parameters (Gao, 2008). The a and b parameters were initially determined using MATLAB by applying a linear regression to log transformed sediment and streamflow data (Gao, 2008). The fit of each of these rating curve equations was assessed by comparing the total sediment flux predicted by the rating curves for periods of observed sediment data to the total observed sediment flux. For the Argentine catchments, predicted and observed sediment fluxes differed by no more than 32%, and these fits were deemed acceptable. For the Chilean catchments, despite having considerably more sediment data, initial rating curves underestimated observed sediment fluxes by more than 35%. Underestimation is common in sediment flux estimates from rating curves as a result of the log transformations necessary to generate the rating curve equation and a number of mechanisms exist to correct for this potential bias (Gao, 2008; Runkel *et al* 2004; Ferguson, 1986). For this study, the United States Geological Survey's LOAD ESTimator (LOADEST) Fortran program was used to create revised rating curves for the Chilean catchments, as it includes built-in mechanisms for correcting for transformation bias (Runkel *et al* 2004). LOADEST has been used in a number of prior studies for sediment load estimation (e.g., Li, L., et al., 2020, Lewis & Lamoureux, 2010).

As a practical matter, the bias-corrected LOADEST rating curves resulted in a multiplicative adjustment to the non-corrected rating curves, increasing the value of the a term in each rating curve equation. Final rating curves generated by LOADEST for the Chilean catchments predicted total sediment fluxes within 5% of observed fluxes for the Río Aconcagua, Río Colorado, and Río Tinguiricia and within 33% for the Río Choapa. Final rating curves for all catchments are shown in Figure S1.

S.2. HBV Model

S.2.1. HBV Model Conceptual Overview

The HBV model implementation used in this study is a semi-distributed conceptual rainfall-runoff model (Seibert & Vis 2012, Figure 2) with 15 parameters (Table S2). The model uses a single average daily value for precipitation and temperature for each catchment from a single elevation. Because precipitation data for Chile and Argentina and temperature data for Chile were obtained as averages across each catchment, the mean catchment elevation was used as the starting point for selecting the elevation of these observations. To account for uncertainty in the precipitation and temperature averages, 500 m window was set around the catchment mean elevation when selecting the 2000 parameter sets through Latin hypercube sampling (described in the Methods and in Section S.2.2.). Because temperature data for Argentina were obtained from gauge stations with known elevations (Table S3), those elevations were used in all simulation runs. Table S4 lists the range of parameter values used for each catchment in the top 100 model runs plus the range of elevation values used for temperature and precipitation inputs in the top 100 runs.

In the model, precipitation and temperature inputs were partitioned across a series of 500 m vertical elevation bands within each catchment based on the fractional area of each elevation band. Precipitation and temperature inputs were also scaled vertically across elevation bands using lapse rates of 10% per 100 m and 0.6 °C per 100 m, respectively. Precipitation fell as snow in a given elevation band when observed temperatures, adjusted by lapse rate, were below the calibrated threshold temperature. The rate of snowmelt was governed by a calibrated degree-day factor when temperatures rose above the calibrated temperature threshold (Tables S2, S4). For any given day, total snowmelt was equal to the degree-day factor multiplied by the difference between the observed daily temperature and the calibrated temperature threshold. Melted snow could also refreeze at a rate governed by a refreezing coefficient when temperatures dropped back below the temperature threshold. Snowmelt entered a soil moisture store when the amount of meltwater in the snowpack crossed the snowpack water holding capacity. In elevation bands with snow present, this meltwater includes rainfall. Where no snow is present, rainfall is routed directly to the soil moisture store.

A percentage of the rain and snowmelt inputs to the soil moisture store were routed to groundwater stores, based on how much water was in the soil moisture store and its total water holding capacity. Water in the soil moisture store could evaporate up to the potential evapotranspiration limit. Monthly averages of potential evapotranspiration were used in the models, with daily values linearly interpolated from these averages. Water moving into the groundwater stores first moved into an upper groundwater store. Water moved from the upper groundwater store to a lower groundwater store at a fixed rate of infiltration. Water moved out of the groundwater stores and into streamflow through three different flow paths: a near surface flowpath, an upper groundwater flowpath, and a lower groundwater flowpath. Water moving via the near surface flow path occurred when water in the upper groundwater store exceeded a calibrated threshold. Calibrated coefficients for each flow path from the groundwater stores governed the rate of flow from these stores. Initial state variables are unique to each catchment and determined based on a warm-up period, taking into account weather inputs and catchment parameters. More detailed information on the HBV implementation used in this study, including governing equations, can be found in Seibert & Vis (2012) and more generally in Bergström (1992).

S.2.2. HBV Parameter Calibration

An initial set of parameters were selected for each catchment using a Genetic Algorithm and Powell (GAP) optimization routine. These parameters were chosen from the ranges specified in Table S2, which are default ranges set within the HBV implementation used in this study. Fifty different parameter sets were randomly selected from within that range and recombined for 5,000 model runs. Following these 5,000 runs, another 1,000 model runs were performed using Powell's quadratically convergent method (Seibert & Vis, 2012). Model performance was evaluated using Nash-Sutcliffe Efficiency (NSE) as the objective function, calculated as:

$$NSE = 1 - \frac{\sum_{t=1}^{T}(Q_{s,t} - Q_{o,t})^2}{\sum_{t=1}^{T}(Q_{o,t} - \mu_o)^2}$$

where Q_s is simulated streamflow, Q_o is observed streamflow, and μ_o is the mean of observed streamflow (Nash & Sutcliffe, 1970).

The single set of parameters arrived at using the GAP optimization routine was then used as the basis for Latin hypercube sampling. As described in the Methods, 2000 parameter sets were generated from a range of +/- 30% applied to GAP routine optimized parameter values, as allowable within HBV parameter space. These parameter sets were then used to run simulations for the baseline period and evaluated against observed streamflow on the basis of NSE. The top 100 parameter sets, ranked by NSE, were selected for future simulation runs (Table S4). As also stated in the Methods, Kling-Gupta Efficiency (KGE) was calculated for model runs as a secondary metric of model fit as follows:

$$KGE = 1 - \sqrt{(r-1)^2 + (\alpha - 1)^2 + (\beta - 1)^2}$$

where r is the linear correlation coefficient between the observed values and the simulated values, α is the standard deviation of the simulated values divided by the standard deviation of the observed values, and β is the mean of the simulated values divided by the mean of the observed values (Gupta et al., 2009).

S.3. Baseline period Observed Versus Modeled Streamflow Results

Mean annual modeled and observed streamflow values for the baseline period were in reasonably close agreement in this study. Observed mean annual streamflow values for the baseline period fell within the range of mean annual streamflow values from the top 100 models for all catchments with the exception of the Río Tunuyán. At the Río Tunuyán, the catchment with the highest mean elevation (Table 1), the median average annual modeled streamflow underpredicted observed average annual streamflow by 43 mm (Table 2). The maximum observed daily stream discharge event for each catchment for the baseline period also fell within the range of maximum discharge events simulated in each of the top 100 models for seven out of the eight catchments. The one exception was the Río Tinguiririca, where the highest observed daily streamflow event was higher than all of the maximum daily streamflow events in each of the top 100 simulations (Table S5). As the southernmost catchment on the Chilean side of the Andes in this study, precipitation inputs to the Río Tinguiririca were higher than any other catchment (Table 1), and the median maximum streamflow event for the top 100 simulations for the Río Tinguiririca was still more than three times higher than the median maximum events for any other catchment (Table S5).

The modeled glacier contribution to streamflow was also comparable to prior work. In particular, the modeled annual glacier contribution to runoff for the Río Colorado catchment in this study was 26-52 mm for the baseline period. This result is within the range of the annual runoff contribution of 53.2 ± 12.2 mm per water year reported by Ayala et al. (2020) for the same watershed for the longer water year 1955-2016 time period in a study focusing on the larger Río Maipo basin.

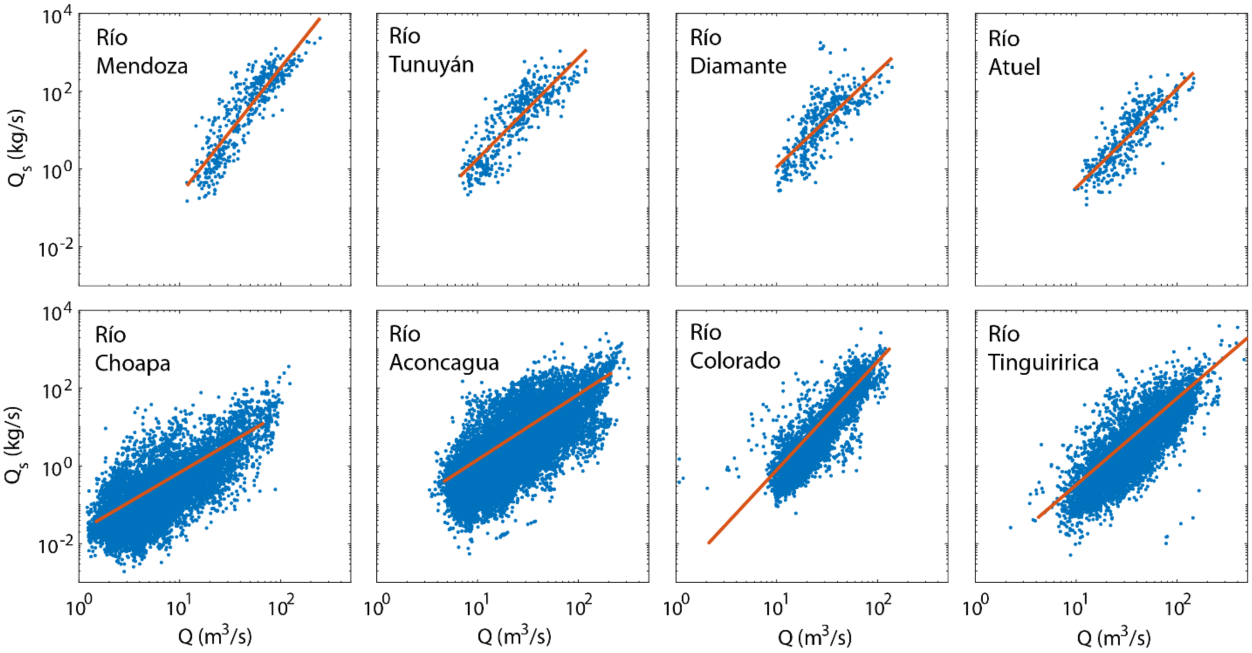

Figure S1. Final rating curves for all eight catchments (orange lines) and paired streamflow (Q) and sediment flux (Q_s) observations.

Table S1. Stream gauge sediment data years of observation and number of observations at each site.

River	Gauge Location	Gauge Number	Years Covered	Number of Observations
Choapa	Cuncumen	4703002	1986-2018	11249
Aconcagua	Chacabuquito	5410002	1966-2018	16724
Colorado	Prior to confluence with Río Maipo	5707002	1985-2010	3980
Tinguiririca	Bajo Los Briones	6028001	1989-2018	7354
Mendoza	Guido	1413	1999-2020	441
Tunuyán	Uco Valley	1419	1999-2020	439
Diamante	La Jaula	1423	1999-2020	432
Atuel	El Sosneado	1428	1999-2020	388

Table S2. HBV model parameters and ranges used for initial calibration. Parameter functions are as described in Seibert and Vis (2012). Note that two parameters, CFR and CWH, had fixed values in all model runs.

Parameter	**Function (units)**	**Minimum Limit**	**Maximum Limit**
Snow Routine			
TT	Threshold temperature (°C)	-2	0.5
CFMAX	Degree-day factor (mm/day)	0.5	4
SFCF	Snowfall correction factor (n/a)	0.5	0.9
CFR	Refreezing coefficient (n/a)	0.05	0.05
CWH	Snowpack water holding capacity (n/a)	0.1	0.1
Soil and Groundwater Routine			
FC	Soil moisture storage limit (mm)	100	550
LP	Soil moisture threshold for actual evapotranspiration equaling potential evapotranspiration (n/a)	0.3	1
BETA	Term partitioning rain/snowmelt contribution to groundwater store (n/a)	1	5
PERC	Maximum percolation to lower groundwater store (mm/day)	0	4
UZL	Threshold parameter for near-surface flow (mm)	0	70
K0	Recession coefficient for near-surface flow (1/day)	0.1	0.5
K1	Recession coefficient for upper groundwater store (1/day)	0.01	0.2
K2	Recession coefficient for lower groundwater store (1/day)	0.00005	0.1
MAXBAS	Length of routing routine weighting function (1/day)	1	2.5
CET	Potential evaporation correction factor (1/°C)	0	0.3

Table S3. Argentina gauge stations used for temperature data.

Catchment	Temperature Gauge Station	Gauge Number	Lat (°S)	Lon (°W)	Gauge elevation (m)
Río Mendoza	Mendoza - Uspallata	1491	32.5946	69.3401	1899
Río Tunuyán	Tunuyán - Uco Valley	1419	33.7765	69.2725	1225
Rio Diamante	Diamante - La Jaula	1423	34.6685	69.3163	1468
Rio Atuel	Malargüe - Dique	1476	35.5422	69.6421	1525

Table S4. Range of calibrated snow routine and soil routine parameters for top 100 HBV models for each catchment. Minimum and maximum values for each parameter for each catchment separated by commas. Range of elevations used for precipitation and temperature inputs also shown.

	Chilean Catchments				**Argentine Catchments**			
Parameter	*Choapa*	*Aconcagua*	*Colorado*	*Tinguiririca*	*Mendoza*	*Tunuyán*	*Diamante*	*Atuel*
TT	0.33, 0.50	0.26, 0.48	0.16, 0.29	-0.38, -0.21	0.30, 0.50	-0.65, -0.35	-1.3, -0.70	-1.2, -0.64
CFMAX	1.9, 3.4	1.1, 2.0	0.71, 1.2	1.9, 3.4	0.57, 1.0	0.80, 1.3	1.2, 2.0	0.83, 1.3
SFCF	0.65, 0.90	0.83, 0.90	0.83, 0.90	0.63, 0.90	0.83, 0.90	0.83, 0.90	0.79, 0.90	0.64, 0.90
FC	320, 550	360, 550	100, 140	100, 170	120, 220	390, 550	390, 550	390, 550
LP	0.52, 0.95	0.73, 1.0	0.70, 1.0	0.30, 0.44	0.73, 1.0	0.88, 1.0	0.73, 1.0	0.74, 1.0
BETA	3.3, 5.0	1.1, 2.1	1.0, 1.4	1.0, 1.3	1.0, 1,3	1.0, 1.3	1.0, 1.3	1.2, 2.2
PERC	1.9, 3.4	1.9, 3.6	1.2, 2.2	2.9, 4.0	0.45, 0.82	1.0, 1.8	3.3, 4.0	1.4, 2.6
UZL	44, 70	35, 64	36, 67	23, 43	28, 51	46, 70	51, 70	54, 70
K0	0.10, 0.18	0.27, 0.49	0.16, 0.30	0.27, 0.48	0.11, 0.20	0.21, 0.38	0.10, 0.13	0.10, 0.13
K1	0.019, 0.035	0.043, 0.079	0.049, 0.090	0.044, 0.082	0.016, 0.029	0.031, 0.056	0.010, 0.014	0.020, 0.037
K2	0.010, 0.019	0.020, 0.035	0.0095, 0.017	0.015, 0.026	0.0073, 0.013	0.017, 0.03	0.012, 0.022	0.0067, 0.012
MAXBAS	1.8, 2.5	1.8, 2.5	1.1, 2.1	1.5, 2.5	1.0, 1.3	1.0, 1.3	1.0, 1.3	1.0, 1.7
CET	0.075, 0.14	2x10^{-6}, 4x10^{-6}	0.088, 0.16	0.22, 0.30	2x10^{-7}, 4x10^{-7}	0.073, 0.13	0.13, 0.23	0.14, 0.25
Precip Elev (m)	2894, 3288	2932, 3198	3170, 3337	2303, 2583	3279, 3419	3400, 3507	2845, 3041	2699, 3041
Temp Elev (m)	2892, 3103	2900, 3115	3171, 3386	2301, 2680	1899	1225	1468	1525

Table S5. Observed and modeled maximum stream discharge (Q) events from each time series for the observed and modeled baseline period and for all future scenarios, normalized by watershed area. Drier scenario = -30% precipitation. Drier and warmer scenario = -30% precipitation + 4°C. Warmer scenario = + 4°C. For the simulated baseline period, the range of max Q events is from the top 100 parameter sets (n = 100). For future scenarios, the range of max Q events is from 5th and 95th percentiles of all 5000 simulations (n = 4500).

Catchment	**Baseline period observed max Q (mm)**	**Baseline period model median max Q and range (mm)**	**Drier scenario median max Q and range (mm)**	**Drier and warmer scenario median max Q and range (mm)**	**Drier scenario median max Q and range (mm)**
Chile					
Choapa	5.10	3.82 (2.92, 6.28)	1.92 (1.15, 4.98)	1.68 (0.93, 4.83)	6.23 (2.57, 12.40)
Aconcagua	8.59	5.03 (4.29, 9.49)	3.71 (2.56, 7.68)	3.36 (2.19, 6.97)	8.89 (4.14, 16.35)
Colorado	6.81	4.87 (4.25, 7.13)	3.43 (2.62, 5.31)	3.51 (2.58, 6.24)	7.79 (4.37, 15.12)
Tinguiririca	31.30	15.48 (10.56, 22.79)	16.72 (10.54, 28.35)	19.28 (12.50, 29.97)	33.34 (23.20, 48.56)
Argentina					
Mendoza	3.15	2.79 (1.92, 3.32)	1.15 (0.86, 1.98)	0.81 (0.58, 1.15)	1.54 (1.01, 3.73)
Tunuyán	4.96	3.91 (3.38, 5.22)	2.26 (1.83, 2.93)	1.46 (1.07, 2.23)	2.41 (1.69, 3.55)
Diamante	5.55	3.88 (3.26, 6.28)	1.79 (1.38, 2.32)	1.29 (1.01, 2.10)	1.97 (1.53, 2.58)
Atuel	6.56	5.67 (4.65, 7.15)	2.33 (1.73, 3.43)	2.00 (1.45, 3.09)	3.40 (2.42, 7.36)

Table S6. Average unit stream power for each time series for the modeled baseline period and for all future scenarios. Drier scenario = -30% precipitation. Drier and warmer scenario = -30% precipitation + 4°C. Warmer scenario = + 4°C. For the simulated baseline period, the range of unit stream power values are from the top 100 parameter sets (n = 100). For future scenarios, the range of unit stream power values are from the 5th and 95th percentiles of all 5000 simulations (n = 4500). Median unit stream power is the median value from the averages for all simulations. Unit stream power is not calculated for the observed baseline period due to gaps in data.

Catchment	**Baseline period model median stream power and range (W/m^2)**	**Drier scenario median stream power and range (W/m^2)**	**Drier and warmer scenario median stream power and range (W/m^2)**	**Warmer scenario median stream power and range (W/m^2)**
Chile				
Choapa	75 (57, 95)	42 (27, 60)	35 (23, 51)	85 (61, 109)
Aconcagua	266 (234, 299)	175 (151, 200)	145 (115, 172)	237 (200, 276)
Colorado	86 (77, 92)	57 (51, 64)	50 (44, 56)	77 (70, 84)
Tinguiririca	144 (123, 159)	96 (85, 109)	92 (79, 105)	140 (122, 161)
Argentina				
Mendoza	278 (244, 315)	163 (139,186)	122| (106,141)	202 (175, 228)
Tunuyán	57 (53, 62)	34 (30, 38)	25 (22, 28)	39 (34, 43)
Diamante	83 (76, 90)	49 (42, 55)	39 (33, 46)	66 (57, 76)
Atuel	26 (23, 29)	15 (13, 17)	12 (10, 14)	21 (18, 24)

Table S7. Average center of volume for each time series for the modeled baseline period and for all future scenarios. Drier scenario = -30% precipitation. Drier and warmer scenario = -30% precipitation + 4°C. Warmer scenario = + 4°C. For the simulated baseline time period, range of center of volume is from the top 100 parameter sets (n = 100). For future scenarios, the range of center of volume is from the 5th and 95th percentiles of all 5000 simulations (n = 4500). Center of volume is calculated as the day on which half of the observed streamflow in a catchment for a given water year has passed the catchment gauging station (Court, 1962), with the beginning of the water year occurring on April 1. Median center of volume is the median value from the averages for all simulations. Center of volume is not calculated for the observed baseline period due to gaps in data.

Catchment	**Baseline period model median center of volume and range (day)**	**Drier scenario median center of volume and range (day)**	**Drier and warmer scenario median center of volume and range (day)**	**Warmer scenario median center of volume and range (day)**
Chile				
Choapa	224 (216, 235)	212 (202, 221)	196 (188, 205)	189 (179, 197)
Aconcagua	242 (232, 254)	216 (202, 232)	181 (168, 193)	178 (165, 190)
Colorado	250 (240, 257)	233 (222, 244)	195 (184, 206)	190 (174, 205)
Tinguiririca	233 (217, 241)	208 (192, 241)	166 (154, 178)	161 (150, 173)
Argentina				
Mendoza	264 (254, 270)	257 (245, 265)	232 (222, 240)	231 (223, 231)
Tunuyán	270 (265, 275)	266 (260, 272)	247 (239, 254)	241 (234, 247)
Diamante	248 (242, 253)	240 (232, 247)	199 (189, 207)	199 (189, 208)
Atuel	248 (241, 255)	239 (231, 249)	212 (204, 219)	214 (207, 222)

Table S8. Erosion rates (E) calculated using observed and modeled time series of streamflow for the baseline period and for all future scenarios. Drier scenario = -30% precipitation. Drier and warmer scenario = -30% precipitation + 4°C. Warmer scenario = + 4°C. For all simulated time series, the erosion rate shown is the median erosion rate from all runs of a given scenario for that catchment. The percent change shown for all future scenarios is in reference to the modeled baseline period.

Catchment	**Baseline period observed E (mm/a)**	**Baseline period model median E (mm/a)**	**Drier scenario median E (mm/a) and % change**	**Drier and warmer scenario median E (mm/a) and % change**	**Warmer scenario median E (mm/a) and % change**
Chile					
Choapa	0.0061	0.0051	0.0021 (-59%)	0.0017 (-67%)	0.0061 (+20%)
Aconcagua	0.0690	0.0572	0.0282 (-51%)	0.0216 (-62%)	0.0504 (-12%)
Colorado	0.2130	0.1694	0.0536 (-68%)	0.0388 (-77%)	0.1467 (-13%)
Tinguiririca	0.1370	0.1047	0.0541 (-48%)	0.0586 (-44%)	0.1825 (+74%)
Argentina					
Mendoza	0.2760	0.1989	0.0303 (-85%)	0.0086 (-96%)	0.0506 (-75%)
Tunuyán	0.3390	0.2487	0.0551 (-78%)	0.0175 (-93%)	0.0590 (-76%)
Diamante	0.1600	0.1285	0.0300 (-77%)	0.0157 (-88%)	0.0514 (-60%)
Atuel	0.0810	0.0726	0.0134 (-82%)	0.0077 (-89%)	0.0305 (-58%)

Table S9. Average height of June, July, August, and September (JJAS) isotherm for the baseline period and under 4°C of warming. Average slope of each catchment below the average JJAS isotherm for the baseline period and the average slope of the area between the average baseline period JJAS isotherm and 4°C of warming JJAS isotherm is also shown.

Catchment	Mean baseline JJAS isotherm elevation (m)	Mean slope below baseline JJAS isotherm (°)	Mean +4 °C JJAS isotherm elevation (m)	Mean slope between baseline JJAS isotherm and +4 °C JJAS isotherm (°)
Chile				
Choapa	3694	22.35	4367	24.27
Aconcagua	3404	27.91	4105	26.44
Colorado	3365	27.44	4058	28.45
Tinguiririca	2589	26.79	3241	27.12
Argentina				
Mendoza	3016	15.65	3706	27.68
Tunuyán	2589	31.32	3241	27.45
Diamante	2532	13.58	3206	21.76
Atuel	2610	13.14	3279	20.51

References

Alvarez-Garreton, C., Mendoza, P.A., Boisier, J.P., Addor, N., Galleguillos, M., Zambrano-Bigiarini, M., et al. 2019. The CAMELS_CL dataset: catchment attributes and meteorology for large sample studies – Chile dataset. *Hydrology and Earth System Sciences,* 22: 5817-5846. https://doi.org/10.5194/hess-22-5817-2018

Asselman, N.E.M. 1999. Suspended sediment dynamics in a large drainage basin: the River Rhine. *Hydrological Processes,* 13: 1437-1450. https://doi.org/10.1002/(SICI)1099-1085(199907)13:10<1437::AID-HYP821>3.0.CO;2-J

Ayala, Á., Farías-Barahona, D., Huss, M., Pellicciotti, F., McPhee, J., & Farinotti D. 2020. Glacier runoff variations since 1955 in the Maipo River basin, in the semiarid Andes of central Chile. *The Cryosphere,* 14: 2005-2027. https://doi.org/10.5194/tc-14-2005-2020

Bagnold, R. 1966. An Approach to the Sediment Transport Problem from General Physics. United States Geological Survey Professional Paper 422-I. https://doi.org/10.3133/pp422I

Baldis, C.T., & Liaudat, D.T. 2019. Rockslides and rock avalanches in the Central Andes of Argentina and their possible association with permafrost degradation. *Permafrost and Periglacial Processes,* 30(4): 330-347. https://doi.org/10.1002/ppp.2024

BDHI 2020. Base de Datos Hidrilógica Integrada. http://bdhi.hidricosargentina.gob.ar.

Buchhorn, M., Smets, B., Bertels, L., Lesiv, M., Tsendbazar, N.-E., Masiliunas, D., et al. 2020. Copernicus Global Land Service: Land Cover 100m: Collection 3: epoch 2019: Globe (Version V3.0.1) [Data set]. Zenodo. https://doi.org/10.5281/zenodo.3939050

Bergström, S. 1992. The HBV Model: Its Structure and Applications. Swedish Meteorological and Hydrological Institute (SMHI), Hydrology, Norrköping, 35 p.

Bilotta, G.S., & Brazier, R.E. 2008. Understanding the influence of suspended solids on water quality and aquatic biota. *Water Research,* 42: 2849-2861. https://doi.org/10.1016/j.watres.2008.03.018

Bodin, X., Rojas, F., & Brenning, A. 2010. Status and evolution of the cryosphere in the Andes of Santiago (Chile, 33.5°S.). *Geomorphology,* 118: 453-464. https://doi.org/10.1016/j.geomorph.2010.02.016

Bozkurt, D., Rojas, M., Boisier, J.P, & Valdiviesco, J. 2018. Projected hydroclimate changes over Andean basins in central Chile from downscaled CMIP5 models under the low and high emission scenarios. *Climate Change,* 150: 131-147. https://doi.org/10.1007/s10584-018-2246-7

Carretier, S., Regard, V., Vassallo, R., Aguilar, G., Martinod, J., Riquelme, R., et al. 2013. Slope and climate variability control of erosion in the Andes of central Chile. *Geology, 41(2)*, 195-198. https://doi.org/10.1130/G33735.1

Carrillo, R., & Mao, L. 2020. Coupling sediment transport dynamics with sediment and discharge sources in a glacial Andean basin. *Water,* 12(12): 3452. https://doi.org/10.3390/w12123452

Chen, J., Brissette, F.P., & Leconte, R. 2012. WeaGETS – A Matlab-based daily scale weather generator for generating precipitation and temperature. *Procedia Environmental Sciences,* 13: 2022-2235. https://doi.org/10.1016/j.proenv.2012.01.211

Cortés, G., Vargas, X., & McPhee, J. 2011. Climatic sensitivity of streamflow timing in the extratropical western Andes Cordillera. *Journal of Hydrology,* 405(1-2): 93-109. https://doi.org/10.1016/j.jhydrol.2011.05.013

Costa, A., Molnar, P., Stutenbecker, L., Bakker, M., Silva, T.A., Schlunegger, F., et al. 2018. Temperature signal in suspended sediment export from an Alpine catchment. *Hydrology and Earth System Sciences,* 22: 509-528. https://doi.org/10.5194/hess-22-509-2018

Court, A. 1962. Measures of Streamflow Timing. *Journal of Geophysical Research, 67(11)*: 4335-4338. https://doi.org/10.1029/JZ067i011p04335

Crespo, S.A., Fernandoy, F., Cara, L., Klarian, S., & Lavergne, C. 2020. First snow, glacier and groundwater contribution quantification in the upper Mendoza River basin using stable water isotopes. *Isotopes in Environmental and Health Studies,* 56(5-6): 566-585. https://doi.org/10.1080/10256016.2020.1797713

Dawson, E.J., & Macklin, M.G. 1998. Speciation of heavy metals on suspended sediment under high flow conditions in the River Aire, West Yorkshire, UK. *Hydrologic Processes,* 12: 1483-1494. https://doi.org/10.1002/(SICI)1099-1085(199807)12:9<1483::AID-HYP651>3.0.CO;2-W

DGA 2020. Información Oficial Hidrometeorológica y de Calidad de Aguas en Línea. https://snia.mop.gob.cl/BNAConsultas/reportes.

Dussaillant, I., Berthier, E., Brun, F., Masiokas, M., Hugonnet, R., Favier, V., et al. 2019. Two decades of glacier mass loss along the Andes. *Nature Geoscience,* 12: 802-808. https://doi.org/10.1038/s41561-019-0432-5

East, A.E., & Sankey, J.B. 2020. Geomorphic and sedimentary effects of modern climate change: current and anticipated future conditions in the western United States. *Reviews of Geophysics*, 58: e2019RG000692. https://doi.org/10.1029/2019RG000692

Ferguson, R.I. 1986. River Loads Underestimated by Sediment Rating Curves. *Water Resources Research,* 22(1): 74-76. https://doi.org/10.1029/WR022i001p00074

Funk, C., Peterson, P., Landsfeld, M., Pedreros, D., Verdin, J., Shukla, S., et al. 2015. The climate hazards infrared precipitation with stations–a new environmental record for monitoring extremes. *Scientific Data,* 2: 150066. https://doi.org/10.1038/sdata.2015.66

Gao, P. 2008. Understanding watershed suspended sediment transport. *Progress in Physical Geography,* 32(3): 243-263. https://doi.org/10.1177/0309133308094849

Garreaud, R.D., Alvarez-Garreton, C., Barichivich, J., Boisier, J.P., Christie, D., Galleguillos, M., et al. 2017. The 2010-2015 Megadrought in central Chile: impacts on regional hydroclimate and vegetation. *Hydrology and Earth System Sciences,* 21: 6307-6327. https://doi.org/10.5194/hess-21-6307-2017

Gupta, H.V., Kling, H., Yilmaz, K.K., & Martinez, G.F. 2009. Decomposition of the mean squared error and NSE performance criteria: Implications for improving hydrologic modeling. *Journal of Hydrology,* 377: 80-91. https://doi.org/10.1016/j.jhydrol.2009.08.003

Hirschberg, J., Fatichi, S., Bennett, G.L., McArdell, B.W., Peleg, N., Lane, S.N., et al. 2021. Climate change impacts on sediment yield and debris-flow activity in an alpine catchment. *Journal of Geophysical Research: Earth Surface,* 126: e2020JF005739. https://doi.org/10.1029/2020JF005739

Hoke, G.D., Giambiagi, L.B., Garzione, C.N., Mahoney, J.B., & Strecker, M.R. 2014. Neogene paleoelevation of intermontane basins in a narrow, compressional mountain range, southern Central Andes of Argentina. *Earth and Planetary Science Letters,* 406: 153-164. http://dx.doi.org/10.1016/j.epsl.2014.08.032

Ibañez, M., Gironás, J., Oberli, C., Chadwick, C., & Garreaud, R. 2020. Daily and seasonal variation of the surface temperature lapse rate and 0°C isotherm height in the western subtropical Andes. *International Journal of Climatology*, 41(S1): E980-E999. https://doi.org/10.1002/joc.6743

Iida, T., Kajihara, A., Okubo, H., & Okajima, K. 2012. Effect of seasonal snow cover on suspended sediment runoff in a mountainous catchment. *Journal of Hydrology,* 428-429: 116-128. https://doi.org/10.1016/j.jhydrol.2012.01.029

Jarvis, A., Reuter, H., Nelson, A., & Guevara, E. 2008. Hole-filled seamless SRTM data V4. International Centre for Tropical Agriculture (CIAT). Available from https://cgiarcsi.community/data/srtm-90m-digital-elevation-database-v4-1/.

Kokelj, S.V., Lacelle, D., Lantz, T.C., Tunnicliffe, J., Malone, L., Clark, I.D., & Chin, K.S. 2013. Thawing of massive ground ice in mega slumps drives increases in stream sediment and solute flux across a range of watershed scales. *Journal of Geophysical Research: Earth Surface,* 118: 681-692. https://doi.org/10.1002/jgrf.20063

Leopold, L.B., Wolman, M.G., & Miller, J.P. 1964. Fluvial processes in geomorphology (W.H. Freeman and Company: San Francisco, CA). 522 p.

Lewis, T., & Lamoureux, S.F. 2010. Twenty-first century discharge and sediment yield predictions in a small high Arctic watershed. *Global and Planetary Change*, 71: 27-41. https://doi.org/10.1016/j.gloplacha.2009.12.006

Li, D., Li., Z., Zhou, Y., & Lu, X. 2020. Substantial increases in the water and sediment fluxes in the headwater region of the Tibetan Plateau in response to global warming. *Geophysical Research Letters,* 47(11): e2020GL087745. https://doi.org/10.1029/2020GL087745

Li, L., Ni, J., Chang, F., Yue, Y., Frolova, N., Magritsky, D., et al. 2020. Global trends in water and sediment fluxes of the world's large rivers. *Science Bulletin,* 65: 62-69. https://doi.org/10.1016/j.scib.2019.09.012

Mao., L., & Carrillo, R. 2017. Temporal dynamics of suspended sediment transport in a glacierized Andean basin. *Geomorphology,* 287: 116-125. http://dx.doi.org/10.1016/j.geomorph.2016.02.003

Masiokas, M.H., Villalba, R., Luckman, B.H., Le Quesne, C., & Aravena, J.C. 2006. Snowpack Variations in the Central Andes of Argentina and Chile, 1951-2005: Large-Scale Atmospheric Influences and Implications for Water Resources in the Region. *Journal of Climate,* 19: 6334-6352. https://doi.org/10.1175/JCLI3969.1

McClain, M.E., & Naiman, R.J. 2008. Andean influences on the biogeochemistry and ecology of the Amazon River. *BioScience,* 58(4): 325-338. https://doi.org/10.1641/B580408

Molnar, P., Anderson, R.S., Kier, G., & Rose, J. 2006. Relationships among probability distributions of stream discharges in floods, climate, bed load transport, and river incision. *Journal of Geophysical Research: Earth Surface,* 111: F02001. https://doi.org/10.1029/2005JF000310

Morieras, S.M. 2005. Climatic effect of ENSO associated with landslide occurrence in the Central Andes, Mendoza Province, Argentina. *Landslides*, 2: 53-59. https://doi.org/10.1007/s10346-005-0046-4

Nash, J.E., & Sutcliffe, J.V. 1970. River flow forecasting through conceptual models: Part I – A discussion of principles. *Journal of Hydrology,* 10: 282-290. https://doi.org/10.1016/0022-1694(70)90255-6

Pepin, E., Carretier, S., Guyot, J.L., & Escobar, F. 2010. Specific sediment yields of the Andean rivers of Chile and their relationship to climate, slope and vegetation. *Hydrologic Sciences Journal,* 55(7): 1190-1205. https://doi.org/10.1080/02626667.2010.512868

Pereira, S.R., Marquardt, C., Beriain, E., & Lambert, F. 2021. Permafrost evolution in a mountain catchment near Santiago de Chile. *Journal of South American Earth Sciences,* 109: 103293. https://doi.org/10.1016/j.jsames.2021.103293

Ragettli, S., Immerzeel, W.W., & Pellicciotti, F. 2016. Contrasting climate change impact on river flows from high-altitude catchments in the Himalayan and Andes Mountains. *Proceedings of the National Academy of Sciences*, 113(33): 9222-9227. https://doi.org/10.1073/pnas.1606526113

Rivera, J.A., Marianetti, G., & Hinrichs, S. 2018. Validation of CHIRPS precipitation dataset along the Central Andes of Argentina. *Atmospheric Research*, 213: 437-449. https://doi.org/10.1016/j.atmosres.2018.06.023

Rivera, J.A., Penalba, O.G., Villalba, R., & Araneo, D.C. 2017. Spatio-Temporal Patterns of the 2010-2015 Hydrological Drought across the Central Andes, Argentina. *Water,* 9(9): 652. https://doi.org/10.3390/w9090652

Runkel, R.L., Crawford, C.G., & Cohen, T.A. 2004. Load Estimator (LOADEST): A FORTRAN program for estimating constituent loads in streams and rivers. United States Geological Survey Techniques and Methods Book 4, Chapter A5 (United States Geological Survey: Reston, VA). 75 p. https://doi.org/10.3133/tm4A5

Rusticucci, M., Zazulie, N., & Raga, G.B. 2014. Regional winter climate of the southern central Andes: Assessing the performance of ERA-Interim for climate studies. *Journal of Geophysical Research: Atmospheres,* 119: 8568-8582. https://doi.org/10.1002/2013JD021167

Seibert, J., & Vis, M.J.P. 2012. Teaching hydrological modeling with a user-friendly catchment-runoff-model software package. *Hydrology and Earth System Sciences,* 16: 3315-3325. https://doi.org/10.5194/hess-16-3315-2012

Sepúlveda, S.A., Morieras, S.M., Marisol, L., & Alejandro, A. 2015. Debris flow in the Andean ranges of central Chile and Argentina triggered by 2013 summer storms: characteristics and consequences. *Landslides,* 12(1): 115-133. https://doi.org/10.1007/s10346-014-0539-0

Singh, R., Wagener, T., Crane, R., Mann, M.E., & Ning, L. 2014. A vulnerability driven approach to identify adverse climate and land use change combinations for critical hydrologic indicator thresholds: Application to a watershed in Pennsylvania, USA. *Water Resources Research,* 50(4): 3409-3427. https://doi.org/10.1002/2013WR014988

Dirección de Sistemas de Monitoreo de los Recursos Hídricos (SMRH). 2021. Muestro de Material en Suspensión.

Snyder, N.P., Rubin, D.M., Alpers, C.N., Childs, J.R., Curtis, J.A., Flint, L.E., &, Wright, S.A. 2004. Estimating accumulation rates and physical properties of sediment behind a dam:

Englebright Lake, Yuba River, northern California. *Water Resources Research,* 40: W11301. https://doi.org/10.1029/2004WR003279

Somers, L.D., McKenzie, J.M., Mark, B.G., Lagos, P., Ng, G.-L.C., Wickert, A.D., et al. 2019. Groundwater buffers decreasing glacier melt in an Andean watershed – but not forever. *Geophysical Research Letters,* 46(22): 13016-13026. https://doi.org/10.1029/2019GL084730

Starke, J., Ehlers, T.A., & Schaller, M. 2020. Latitudinal effect of vegetation on erosion rates identified along western South America. *Science,* 367: 1358-1361. https://doi.org/10.1126/science.aaz0840

Syvitski, J.P.M. 2002. Sediment discharge variability in Arctic rivers: implications for a warmer future. *Polar Research,* 21(2): 323-330. https://doi.org/10.3402/polar.v21i2.6494

Thomas, B.F., & Famiglietti, J.S. 2019. Identifying Climate-Induced Groundwater Depletion in GRACE Observations. *Scientific Reports,* 9: 4124. http://doi.org/10.1038/s41598-019-40155-y

Thornthwaite, C.W., & Mather, J.R. 1955. The Water Balance. *Drexel Institute of Climatology, Laboratory of Climatology: Publications in Climatology,* 8(1). 101 p.

Tucker, G.E., & Bras, R.L. 1998. Hillslope processes, drainage density, and landscape morphology. *Water Resources Research,* 34(10): 2751-2764. https://doi.org/10.1029/98WR01474

RGI Consortium 2017. Randolph Glacier Inventory – A Dataset of Global Glacier Outlines: Version 6.0: Technical Report, Global Land Ice Measurements from Space, Colorado, USA. Digital Media. https://doi.org/10.7265/N5-RGI-60.

Val, P., Venerdini, A.L., Ouimet, W., Alvaredo, P., & Hoke, G.D. 2018. Tectonic control of erosion in the southern Central Andes. *Earth and Planetary Science Letters,* 482: 160-170. https://doi.org/10.1016/j.epsl.2017.11.004

Viale, M., & Garreaud, R. 2015. Orographic effects of the subtropical and extratropical Andes on upwind precipitating clouds. *Journal of Geophysical Research: Atmospheres*, 120(10): 4962-4974. https://doi-org.libezproxy2.syr.edu/10.1002/2014JD023014

Viale, M., & Norte, F.A. 2009. Strong cross-barrier flow under stable conditions producing intense winter orographic precipitation: A case study over the subtropical Central Andes. *Weather and Forecasting,* 24(4): 1009-1031. https://doi.org/10.1175/2009WAF2222168.1

Viale, M. & Nuñez, M.N. 2011. Climatology of winter orographic precipitation over the subtropical Central Andes and associated synoptic characteristics. *Journal of Hydrometeorology,* 12(4): 481-507. https://doi.org/10.1175/2010JHM1284.1

Vicuña, S., Garreaud, R.D., & McPhee, J. 2011. Climate change impacts on the hydrology of a snowmelt driven basin in semiarid Chile. *Climatic Change,* 105: 469-488. https://doi.org/10.1007/s10584-010-9888-4

Vicuña, S., Gironás, J., Meza, F.J., Cruzat, M.L., Jelinek, M., & Bustos, E. 2013. Exploring possible connections between hydrological extreme events and climate change in central south Chile. *Hydrologic Sciences Journal,* 58(8): 1598-1619. https://doi-org.libezproxy2.syr.edu/10.1080/02626667.2013.840380

Viviroli, D., Archer, D.R., Buytaert, W., Fowler, H.J., Greenwood, G.B., Hamlet, A.F., et al. 2011. Climate change and mountain water resources: overview and recommendations for research, management and policy. *Hydrology and Earth System Sciences,* 15: 471-504. https://doi.org/10.5194/hess-15-471-2011

Wulf, H., Bookhagen, B., & Scherler, D. 2012. Climatic and geologic controls on suspended sediment flux in the Sutlej River Valley, western Himalaya. *Hydrology and Earth System Sciences,* 16: 2193-2217. https://doi.org/10.5194/hess-16-2193-2012

Yang, G., Chen, Z., Yu, F., Wang, Z., Zhao, Y, & Wang, Z. 2007. Sediment rating parameters and their implications: Yangtze River, China. *Geomorphology,* 85: 166-175. https://doi.org/10.1016/j.geomorph.2006.03.016

Chapter 3

Estimating Reservoir Infill Rates and Sediment Flux Dynamics in the Argentine High Andes with Paired ^{14}C and ^{10}Be in River Sand

Chapter 3 is in preparation for submission to *Geology*

Abstract

Water resources from the high Andes Mountains of Argentina are critically important to millions of people living in the arid provinces of Mendoza and San Juan. Glaciers and snowmelt supplying regional streams and rivers are under increasing stress from drought, warming temperatures, and deceasing precipitation. Water reservoirs have been built as a solution, but their lifespans are impacted by sediment accumulation in this high relief, tectonically active part of the world. Stream gauge data and cosmogenic ^{10}Be were used to estimate erosion rates and sediment flux for six rivers and predict lifespans for five existing reservoirs in the high Andes. Similarity between ^{10}Be and stream gauge results indicates that ^{10}Be is suitable for this purpose, with ^{10}Be predicted reservoir lifespans ranging from 129 to 217 years. Five ^{10}Be samples were also paired with an analysis of ^{14}C concentrations to study sediment transport dynamics in contributing mountainous watersheds. Low ^{14}C/^{10}Be ratios suggest that despite agreement between decadal and millennial scale erosion rates from ^{10}Be, sediment transport times through these complex watersheds may range from a minimum of 10,000 to 19,000 years.

1. Introduction

Over recent human history, glaciers and snowmelt from the high Andes have provided a lifeline to millions of people living in Argentina's Mendoza and San Juan provinces. In this arid region, cities such as Mendoza and San Juan receive less than 200 mm of rainfall annually and irrigation is an essential component of a robust agricultural sector (Crespo et al., 2020; Masiokas et al., 2006; Morris, 1969). Streamflow is primarily snowmelt driven, with glacier melt buffering runoff during the warmer months of the year (Crespo et al., 2020; Leiva, 2007; Leiva, 1999). However, glacier retreat has been widely documented in the Argentine high Andes during the twentieth and early twenty-first centuries (Barros et al., 2015; Masiokas et al., 2009; Leiva, 2007) and a regional hydrologic drought from 2010 to 2015 put further pressure on limited water supplies (Rivera et al., 2017). Water resources in the area are expected to come under continued stress from rising air temperatures and declines in precipitation throughout the twenty-first century (Barros et al., 2015).

In this arid and mountainous region, a number of large reservoirs have been constructed as a solution to water scarcity (e.g., Panedile, 2021; ORSEP, 2021; Carmona et al., 2014) and additional reservoirs are in the planning stages. However, rivers draining the high relief, tectonically active high Andes can carry significant sediment loads (Val et al., 2018; Pepin et al., 2013). These sediments accumulate in reservoirs (Snyder et al., 2004), reducing their storage capacity, impacting maximum withdrawal rates, and shortening their useful lifespans (Heineke et al., 2017; Sabo et al., 2010). As a case in point, the Carrizal reservoir on the Río Tunuyán lost nearly 114.4 hm^3 of storage capacity from the time it was completed in 1971 to the year 2013, a nearly 30% reduction in the overall storage capacity as measured from land fill level (EVARSA, 2013). Because reservoirs can also carry significant economic, social, and environmental costs (Kornijów, 2009), quantifying how long they may be relied upon as a source of water for their communities is critically important (Heineke et al., 2017).

Stream gauges located near the foot of the Andes record streamflow and sediment data and provide a reasonable first approximation of sediment fluxes from the high mountains over recent decades. As other researchers have noted, however, these decadal scale rates can diverge from longer-term catchment-averaged erosion rates if they under- over over-represent rare but high magnitude events that mobilize regolith, such as landslides (Heineke, 2017; Kirchner, 2001), which can have an outsized impact on erosion rates (Molnar et al., 2006). Stream gauging stations are also not always situated near locations where information about sediment fluxes is most needed, such as at sites where infrastructure projects are proposed.

Cosmogenic radionuclides offer an alternative to stream gauge data and their use to estimate catchment-wide erosion rates is well established (von Blankenburg, 2005; Granger et al., 1996; Bierman, 1994). ^{10}Be, in particular, has emerged as a common nuclide to pair with stream gauge sediment data to establish background erosion rates (Val et al., 2018; Wittman et al., 2011; Kirchner et al., 2001) and has also been used as a tool to estimate reservoir lifespans (Heineke, 2017). Nonetheless, sediment transport dynamics from the hillslope to the catchment outlet may not be fully evident from short-term gauge data or ^{10}Be erosion rates that can integrate over thousands or tens of thousands of years.

Pairing two cosmogenic nuclides with different half-lives provides a way to determine if erosional processes in a catchment deviate from an assumption of constant, steady-state erosion (Gosse & Phillips, 2001; Lal, 1991). ^{10}Be has a comparatively long half-life of 1.38 x 10^6 years (Chmeleff et al., 2010) and sea-level and high latitude (“SLHL”) production rate of 3.69 to 4.09 atoms per gram year, based on the scaling method used (Phillips et al., 2016). This long half-life and low production rate can make ^{10}Be insensitive to changes in erosional processes that take place over timescales of up to even tens of thousands of years (Niemi et al., 2005). ^{14}C, in contrast, with a short half-life of 5.73 x 10^3 years (Bierman, 1994) and SLHL production rate of 12.2 to 13.4 atoms per gram per year (Phillips et al., 2016), is highly sensitive to sub thousand year disturbances (Hippe et al., 2019; Hippe et al., 2012). Its use has been limited until only recently, however, due to the difficulty of measurement of in situ ^{14}C (Pigati et al., 2010). In the last few years, the ^{14}C-^{10}Be nuclide pair has been used to explore complex erosional histories deviating from steady-state, including sediment storage (Hippe et al., 2019; Kober et al., 2019; Kim et al., 2016, Hippe et al., 2012).

In this study, stream gauge data and in situ cosmogenic ^{10}Be from quartz bearing river sand are used to estimate background erosion rates for six major river systems in the high Andes of the Mendoza and San Juan provinces. ^{10}Be samples and stream gauge stations at different points along these river systems provide the opportunity to investigate sediment flux dynamics from the higher elevations towards the lowlands just outside of the mountain front. Erosion rates from ^{10}Be and gauge data are also used to predict the lifespans of five reservoirs sited in or near the base of the Andes and to compare these two methods. Finally, five of the higher elevation ^{10}Be samples were paired with in situ ^{14}C to explore hillslope residence times and potential disequilibria with gauge and ^{10}Be erosion rates. Results from this study have broad implications for the use of ^{10}Be as a tool for estimating reservoir lifespans and for investigating sediment flux dynamics that may be masked by decadal- or millennial-scale methods.

2. Materials and Methods

2.1. Study Area

The study area covers the Argentine high Andes from approximately 29 to 35° S with elevations ranging from under 1000 m in the eastern lowlands to over 6,000 m at the highest peaks. Regional climate is strongly influenced by the high Andes, which act as an orographic barrier to strong storm systems originating from the Pacific. While winter precipitation events on the western, Chilean side of the Andes can exceed 100 mm in a single event, precipitation from these events often does not reach the lowlands on the Argentine side of the range (Viale & Nuñez, 2011; Viale and Norte, 2009; Masiokas et al., 2006). As a result, during the cold season precipitation on the Argentine side of the Andes is not correlated with precipitation in the city of Santiago, Chile. On an annual basis, the cities of Mendoza and San Juan in Argentina receive 31% less annual rainfall than Santiago (Masiokas et al., 2006). Climate in the Mendoza and San Juan provinces is also influenced by the South Atlantic high pressure system (Barros et. al., 2015). Precipitation in the eastern Andes peaks in the warmer months, principally fueled by moist air masses originating in the northeast and localized atmospheric convection (Masiokas et al., 2006), and tends to be higher in El Niño years. Runoff from the mountains is highest during December and January and is largely snowmelt driven (Barros et al., 2015).

A combination of active uplift and high topography make the Andes prone to significant sediment generation. The western margin of South America is tectonically active, as the Nazca plate is being subducted beneath the South American plate. The region extending from 27° S to 32° S is characterized by sub-horizonal, “flat-slab,” subduction of the Nazca plate at ~100 km depth and an absence of arc magmatism (Cahill and Isacks, 1992; Mulcahy et al., 2014). Magmatism resumes south of 33° S, where the subduction angle of the Nazca plate is approximately 30° (Cahill and Isacks, 1992). Valley headwall relief south of the slab-dip transition additionally suggests that the Andes are experiencing active rock uplift in that region (Hoke et al., 2014). These factors create an environment with a high potential for sediment generation, and previous studies have recorded millennial-scale erosion rates in the central Argentine Andes as high as 0.300 mm/a using river gauge data and ^{10}Be from river sand (Val et al., 2018; Pepin et al., 2013).

2.2. River Gauge Data

Decadal-scale erosion rates were calculated for nine different sites in the southern Central Andes using sediment and streamflow data from Argentina's Base de Datos de Hidrológica Integrada (BDHI), which are available from a public website (BDHI, 2021). The number of observations and years of observation for each site are available in the supplementary information (Table S1). Contributing areas were calculated for each gauge station using 1 arc second Shuttle Radar Topography Mission (SRTM) data and ranged from just over 560 km^2 to over 23,800 km^2 (Figure 1; Table 1). Erosion rates for each gauge location were calculated by fitting a power law to stream discharge and sediment flux data (Gao, 2008), following prior approaches used in the region (Val et al., 2018). This power law was used to calculate the average annual volume of bedrock eroded from each catchment, assuming an average bedrock density of 2650 kg m^{-3}. The eroded volume was then divided by the area of each respective catchment to calculate an erosion rate. An uncertainty of 30% was applied to all erosion rates calculated using river gauge data (Carretier et al., 2013, Val et al., 2018).

2.3. Cosmogenic Nuclide Samples

To calculate long-term, background erosion rates in the study region, nine samples of quartz-bearing river sand were collected from six rivers with perennial water flow on the eastern flank of the Andes spanning from approximately 29° to 35° S for ^{10}Be analysis (Figure 1; Table 2). ^{10}Be is principally produced through spallation reactions in O, Mg, Si, and Fe and its most common target mineral is quartz (Lal, 1991). With a half-life of 1.38 x 10^6 years (Chmeleff et al., 2010), ^{10}Be is suitable for the calculation of erosion rates at the millennial scale (Val et al., 2018). Each of the sample sites were located either upstream from existing reservoirs or in locations that have been under consideration for future water retention projects (Figure 1). Several sites are also in close proximity to existing river gauge stations, allowing for comparison of erosion rates calculated at both decadal and millennial scales. It was assumed that each sample collected represented a well-mixed aggregate of grains from upstream contributing areas, allowing for estimation of a catchment-averaged erosion rate at each site (i.e., von Blanckenburg, 2005; Granger et al., 1996). Conceptually, the catchment-averaged erosion rate can be modeled using the following formulation for a sample collected at the surface and assuming the case of steady-state erosion:

$$\varepsilon = \frac{P(0) - N(t)\lambda}{N(t)\mu}$$

where, ε is the catchment-averaged erosion rate, $P(0)$ is the ^{10}Be production rate, $N(t)$ is the nuclide concentration at time t, λ is a disintegration constant, and μ is an absorption coefficient equal to the rock density divided by the mean free path (von Blanckenburg 2005, Lal 1991).

We isolated pure quartz from each sample (Al concentrations of ~100 ppm or lower and concentrations of ~40 ppm or lower for all other cations) at Syracuse University for subsequent ^{14}C and ^{10}Be analysis. Quartz purity was assessed on a 0.25 g aliquot of quartz dissolved in solution of concentrated HF and H_2SO_4 and analyzed via inductively coupled plasma-optical emission spectrometry at the State University of New York's College of Environmental Science and Forestry. Chemical separation of ^{10}Be was performed at the University of Buffalo following procedures outlined in Tulenko et al. (2020), where samples were spiked with a known concentration of ^{9}Be carrier solution and dissolved in hydrofluoric acid. ^{10}Be was extracted by cation exchange columns and subsequently oxidized in a muffle furnace. Finally, BeO was mixed with niobium powder and packed in cathodes for accelerator mass spectrometry (AMS) analysis at Lawrence Livermore National Laboratory. Measured ^{10}Be/^{9}Be ratios for the nine samples ranged from 1.429 x 10^{-12} to 1.022 x 10^{-13}. Complete AMS results are available in the supplementary information (Table S2).

Catchment-averaged erosion rates were estimated using version 3.0 of the online cosmogenic nuclide calculator of Balco et al. (2008, available at https://hess.ess.washington.edu/), scaling for altitude and latitude using the LSD nuclide-specific (LSDn) framework (Lifton et al., 2014). This method accounts for the muonic contribution to cosmogenic nuclide production, although muons comprise less than 3.0% of total ^{10}Be production in quartz at SLHL (Braucher et al., 2009, Braucher et al., 2003). The mean altitude for each catchment was calculated by masking out non-quartz bearing lithologies and weighed by catchment hypsometry. For each sample site, a shielding correction was also applied based on average catchment slope (Dunne et al., 1999) and the percentage of each catchment covered by glaciers. Glacier area was calculated using the Randolph Glacier Inventory version 6.0 (RGI Consortium 2017). Although glacier coverage has varied over time, it is likely to have been similar over the integration time of each sample. Despite this uncertainty, glacier coverage accounts for less than 5% of most catchments today and no more than 9% of any catchment. Each of the inputs used in the online cosmogenic nuclide calculator are available in the supplementary information (Table S3). For comparison to prior studies in the Argentine high Andes estimating erosion rates from ^{10}Be in river sand, erosion rates using data from Val et al. (2018) and Pepin et al. (2013) were recalculated using LSDn scaling. Data inputs for these samples are also available in the supplementary information (Table S4).

To analyze potential sediment flux disequilibria, five samples analyzed for ^{10}Be concentrations were analyzed for their concentrations of ^{14}C. The five samples, chosen predominantly from high mountain locations, were SJ17RSJt, SJ17RB, MDZ17RM2, MDZ17RT2, and MDZ17RA. The quartz splits for ^{14}C analysis underwent ^{14}C extraction at the Purdue Rare Isotope Measurement Laboratory (PRIME Lab) following procedures described more fully in Graham et al. (2019) and Lifton et al. (2015). Quartz samples were placed in Al_2O_3 sample boats with a degassed $LiBO_2$ flux and heated to 600° C to remove potential contaminants. The quartz samples were then dissolved at 1100 °C in Research Purity O_2 for oxidation of evolved carbon species to CO_2. The CO_2 was purified and converted to graphite for AMS analysis, which was also performed at PRIME Lab (Graham et al., 2019; Lifton et al., 2015).

2.4 Reservoir Lifespans

Erosion rates calculated from stream gauge data and ^{10}Be samples were used to estimate the lifespans of five existing reservoirs at the eastern margin of the Andes. The location of each reservoir and the nearest ^{10}Be or stream gauge sites used to calculate erosion rates are shown in Table 3. Reservoir volumes as listed in previously published works or by organizations responsible for management, oversight, or construction of each reservoir (ORSEP, 2021; Panedile, 2021; Carmona et al., 2014) were used, although the actual usable volume of each reservoir is likely less. For each reservoir, the contributing area for the main river emptying into the reservoir upstream of the reservoir fill area was calculated. The erosion rate from the nearest stream gauge or ^{10}Be sample site was then applied to calculate a mass of material eroded annually from the reservoir contributing area, assuming a mean bedrock density of 2650 kg m^{-3}. It was assumed the sediment filling each reservoir has density of 1400 kg m^{-3} by analogy to prior works (Heineke et al., 2017; Snyder et al., 2004), and this value was used to calculate a volume of material added annually to each reservoir. The reservoir volume was divided by this rate to determine a total lifespan. Reservoir lifespans were calculated starting from the day each reservoir was completed to allow for comparisons among the different reservoirs, irrespective of the year each was built. Lifespan calculations also assume, conservatively, that each reservoir contained no sediment when it began operation and that no sediment is removed.

3. Results

3.1. Erosion Rates and Reservoir Infill Rates

Erosion rates as measured by available stream gauge data ranged from 0.0495 mm a^{-1} at the northernmost stream gauge station to 0.354 mm a^{-1} at 33 °S (Table 1). The overall pattern of erosion rates from ^{10}Be samples was similar, ranging from 0.00381 mm a^{-1} in the north to 0.287 mm a^{-1} at 32 °S (Table 2). Overall, the highest erosion rates tended to be clustered together from approximately 32.5 to 35 °S, around the transition area from flat-slab subduction (Figure 3). Most erosion rates from stream gauge stations and ^{10}Be samples located near one another were within error. Two notable exceptions, however, were the Río Tunuyan, in the region where erosion rates are highest, and the Río Atuel, towards the south of the study area. The broad pattern of erosion rates from this study are in reasonable agreement with recalculated catchment-averaged ^{10}Be erosion rates from Val et al. (2018) and Pepin et al. (2013) (Figure 3), which also show higher erosion rates in the transition zone from flat-slab subduction.

Reservoir lifespans from stream gauge data ranged from as low as 76 years from the day of completion for the Carrizal reservoir on the Río Tunuyan to 459 years from the day of completion for the Nihuil reservoir on the Río Atuel. Reservoir lifespans from ^{10}Be sample data occupied a much narrower range, from 129 years for the Carrizal reservoir to 217 years for the Agua del Toro reservoir on the Río Diamante. Notably, the estimated lifespan using ^{10}Be was within 55 years of the estimated lifespan from gauge data for three out of the five reservoirs analyzed, although estimates using the two methods differed considerably for the Río Atuel and Río Diamante (Table 3).

3.2. Paired ^{14}C-^{10}Be Samples

^{10}Be concentrations for the five paired ^{14}C-^{10}Be samples ranged from 61,334 ± 1,180 atoms g^{-1} to 302,702 ± 3,360 atoms g^{-1}. ^{14}C concentrations for these same pairs ranged from 45,094 ± 4,580 atoms g^{-1} to 122,878 ± 10,300 atoms gm^{-1}, with ^{14}C to ^{10}Be ratios for each pair ranging from 0.41 to 1.2 (Table 2). These ratios are well below what would be expected from the simple case of steady-state erosion, placing each sample pair solidly within the “complex exposure” zone of the frequently used two-nuclide diagram (Figure 4; Gosse & Phillips, 2001; Lal, 1991). Assuming that ^{10}Be concentrations are representative of background erosion rates, ^{14}C concentrations would need to be 2.5 to nearly 4 times higher than those actually measured to reflect steady-state erosion.

^{10}Be integration times, or the time it takes to erode a layer of one cosmic ray absorption depth (von Blanckenburg et al., 2005), ranged from approximately 2,000 to 10,000 years for the five sample pairs, assuming an adsorption depth of 60 cm. The three southernmost sample pairs, MDZ17RM2, MDZ17RT2, and MDZ17RA had the lowest integration times, and all were under 3,000 years. The SJ17RB sample had a slightly longer integration time of approximately 4,000 years. The longest integration time, approximately 10,000 years, corresponded to the northernmost sample pair, SJ17RSJt, where erosion rates were lower.

4. Discussion

4.1. Suitability of ^{10}Be for Estimating Reservoir Lifespans

The relative agreement between catchment-averaged erosion rates from ^{10}Be and stream gauge data in this study suggests that in most cases in the Argentine high Andes, ^{10}Be can serve as a reasonable estimator of sediment flux at a given sample site. Both ^{10}Be and stream gauge data also provide relatively close agreement with known sediment accumulation in the Carrizal reservoir on the Río Tunuyán. Based on infill rates from 1971 to 2013 (EVARSA, 2013), it could be expected that it would take approximately 140 years to completely fill the Carrizal reservoir. The ^{10}Be estimate was a very close 129 years while stream gauge data suggested an even shorter lifespan of 79 years. ^{10}Be is also advantageous because it can provide a better estimate of long-term erosion rates than gauge data alone, since it is less sensitive to short-duration, high magnitude events (Heineke, 2017; Niemi et al., 2005). Of course, however, knowledge about the prevalence of such outlier events is still important for the purposes of planning infrastructure projects, as a single such event can rapidly diminish infrastructure function.

Some additional points of caution should be noted about estimating sediment flux from ^{10}Be alone. In one study in the mountains of central Idaho, for example, erosion rates from ^{10}Be were on average 17 time higher than modern erosion rates calculated from gauge data (Kirchner et al., 2001). Additionally, while most locations in this study exhibited agreement between ^{10}Be and stream gauge erosion rates, a notable exception was the Río Atuel, the southernmost site. Here, ^{10}Be data implied a reservoir fill time of 193 years, while stream gauge data implied a dramatically longer 459 years (Table 3). The difficulty with sediment flux estimates at this site may be the location of the reservoir itself, sited tens of kilometers away from the mountain front. In the mountains, stream channels are comparatively confined and occupy steeper slopes. The gradient flattens in the foreland piedmont and stream systems are often characterized by alluvial channels and fan complexes (Capaldi et al., 2019; Pepin et al., 2013; Mehl & Zárate, 2012). While erosion rates calculated from stream gauges on the Río Atuel located at two ends of the piedmont floodplain show strong agreement with one another (Table 1), channel dynamics in the piedmont may simply be more variable over the integration time of ^{10}Be (Mehl & Zárate, 2012). In contrast, ^{10}Be erosion rates from two sites separated by a floodplain on the Río Tunuyán tell a different story. Here, erosion rates calculated from both ^{10}Be and a stream gauge near the exit of the mountain front are higher than the erosion rate calculated from ^{10}Be tens of kilometers away on the piedmont (Table 1, Table 2). In this case, high flow events, such as those associated with warm season snowmelt (Crespo et al., 2020), may be mobilizing sediment in the high Andes that is subsequently decanted onto lowland floodplains (Pepin et al., 2013).

Although the foregoing considerations will need to be kept in mind when interpreting ^{10}Be results to estimate sediment fluxes at timescales relevant to human needs, a notable result from this study is the relative similarity in reservoir lifespans predicted by ^{10}Be. These were all within 90 years of one another and did not exceed 217 years, with shorter lifespans predicted in the region from 32.5 to 34° S. These estimates are also conservative, as a reservoir will almost certainly cease to be functionally useful before it is completely filled with sediment, assuming sediment is not removed. While paired ^{10}Be and stream gauge estimates may be the most useful for predicting reservoir lifespans (Heineke, 2017), these results suggest that ^{10}Be alone may provide a useful first approximation where existing monitoring efforts do not exist.

4.2 Sediment Transport Implications from Hillslope to Catchment Outlet from ^{14}C and ^{10}Be

Lower than expected ^{14}C to ^{10}Be ratios have been observed in other studies where ^{10}Be has been used to measure catchment-averaged erosion rates (Kober et al., 2019; Hippe et al., 2012).

While integration times of 2,000 to 10,000 years for the five paired ^{10}Be samples suggest that these sediments were eroded from catchment hillslopes during the Holocene, the low ^{14}C concentrations indicate that this may not have been the case. The broad similarity of the ^{10}Be and stream gauge results for most catchments suggests that the ^{10}Be erosion rates are representative of background erosion in the catchments. Assuming steady-state erosion based on the ^{10}Be sample concentrations, it would take approximately 10,000 to 19,000 years of complete shielding to reduce the ^{14}C concentrations to their observed values. This amount of time indicates that an assumption of nearly uninterrupted travel through the watershed from hillslope to catchment outlet is not met, at least on the timescale of ^{14}C (von Blanckenurg, 2005; Granger et al., 1996). Due to its much larger half-life, however, ^{10}Be concentrations would be minimally impacted over this timescale, and for practical purposes are largely insensitive to hillslope processes occurring outside the buildup of initial concentrations in the regolith.

Several studies attribute low ^{14}C concentrations relative to ^{10}Be concentrations to sediment storage (Kober et al., 2019; Kim et al., 2016; Hippe et al., 2012). As a practical matter, pinpointing the exact mechanism of storage in a given watershed has proven difficult (Hippe et al., 2019). In the high Andes, many potential mechanisms for transient storage existed during the Holocene and late Pleistocene, although many of the finer details of the landscape during these epochs are still unknown. Glacier equilibrium line elevations were several hundred meters lower during the Last Glacial Maximum compared to today, although glaciers would not have covered the entire watersheds analyzed in this study (Clapperton, 1994). Potential Neoglacial advances during the Holocene (Mehl & Zárate, 2012; Espizua, 2005) could also shield sediments for a few thousand years, but are not likely a sufficient explanation for the reduced ^{14}C concentrations alone.

Postglacial moraines and hanging valleys are other locations where sediment could be transiently stored (Pepin et al., 2013) in addition to alluvium along stream banks.

Among the five paired ^{14}C-^{10}Be samples, the northernmost sample, located on the Río San Juan, is in a location where extensive upstream sediment storage is most likely to have occurred and had the lowest ^{14}C/^{10}Be ratio in this study (0.41). This sample was collected downstream from the large Calingasta Valley, which is traversed by several tributaries of the Río San Juan draining the high Andes to the west. This location is likely comparable to the piedmont traversed by the Río Tunuyán, where sediment-laden streamflow from the mountains may be partially decanted onto floodplains during high flow events. ^{10}Be erosion rates from this study further suggest that this is the case. The erosion rate measured on the Río Blanco, a Rio San Juan tributary upstream from the Calingasta Valley, is more than twice as high as that measured on the Rio San Juan on the downstream side of the valley (Table 2). As discussed previously, ^{10}Be erosion rates on the Río Tunuyan show a similar dynamic: the erosion rate measured where the Tunuyán exists the mountain front is over 1.5 times the erosion rate measured downstream after the Tunuyán has traversed the piedmont floodplain for tens of kilometers. Both of these sample pairs indicate that the possibility for sediment storage is high when rivers exit the mountains and cross broad, low-lying areas.

In contrast to the Río San Juan sample, the majority of the paired ^{14}C-^{10}Be samples principally drain high mountain catchments with narrow channels – topography that is not conducive to extensive storage (Marshall et al., 2017). Slopes in these catchments are steep, averaging 19-27° for the four remaining paired ^{14}C-^{10}Be sample sites. Based on aerial imagery, it is estimated that only approximately 6-10% of the contributing areas for these same four samples consist of the types of terrain where long-term storage is typically thought to occur, namely, moraines, hanging valleys, and stream bank alluvium (Pepin et al., 2013). For these areas of storage to be the primary explanation for reduced $^{14}C/^{10}Be$ ratios, 85 to 95% of sediment exiting the catchments would have to be sourced from them, which is unlikely given their comparatively small size.

While transient storage in moraines or alluvium and temporary shielding by glacier or snow cover may be the cause of some reduction in ^{14}C concentrations relative to ^{10}Be, other processes are likely necessary to account for the ratios observed in this study. Since most of the catchments are characterized by steep hillslopes, a significant amount of shielding may occur on the hillslopes themselves. Scree and talus mantled hillslopes are pervasive throughout the high Andes. These are dynamic environments, where sediment from upper elevations can be transiently stored and reworked by processes including landsliding and snow coverage (Hendrickx et al., 2020; Sass, 2006). Sediments on these slopes can also be mixed from periglacial processes such as frost cracking (Marshall et al., 2017), which could have occurred at a higher rate following glacial episodes (Marshall et al., 2015). In this type of setting, it may actually be difficult for sediment eroded from bedrock at upper elevations from ridgelines or rock walls to stay at the slope surface, and some form of shallow to intermediate shielding may be common. It is therefore proposed that reduced ^{14}C concentrations can be at least partially attributed to transient sediment storage in talus slopes in addition to the processes previously described.

One other noteworthy observation from the paired ^{14}C-^{10}Be samples is the closeness of their ratios. While the Río San Juan sample had the lowest $^{14}C/^{10}Be$ ratio of 0.41, none where higher than 1.2. This result suggests that whatever the exact cause of the reduced ^{14}C concentrations, similar processes likely impacted each of the catchments, even though they span several degrees of latitude and variable amounts of glacier coverage (Figure 1). The similar ratios and the topography characteristic of the high Andes also make some explanations for reduced ^{14}C

concentrations in other regions less likely here. For instance, a significant reworking of the fluvial network in each of the catchments is unlikely, especially given the steep hillslopes surrounding modern channels (Hippe et al., 2019). Ultimately, however, more research will be needed to constrain the processes impacting ^{14}C concentrations in this region. Paired ^{14}C-^{10}Be samples from sediment source areas could be particularly insightful (Kober et al., 2019).

Aside from the exact mechanisms leading to reduced ^{14}C concentrations in the high Andes, the paired ^{14}C/^{10}Be ratios in this study are also informative because they suggest a minimum transport time through the sediment cascade from hillslope to catchment outlet. Based on this reading, ^{10}Be integration times indicate travel times through the regolith to surface exposure, reduced ^{14}C concentrations from steady-state suggest a minimum travel time through the catchment, and gauge data indicates the modern sediment flux leaving the catchment. The closeness of the ^{10}Be and gauge results give more confidence to this interpretation, as erosion rates appear comparatively steady over these differing intervals, although short term changes in erosion rates cannot be ruled out. If correct, this hypothesis implies that fluvial sediment at the catchment outlets could have been eroded from higher elevation hillslopes during the early Holocene or late Pleistocene. Any intervals of re-exposure between periods of shielding would necessarily increase this timeframe.

5. Conclusion

Stream gauge data and cosmogenic ^{10}Be were used to quantify catchment scale erosion rates from six active rivers in the Argentine high Andes. For most catchments, ^{10}Be and stream gauge results are in broad agreement and mirror a trend showing the highest erosion rates between 32.5 to 35° S, around the transition zone from flat slab subduction of the Nazca plate. ^{10}Be results also predict lifespans for five reservoirs at the foot of the high Andes ranging from 129 to 217 years, with more variability seen in lifespans calculated from gauge data. The broad similarity of ^{10}Be and stream gauge results gives strength to the conclusion that ^{10}Be erosion rates are representative of background erosion in the region. Low concentrations of ^{14}C relative to ^{10}Be, however, indicate that sediment travel times through these complex, postglacial catchments may range from a minimum of 7,500 to 11,000 years, although additional work will be needed to confirm this hypothesis.

Acknowledgements

This work was supported by the National Science Foundation under Grant DGE-1449617, the Geological Society of America John T. and Carol G. McGill Award, the Syracuse University Education Model Program on Water-Energy Research (EMPOWER), and the Syracuse University Research Excellence Doctoral Funding (REDF) program.

Figures

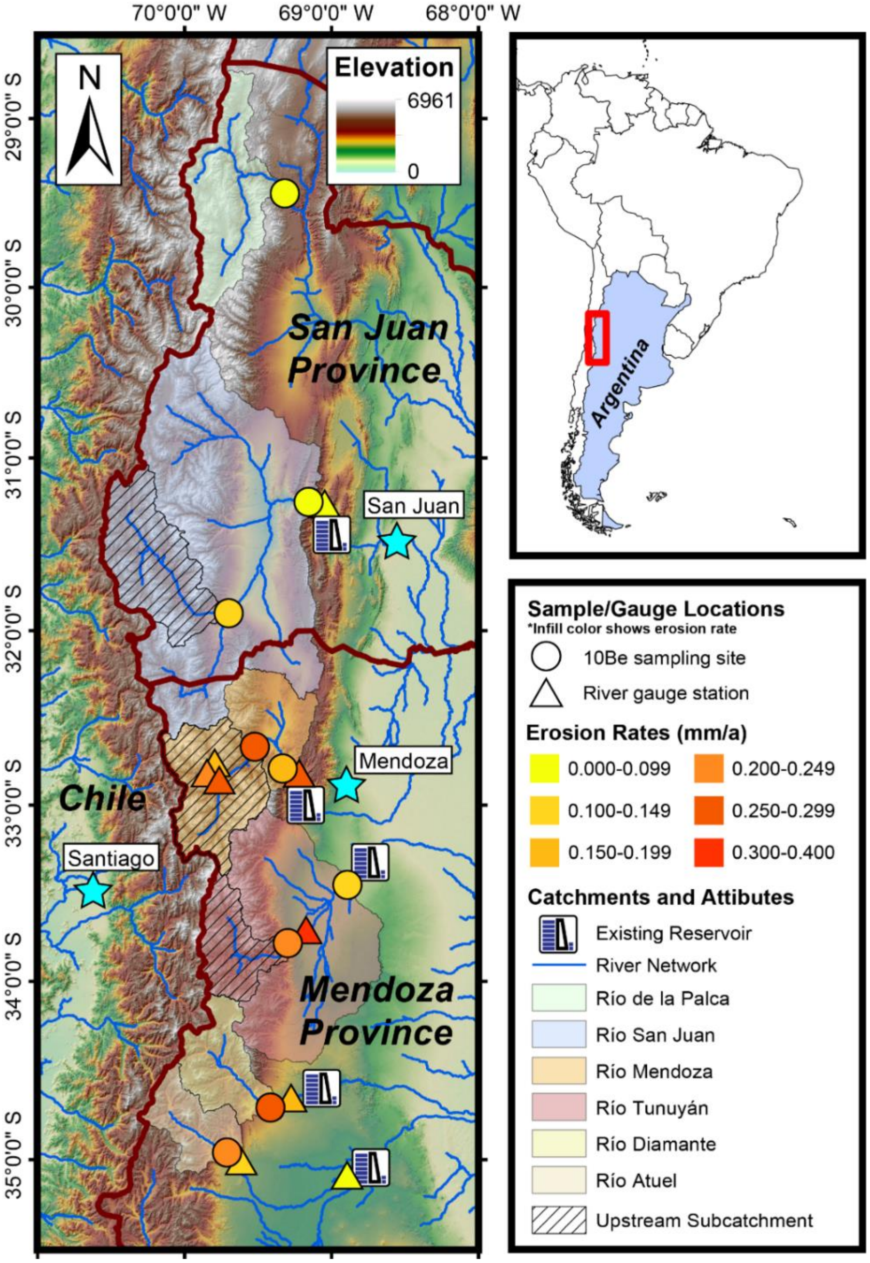

Figure 1. Map of the study area, ^{10}Be nuclide sample locations, river gauge stations, and existing reservoirs immediately downstream of sample locations in the Argentine high Andes. ^{10}Be Sample sites and gauged stations are shaded according to measured erosion rates in this study. Contributing areas for sample location are also shaded. Map of South America shows the extent of the study area in Argentina.

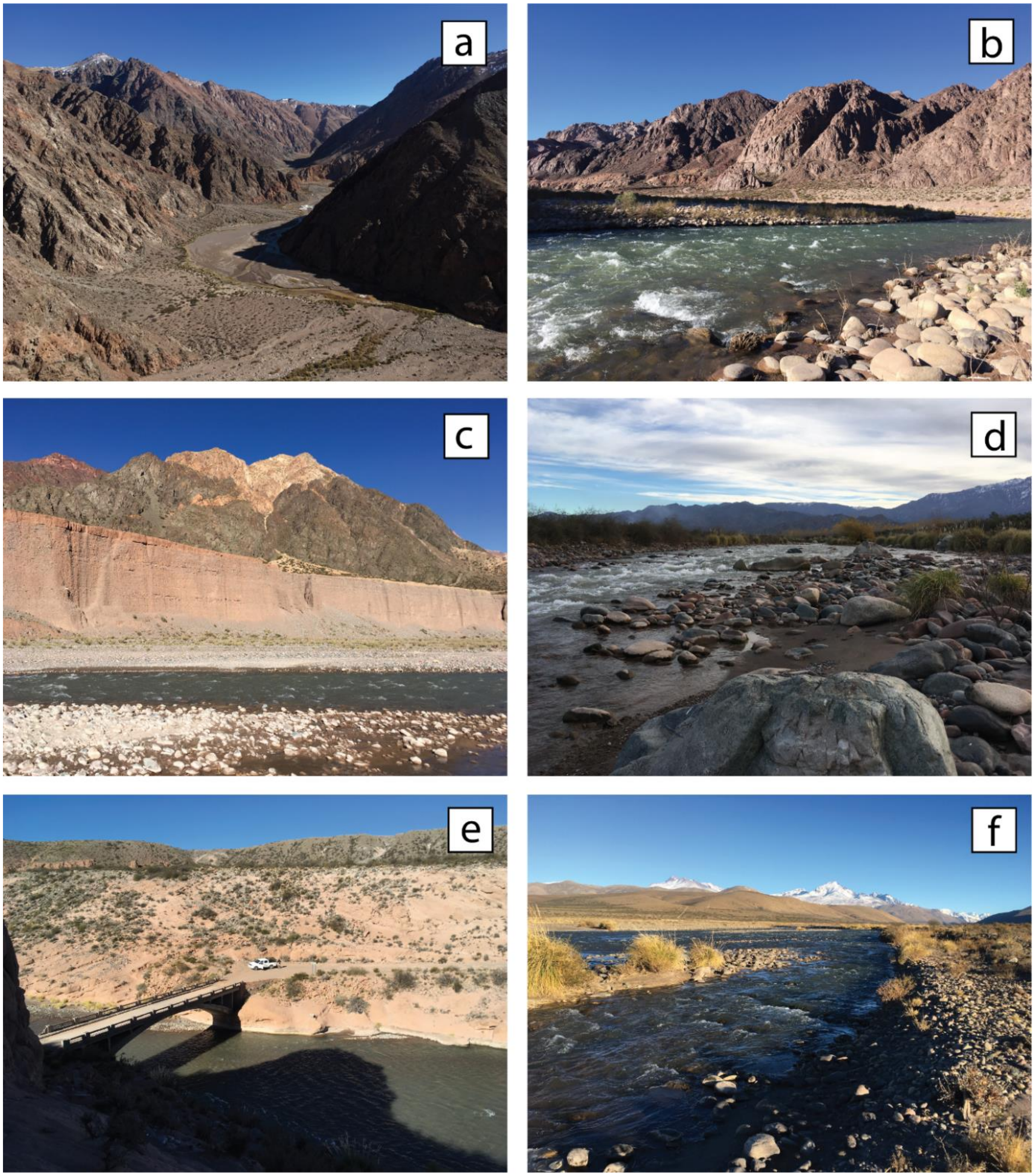

Figure 2. June 2017 field photos of the following cosmogenic nuclide sample locations (sample ID in parentheses), arranged in order from north to south: *a*. Río de la Palca (SJ17RPa), *b*. Río Blanco (SJ17RB), *c*. Río Mendoza (MDZ17RM2), *d*. Río Tunuyan (MDZ17RT2), *e*. Río Diamante (MDZ17RD), and *f*. Río Atuel (MDZ17RA).

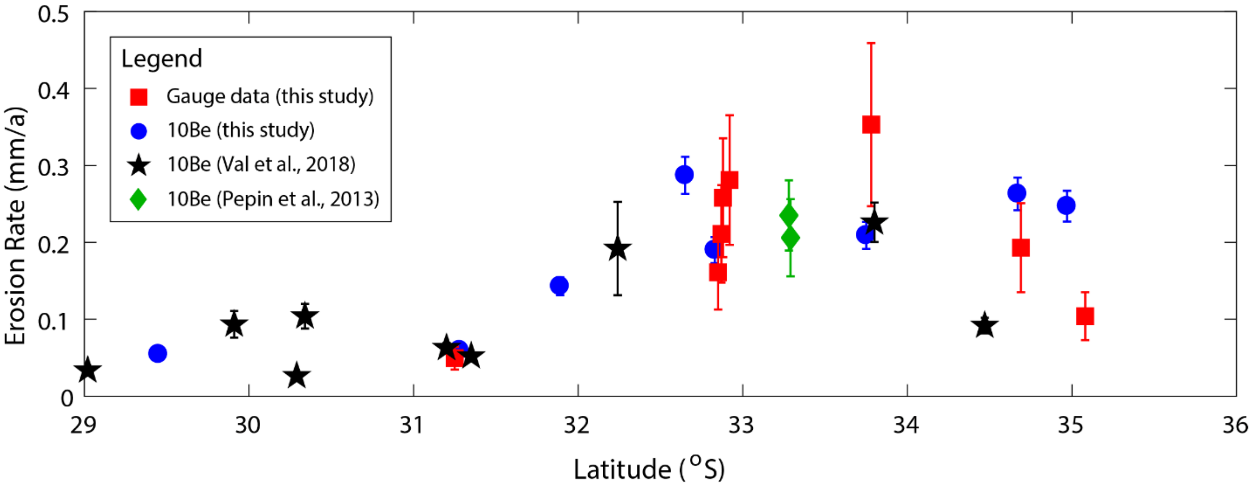

Figure 3. Erosion rates from gauge data and ^{10}Be in this study and recalculated ^{10}Be erosion rates from samples collected in Val et al. (2018) and Pepin et al. (2013). All samples are from the Argentine Andes between 29 and 36° S, including both the Precordillera and high Andes. Only those samples within the Andes or in close proximity to the mountain front are shown. Erosion rates are highest from approximately 32.5 to 35° S.

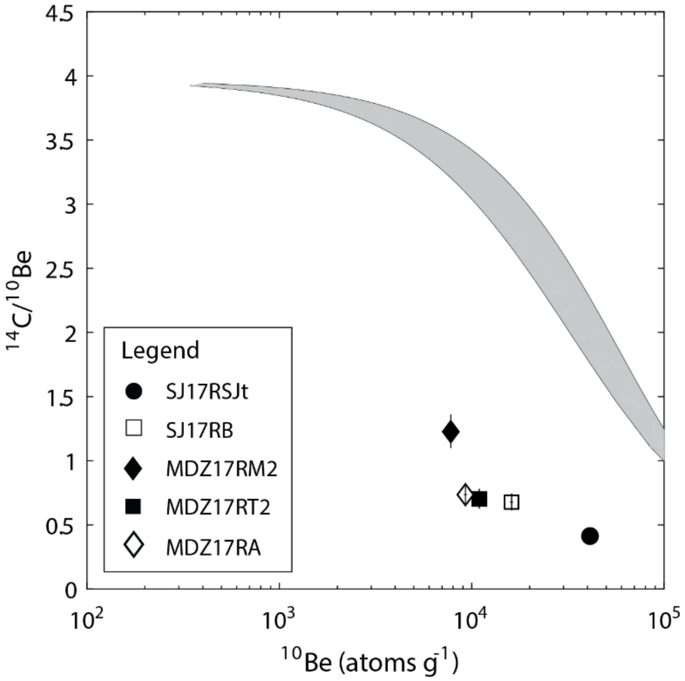

Figure 4. Two-nuclide diagram showing ^{14}C to ^{10}Be ratio for five paired ^{14}C-^{10}Be samples versus ^{10}Be concentrations, adjusted to sea level and high latitude. Note that all samples plot outside the shaded gray steady-state island and are located within the complex exposure area of the diagram (Gosse & Phillips, 2001; Lal, 1991).

Tables

Table 1. Stream gauge stations and calculated erosion rates.

River	Gauge Location	Gauge Number	Latitude (°S)	Longitude (°W)	Contributing Area (km^2)	Erosion Rate (mm/a)	Uncertainty (mm/a)
San Juan	KM 101	1211	31.25	69.18	23862	0.0495	0.0148
Vacas	Punta de Vacas	1421	32.85	69.76	563	0.161	0.0484
Cuevas	Punta de Vacas	1407	32.87	69.77	669	0.211	0.0634
Tupungato	Punta de Vacas	1420	32.88	69.77	1767	0.258	0.0773
Mendoza	Guido	1413	32.9153	69.2378	7155	0.281	0.0843
Tunuyán	Uco Valley	1419	33.7765	69.2725	2458	0.353	0.106
Diamante	La Jaula	1423	34.6685	69.2725	2832	0.193	0.0579
Atuel	El Sosneado	1428	35.0839	69.6031	2364	0.104	0.0312
Atuel	La Angostura	1403	35.10	68.87	3009	0.0956	0.0287

Table 2. ^{10}Be sample data, corresponding erosion rates (E), and ^{14}C sample data. Mean catchment elevation is calculated by excluding non-quartz lithologies and weighted based on catchment hypsometry. Uncertainty (±) reported as the combination of internal and external uncertainty.

River	**Sample**	**Latitude (°S)**	**Longitude (°W)**	**Mean Elev. (m)**	**Contrib. Area (km^2)**	**^{10}Be (atoms/g)**	**^{10}Be ± (atoms/g)**	**^{10}Be E (mm/a)**	**^{10}Be E ± (mm/a)**	**^{14}C (atoms/g)**	**^{14}C ± (atoms/g)**	**^{14}C/^{10}Be**
de la Palca	SJ17RPa	29.4456	69.3250	4201	5521	539861	5230	0.0546	0.00381	-	-	-
San Juan	SJ17RSJt	31.2844	69.1006	3191	23948	302702	3360	0.0598	0.00428	122878	10340	0.406
Blanco	SJ17RB	31.8947	69.6967	3684	4856	154936	2880	0.143	0.0115	104960	8140	0.677
Mendoza	MDZ17RM1	32.8342	69.2831	3498	6975	103610	2530	0.190	0.0169	-	-	-
Mendoza	MDZ17RM2	32.6533	69.5033	3957	4226	82929	1770	0.287	0.0241	101694	8690	1.23
Tunuyán	MDZ17RT1	33.4325	68.8714	2230	12283	81234	2340	0.125	0.0119	-	-	-
Tunuyán	MDZ17RT2	33.7506	69.1980	3558	2534	94483	1990	0.209	0.0175	66320	5900	0.702
Diamante	MDZ17RD	34.6692	69.3172	2919	2784	58802	1000	0.263	0.0213	-	-	-
Atuel	MDZ17RA	34.9733	69.6706	2879	2117	61334	1180	0.247	0.0201	45093	4580	0.735

Table 3. Location and volume of reservoirs in the Mendoza and San Juan provinces located downstream of river gauge stations and ^{10}Be sample sites. Reservoir volume from Carmona *et al* (2014), ORSEP (2021), and Panedile (2021). The lifespan of each reservoir is calculated using both stream gauge and ^{10}Be data. As described in the methods, erosion rates from the Uco Valley gauge station and the MDZ17RA ^{10}Be sample site were scaled for calculation of reservoir lifespans due to distance from their respective reservoir locations.

Reservoir	**River**	**Lat (°S)**	**Lon (°S)**	**Volume (hm^3)**	**Upstream Gauge**	**Upstream ^{10}Be Sample**	**Est. lifespan from gauge (yrs)**	**Est. lifespan from ^{10}Be (yrs)**
Los Caracoles	San Juan	33.52	68.98	565	KM 101	SJ17RSJt	246	204
Potrerillos	Mendoza	32.99	69.13	420	Guido	MDZ17RM1	106	157
El Carrizal	Tunuyan	33.29	68.72	390	Uco Valley*	MDZ17RT1	76	129
Agua del Toro	Diamante	34.58	69.04	325	La Jaula	MDZ17RD	296	217
El Nihuil	Atuel	35.03	68.68	259	La Angostura	MDZ17RA*	459	193

Supplementary Information

Table S1. Stream gauge sediment and streamflow years of observation and number of observations at each site.

			Sediment Data		Streamflow Data	
River	**Gauge Location**	**Gauge Number**	**Years Covered**	**Number of Observations**	**Years Covered**	**Number of Observations**
San Juan	KM 101	1211	2010-2020	142	1971-2019	14182
Vacas	Punta de Vacas	1421	1999-2020	396	1949-2020	25080
Cuevas	Punta de Vacas	1407	1999-2020	402	1949-2020	24647
Tupungato	Punta de Vacas	1420	1999-2020	399	1949-2020	24767
Mendoza	Guido	1413	1999-2020	441	1956-2019	22098
Tunuyán	Uco Valley	1419	1999-2020	439	1954-2019	23795
Diamante	La Jaula	1423	1999-2020	432	1971-2019	17581
Atuel	El Sosneado	1428	1999-2020	388	1972-2019	16885
Atuel	La Angostura	1403	1999-2020	451	1931-2020	32306

Table S2. ^{10}Be AMS results.

Sample ID	Be ratio	Be ratio error	Error (%)	Carrier conc. (ppm)	Carrier weight (g)	Quartz (g)	Grams of ^{9}Be	^{9}Be atoms	^{10}Be atoms	^{10}Be (atoms/g)	± (atoms/g)
MDZ17RT1	2.719E-13	7.84E-15	2.9%	372.5	0.6070	50.5665	0.000226108	1.5109E+19	4.11E+06	8.12E+04	2.34E+03
MDZ17RD	1.643E-13	3.09E-15	1.9%	372.5	0.6065	42.1869	0.000225921	1.5097E+19	2.48E+06	5.88E+04	1.10E+03
MDZ17RT2	3.375E-13	7.11E-15	2.1%	372.5	0.6079	54.0536	0.000226443	1.5131E+19	5.11E+06	9.45E+04	1.99E+03
SJ17RB	5.356E-13	9.96E-15	1.9%	372.5	0.6069	52.2173	0.000226070	1.5106E+19	8.09E+06	1.55E+05	2.88E+03
SJ17RPa	1.331E-12	1.29E-14	1.0%	372.5	0.6087	37.3648	0.000226741	1.5151E+19	2.02E+07	5.40E+05	5.23E+03
SJ17RSJt	1.429E-12	1.59E-14	1.1%	372.5	0.6072	71.3488	0.000226182	1.5114E+19	2.16E+07	3.03E+05	3.36E+03
MDZ17RM1	3.872E-13	9.45E-15	2.4%	372.5	0.6066	56.4227	0.000225959	1.5099E+19	5.85E+06	1.04E+05	2.53E+03
MDZ17RM2	1.636E-13	3.50E-15	2.1%	372.5	0.6071	29.8069	0.000226145	1.5111E+19	2.47E+06	8.29E+04	1.77E+03
MDZ17RA	1.022E-13	1.96E-15	1.9%	372.5	0.6076	25.2125	0.000226331	1.5124E+19	1.55E+06	6.13E+04	1.18E+03

Table S3. ^{10}Be inputs to Balco *et al* (2008) online cosmogenic nuclide calculator version 3.0 for samples collected as part of this study. The nuclide-mineral pair for each sample was entered as “Be-10” and “quartz.”

Sample Name	**Lat (°S)**	**Lon (°W)**	**Elevation (m)**	**Elevation / Pressure Flag**	**Sample Thickness (cm)**	**Sample Density (g cm^{-3})**	**Shielding correction**	**Year**	**^{10}Be concentration (atoms g^{-1})**	**^{10}Be uncertainty (atoms gm^{-1})**	**10-Be Standardization**
SJ17RPa	29.45	69.33	4201	std	0	2.65	0.98	2017	539861	5228	07KNSTD
SJ17RSJt	31.28	69.10	3191	std	0	2.65	0.98	2017	302702	3360	07KNSTD
SJ17RB	31.89	69.70	3684	std	0	2.65	0.97	2017	154936	2881	07KNSTD
MDZ17RM1	32.83	69.28	3498	std	0	2.65	0.94	2017	103610	2529	07KNSTD
MDZ17RM2	32.65	69.50	3957	std	0	2.65	0.91	2017	82929	1774	07KNSTD
MDZ17RT1	33.43	68.87	2230	std	0	2.65	0.97	2017	81234	2342	07KNSTD
MDZ17RT2	33.75	69.20	3558	std	0	2.65	0.88	2017	94483	1991	07KNSTD
MDZ17RD	34.67	69.32	2919	std	0	2.65	0.97	2017	58802	1105	07KNSTD
MDZ17RA	34.97	69.67	2879	std	0	2.65	0.96	2017	61334	1178	07KNSTD

Table S4. ^{10}Be inputs to Balco et al. (2008) online cosmogenic nuclide calculator version 3.0 for sample data from Val et al. (2018) (PV, AL prefixes) and Pepin et al. (2013) (CLA prefixes). The nuclide-mineral pair for each sample was entered as "Be-10" and "quartz." A sample density of 2.65 g cm^{-3} was used for consistency with the analysis of other samples in this study. For samples from Pepin et al. (2013), 2011 was entered as year of sample collection as an estimate based on year of study publication. Mean sample elevations were also recalculated for the two samples from Pepin, et al. (2013) in ArcGIS.

Sample Name	**Lat (°S)**	**Lon (°W)**	**Elevation (m)**	**Elevation / Pressure Flag**	**Sample Thickness (cm)**	**Sample Density (g cm^{-3})**	**Year**	**Shielding correction**	**^{10}Be concentration (atoms g^{-1})**	**^{10}Be uncertainty (atoms gm^{-1})**	**^{10}Be Standardization**
PV-14-30	29.02	69.37	3980	std	0	2.65	2014	0.94	769921	15632	07KNSTD
PV-14-24	29.91	68.72	2070	std	0	2.65	2014	0.94	87332	7250	07KNSTD
PV-14-23	30.34	69.01	2460	std	0	2.65	2014	0.99	103515	6705	07KNSTD
PV-14-11	30.29	69.67	3930	std	0	2.65	2014	0.96	1030780	20109	07KNSTD
PV-14-15	31.20	69.04	2320	std	0	2.65	2014	0.96	164613	5092	07KNSTD
PV-14-16	31.35	69.88	3700	std	0	2.65	2014	0.90	427304	9918	07KNSTD
A13-07	32.24	69.95	3610	std	0	2.65	2013	0.90	98730	14983	07KNSTD
PV-14-14	33.80	69.67	3580	std	0	2.65	2013	0.89	85727	3544	07KNSTD
A13-05	34.47	69.72	2890	std	0	2.65	2014	0.92	163478	6362	07KNSTD
CLA2	33.28	69.55	4030*	std	0	2.65	2011*	1.0	114000	10000	07KNSTD
CLA4	33.29	69.48	3881*	std	0	2.65	2011*	1.0	122000	14000	07KNSTD

Table S5. Recalculated erosion rates for Val et al. (2018) (PV, Al prefixes) and Pepin et al. (2013) (CLA prefixes) ^{10}Be samples using version 3.0 of the Balco *et al* (2008) online cosmogenic nuclide calculator and LSD scaling.

Sample Name	Erosion Rate (mm/a)	Internal Uncertainty (mm/a)	External Uncertainty (mm/a)
PV-14-30	0.0337	0.000691	0.00212
PV-14-24	0.0934	0.00778	0.00954
PV-14-23	0.104	0.00679	0.00918
PV-14-11	0.0264	0.000520	0.00166
PV-14-15	0.0629	0.00196	0.00421
PV-14-16	0.0521	0.00122	0.00322
A13-07	0.192	0.0293	0.0314
PV-14-14	0.226	0.00937	0.0163
A13-05	0.0919	0.00359	0.00652
CLA2	0.235	0.0207	0.0249
CLA4	0.206	0.0236	0.0266

References

Balco, G., Stone, J.O., Lifton, N.A., & Dunai, T.J. 2008. A complete and easily accessible means of calculating surface exposure ages or erosion rates from ^{10}Be and ^{26}Al measurements. *Quaternary Geochronology*, 3: 174-195. https://doi.org/10.1016/j.quageo.2007.12.001

Barros, V.R., Boninsegna, J.A., Camilloni, I.A., Chidiak, M., Magrín, G.O., & Rusticucci, M. 2015. Climate change in Argentina: trends, projections, impacts and adaptation. *WIREs Climate Change*, 6: 151-169. https://doi.org/10.1002/wcc.316

BDHI. 2021. Base de Datos Hidrilógica Integrada. http://bdhi.hidricosargentina.gob.ar.

Bierman, P.R. 1994. Using in situ produced cosmogenic isotopes to estimate rates of landscape evolution: A review from the geomorphic perspective. *Journal of Geophysical Research*, 99: 13,885-13,896. https://doi.org/10.1029/94JB00459

Cahill, T. & Isacks, B.L. 1992. Seismicity and shape of the subducted Nazca Plate. *Journal of Geophysical Researc*h, 917(B12) 17,503-17,529. https://doi.org/10.1029/92JB00493

Capaldi, T.N., George, S.W.M., Hirtz, J.A., Horton, B.K., & Stockli, D.F. Fluvial and eolian sediment mixing during changing climate conditions recorded in Holocene Andean foreland deposits from Argentina (31-33° S). *Frontiers in Earth Science*, 7: 298. https://doi.org/10.3389/feart.2019.00298

Carmona, J.S., Carmona Palau, J., & Palau, R. 2014. The Evaluation of the Permanent Seismic Crest Displacement of the CFGD Potrerillos Dam in Argentine by Means of a Tridemensional Limit State Analysis. 13th World Conference on Earthquake Engineering, Paper No. 487. 12p.

Carretier, S., Regard, V., Vassallo, R., Aguilar, G., Martinod, J., Riquelme, R., Pepin, E., & Charrier, R., et al. 2013. Slope and climate variability control of erosion in the Andes of central Chile. *Geology*, 41(2): 195-198. https://doi.org/10.1130/G33735.1

Clapperton, C.M. 1994. The quaternary glaciation of Chile: a review. *Revista Chilena de Historia Natural*, 67: 369-383.

Crespo, S.A., Fernandoy, F., Cara, L., Klarian, S., & Lavergne, C. 2020. First snow, glacier and groundwater contribution quantification in the upper Mendoza River basin using stable water isotopes. *Isotopes in Environmental and Health Studies*, 56(5-6): 566-585. https://doi.org/10.1080/10256016.2020.1797713

Dunne, J., Elmore, D., & Muzikar, P. 1999. Scaling factors for the rates of production of cosmogenic nuclides for geometric shielding and attenuation at depth on sloped surfaces. *Geomorphology*, 27: 3-11. https://doi.org/10.1016/S0169-555X(98)00086-5

Espizua, L.E. 2005. Holocene glacier chronology of Valenzuela Valley, Mendoza Andes, Argentina. *The Holocene*, 15(7): 1079-1085. https://doi.org/10.1191/0959683605hl866rr

Evaluación de Recursos S.A. (EVARSA). 2013. Batimetria Embalse El Carrizal. 37p.

Gao, P. 2008. Understanding watershed suspended sediment transport. *Progress in Physical Geography*, 32(3): 243-263. https://doi.org/10.1177/0309133308094849

Gosse, J.C. & Phillips, F.M. 2001. Terrestrial in situ cosmogenic nuclides: theory and application. *Quaternary Science Reviews*, 20: 1475-1560. https://doi.org/10.1016/S0277-3791(00)00171-2

Graham, B.L., Briner, J.P., Schweinsberg, A.D., Lifton, N.A., & Bennike, O. 2019. New in situ ^{14}C data indicate the absence of nunataks in west Greenland during the Last Glacial Maximum. *Quaternary Science Reviews*, 225: 105981. https://doi.org/10.1016/j.quascirev.2019.105981

Granger, D.E., Kirchner, J.W., & Finkel, R. 1996. Spatially Averaged Long-Term Erosion Rates Measured from In-Situ Produced Cosmogenic Nuclides in Alluvial Sediment. *The Journal of Geology*, 104: 249-257. http://www.jstor.org/stable/30068190

Heineke, C., Hetzel, R., Akal, C., & Christl, M. 2017. Constraints on water reservoir lifetimes from catchment-wide ^{10}Be Erosion Rates – A case study from Western Turkey. *Water Resources Research*, 53: 9206-9244. https://doi.org/10.1002/2017WR020594

Hippe, K., Kober, F., Zeilinger, G., Ivy-Ochs, S., Maden, C., Wacker, L., Kubik, P.W., & Wieler, R. 2012. Quantifying denudation rates and sediment storage on the eastern Antiplano, Bolivia, using cosmogenic ^{10}Be, ^{26}Al, and in situ ^{14}C. *Geomorphology,* 179: 58-70. https://doi.org/10.1016/j.geomorph.2012.07.031

Hippe, K., Gordijn, T., Picotti, V., Hajdas, I., Jansen, J.D., Christl, M., et al. 2019. Fluvial dynamics and ^{14}C-^{10}Be disequilibrium on the Bolivian Antiplano. *Earth Surface Processes and Landforms*, 44: 766-780. https://doi.org/10.1002/esp.4529

Hendrickx, H., De Sloover, L., Stal, C., Delaloye, R., Nyssen, J, & Frankl, A. 2020. Talus slope geomorphology investigated at multiple time scales from high-resolution topographic surveys and historical aerial photographs (Sanetsch Pass, Switzerland). *Earth Surface Processes and Landforms*, 45: 3653-3669. https://doi-org.libezproxy2.syr.edu/10.1002/esp.4989

Hoke, G.D., Graber, N.R., Mescua, J.F., Giambiagi, L.B., Fitzgerald, P.F., & Metcalf, J.R. 2014. Near pure surface uplift of the Argentine Frontal Cordillera: insights from (U-Th)/He thermochronometry and geomorphic analysis. *Geological Society, London, Special Publications*, 399: 383-399. https://doi.org/10.1144/SP399.4

Kirchner, J.W., Finkel, R.C., Riebe, C.S., Granger, D.E., Clayton, J.L., King, J.G., & Megahan, W.F. 2001. Mountain erosion over 10 yr, 10 k.y., and 10 m.y. time scales. *Geology*, 29(7): 591-594. https://doi.org/10.1130/0091-7613(2001)029<0591:MEOYKY>2.0.CO;2

Kim, D., Seong, Y.B., Byun, J., Weber, J., & Min, K. 2016. Geomorphic disequilibrium in the Eastern Korean Peninsula: possible evidence for reactivation of a rift-flank margin. *Geomorphology*, 254: 130-145. http://dx.doi.org/10.1016/j.geomorph.2015.11.022

Kober, F., Hippe, K., Salcher, B., Grischott, R., Zurfluh, R., Hajdas, I., et al. 2019. Postglacial to Holocene landscape evolution and process rates in steep alpine catchments. *Earth Surface Processes and Landforms,* 44: 242-258. https://doi.org/10.1002/esp.4491

Kornijów, R. 2009. Controversies around dam reservoirs: benefits, costs, and future. *Ecohydrology and Hydrobiology*, 9(2-4): 141-148. https://doi.org/10.2478/v10104-010-0001-4

Lal, D. 1990. Cosmic Ray labeling of erosion surfaces: in situ nuclide production rates and erosion models. *Earth and Planetary Science Letters*, 104: 424-439. https://doi.org/10.1016/0012-821X(91)90220-C

Leiva, J.C., Cabrera, G.A., & Lenzano, L.E. 2007. 20 years of mass balances on the Piloto glacier, Las Cuevas river basin, Mendoza, Argentina. *Global and Planetary Change*, 59: 10-16. https://doi.org/10.1016/j.gloplacha.2006.11.018

Leiva, J.C. 1999. Recent fluctuations of Argentinian glaciers. *Global and Planetary Change*, 22: 169-177. https://doi.org/10.1016/S0921-8181(99)00034-X

Lifton, N., Goehring, B., Wilson, J., Kubley, T., & Caffee, M. 2015. Progress in automated extraction and purification of in situ ^{14}C from quartz: Results from the Purdue in situ ^{14}C laboratory. *Nuclear Instruments and Methods in Physics Research B*, 361: 381-386. https://doi.org/10.1016/j.nimb.2015.03.028

Lifton, N., Sato, T., & Dunai, T.J. 2014. Scaling in situ cosmogenic nuclide production rates using analytical approximations to atmospheric cosmic-ray fluxes. *Earth and Planetary Science Letters*, 386: 149-160. https://doi.org/10.1016/j.epsl.2013.10.052

Marshall, J.A., Roering, J.J., Gavin, D.G., & Granger, D.E. 2017. Late Quaternary climatic controls on erosion rates and geomorphic processes in western Oregon, USA. *Geological Society of America Bulletin*, 129: 715–731. https://doi.org/10.1130/B31509.1

Marshall, J.A., Roering, J.J., Bartlein, P.J., Gavin, D.G., Granger, D.E., Rempel, A.W., Praskievicz, S.J., & Hales, T.C. 2015. Frost for the trees: Did climate increase erosion in unglaciated landscapes during the late Pleistocene? *Science Advances*, 1: e1500715. https://doi.org/10.1126/sciadv.1500715

Masiokas, M.H., Villalba, R., Luckman, B.H., Le Quesne, C. & Aravena, J.C. 2006. Snowpack variations in the Central Andes of Argentina and Chile, 1951-2005: Large-Scale Atmospheric Influences and Implications for Water Resources in the Region. *Journal of Climate*, 19: 6334-6352. https://doi.org/10.1175/JCLI3969.1

Masiokas, M.H., Rivera, A., Espizua, L.E., Villalba, R., Delgado, S., & Aravena, J.C. 2009. Glacier fluctuations in extratropical South America during the past 1000 years. *Paleogeography, Paleoclimatology, Paleoecology*, 281: 242-268. https://doi.org/10.1016/j.palaeo.2009.08.006

Mehl, A.E., & Zárate, M.A. 2012. Late Pleistocene and Holocene environmental and climatic conditions in the eastern Andean piedmont of Mendoza (33°-34° S, Argentina). *Journal of South American Earth Sciences*, 37: 41-59. https://doi.org/10.1016/j.jsames.2012.01.003

Molnar, P., Anderson, R.S., Kier, G., & Rose, J. 2006. Relationships among probability distributions of stream discharges in floods, climate, bed load transport, and river incision. *Journal of Geophysical Research: Earth Surface*, 111: F02001. https://doi.org/10.1029/2005JF000310

Morris, A.S. 1969. The development of the irrigation economy of Mendoza, Argentina. *Annals of the Association of American Geographers*, 59(1): 97-115. https://doi.org/10.1111/j.1467-8306.1969.tb00660.x

Mulcahy, P., Chen, C., Kay, S., Brown, L., Isacks, B., Sandvol, E., et al. Central Andean mantle and crustal seismicity beneath the Southern Puna plateau and the northern margin of the Chilean-Pampean flat slab. *Tectonics,* 33: 1636-1658. https://doi.org.libezproxy2.syr.edu/10.1002/2013TC003393

Niemi, N.A., Oskin, M., Burbank, D.W., Heimsath, A.M., & Gabet, E.J. 2005. Effects of bedrock landslides on cosmogenically determined erosion rates. *Earth and Planetary Science Letters*, 237: 480-498. https://doi.org/10.1016/j.epsl.2005.07.009

Panedile 2021. Hydropower: Los Caracoles: San Juan. https://en.panedile.com/caracolesen/

Pigati, J.S., Lifton, N.A., Timothy Jull, A.J., & Quade, J. 2010. A Simplified In Situ Cosmogenic ^{14}C Extraction System. *Radiocarbon,* 52(3): 1236-1243. https://doi.org/10.1017/S0033822200046324

Organismo Regulador de Seguridad de Presas (ORSEP). 2021. Registro de presas fiscalizadas. https://www.argentina.gob.ar/orsep/registro-de-presas-fiscalizadas

Pepin, E., Carretier, S., Hérail, G., Regard, V., Charrier, R., Farias, M., Garcia, V., & Giambiagi, L. 2013. Pleistocene landscape entrenchment: a geomorphological mountain to foreland field case, the Las Tunas system, Argentina. *Basin Research*, 25: 613-637. https://doi.org/10.1111/bre.12019

Rivera, J.A., Penalba, O.C., Villalba, R., & Araneo, D.C. 2017. Spatio-Temporal Patterns of the 2010-2015 Hydrological Drought across the Central Andes, Argentina. *Water*, 9(9): 652. https://doi.org/10.3390/w9090652

RGI Consortium. 2017. Randolph Glacier Inventory – A Dataset of Global Glacier Outlines: Version 6.0: Technical Report, Global Land Ice Measurements from Space, Colorado, USA. Digital Media. https://doi.org/10.7265/N5-RGI-60

Sabo, J.L., Sinha, T., Bowling, L.C., Schoups, G.H.W., Wallender, W.W., Campana, M.E., et al. 2010. Reclaiming freshwater sustainability in the Cadillac Desert. *Proceedings of the National Academy of Sciences of the United States of America*, 107: 21263-21270. https://doi.org/10.1073/pnas.1009734108

Sass, O. 2006. Determination of the internal structure of alpine talus deposits using different geophysical methods (Lechtaler Alps, Austria). *Geomorphology*, 80(1-2): 45-58. https://doi.org/10.1016/j.geomorph.2005.09.006

Snyder, N.P., Rubin, D.M., Alpers, C.N., Childs, J.R., Curtis, J.A., Flint, L.E., & Wright, S.A. 2004. Estimating accumulation rates and physical properties of sediment behind a dam: Englebright Lake, Yuba River, northern California. *Water Resources Research*, 40: W11301. https://doi.org/10.1029/2004WR003279

Tulenko, J.P., Caffee, W., Schweinsberg, A.D., Briner, J.P., & Leonard, E.M. 2020. Delayed and rapid deglaciation of alpine valleys in the Sawatch Range, southern Rocky Mountains, USA. *Geochronology*, 2: 245-255. https://doi.org/10.5194/gchron-2-245-2020

Val, P., Venerdini, A.L., Ouimet, W., Alvaredo, P., & Hoke, G.D. 2018. Tectonic control of erosion in the southern Central Andes. *Earth and Planetary Science Letters*, 482: 160-170. https://doi.org/10.1016/j.epsl.2017.11.004

Von Blanckenburg, F. 2005. The control mechanisms of erosion and weathering at basin scale from cosmogenic nuclides in river sediment. *Earth and Planetary Science Letters*, 237: 462-479. https://doi.org/10.1016/j.epsl.2005.06.030

Wittman, H., von Blanckenburg F., Maurice, L., Guyot, J., Filizola, N., & Kubik, P.W. 2011. Sediment production and delivery in the Amazon Basin quantified by in-situ produced cosmogenic nuclides and recent river loads. *GSA Bulletin*, 123(5-6): 934-950. https://doi.org/10.1130/B30317.1

JOHN R. SLOSSON

Syracuse University, Department of Earth and Environmental Sciences
204 Heroy Geology Laboratory, Syracuse, New York 13244

EDUCATION

J.D. 2009	University of Virginia School of Law, Charlottesville, Virginia
B.A. 2006	Economics, with Distinction, University of Virginia, Charlottesville, Virginia

POSITIONS HELD

2020	Part-Time Instructor, Syracuse University Syracuse, New York
2009-2014	Associate, Cadwalader, Wickersham & Taft, LLP New York, New York
2008	Summer Associate, Cadwalader, Wickersham & Taft, LLP New York, New York
2007	Intern, The Honorable Judge R. Terrence Ney, Fairfax Circuit Court Fairfax, Virginia

HONORS AND AWARDS

2021	Syracuse Univ. Dept. of Earth & Envtl. Sciences Student Publication Award
2021	Syracuse Univ. EMPOWER Emerging Interdisciplinary Research Grant
2020	Syracuse Univ. Research Excellence Doctoral Funding Fellowship
2019	American Alpine Club Live Your Dream Grant
2017-2018	National Science Foundation INTERN Award
2017	Geological Society of America John T. and Carol G. McGill Research Award
2017	Syracuse Univ. Dept. of Earth & Envtl. Sciences John J. Prucha Research Grant
2016-2017	Syracuse Univ. EMPOWER Fellowship
2006	Phi Beta Kappa

TEACHING EXPERIENCE

2020	Instructor of Record, Climate Change: Past and Present, Syracuse University
2019	Instructor of Record, Water and Our Environment, Syracuse University
2020	Teaching Assistant, Climate Change: Past and Present, Syracuse University
2019	Teaching Assistant, Oceanography, Syracuse University
2018	Teaching Assistant, Earth Systems Science, Syracuse University

PUBLICATIONS

Slosson J, Lautz L and Beltran J. 2021. Chloride load dynamics along channelized and intact reaches in a northeastern United States urban headwater stream. Environmental Research Letters, 16: 025001. https://doi.org/10.1088/1748-9326/abd8ab

Slosson J, Kelleher C and Hoke G. 2021. Contrasting impacts of a hotter and drier future on streamflow and catchment scale sediment flux in the High Andes. In review.

Beltran J, Lautz L and **Slosson J**. 2021. The impact of stream-groundwater exchange on seasonal nitrate loads in an urban stream. In review.

CONFERENCE ABSTRACTS

Slosson J, Kelleher C and Hoke G. 2020. The impact of increased aridity on catchment scale sediment flux in the Andes Mountains of Argentina and Chile. American Geophysical Union Fall Meeting. Oral Presentation.

Slosson J, Lautz L and Beltran J. 2019. Groundwater storage of seasonally-applied road salt in an urban watershed. American Geophysical Union Fall Meeting. Poster Presentation.

Beltran J, Lautz L and **Slosson J**. 2019. The impact of stream-groundwater exchange on seasonal nitrate uptake dynamics in an urban stream. American Geophysical Union Fall Meeting. Poster Presentation.

Slosson J and Hoke G. 2018. Stream gauge data and cosmogenic radionuclides as tools for calculating the useful lifespan of reservoirs in the Argentine Andes. American Geophysical Union Fall Meeting. Poster Presentation.

Campbell A, Millard G, Umutoniwase N, **Slosson J**, Millard S, Yang Y, Habimana E, Scholz C, Junium, Lautz L, Driscoll C, Nsabimana A, Nyiragatare A and Valens H. 2018. Collaborative international geosciences field course builds transferable skills and broader global perspectives. American Geophysical Union Fall Meeting. Poster Presentation.

Millard G, Campbell A, Hategekimana F, **Slosson J**, Millard S, Yang Y, Habimana E, Scholz C, Junium C, Lautz L, Driscoll C, Nsabimana A, Nyiragatare A and Valens H. 2018. Leveraging established research sites for developing multinational field methods course. American Geophysical Union Fall Meeting. Poster Presentation.

Slosson J and Hoke G. 2018. Using Stream Gauge Data and Cosmogenic Radionuclides to Calculate Sediment Flux in the Eastern Argentine Andes over Multiple Timescales. Binghamton Geomorphology Symposium. Poster presentation.

SELECTED PROFESSIONAL SERVICE

2021	Reviewer, Hydrogeology Journal
2019	Faculty Search Committee Student Co-Representative, Department of Earth and Environmental Sciences, Syracuse, New York
2017-2018	Volunteer, United States Geological Survey, New York Water Science Center Ithaca, New York

2017-2018	Senator, Syracuse University Senate, Syracuse, New York
2008-2009	Articles Editor, Virginia Tax Review, University of Virginia School of Law, Charlottesville, Virginia
2006-2008	Counselor, University Judiciary Committee, University of Virginia, Charlottesville, Virginia
2005-2006	Student Advisory Committee Vice-Chair, State Council on Higher Education for Virginia, Richmond, Virginia
2005-2006	Legislative Affairs Committee Chair, Student Council, University of Virginia, Charlottesville, Virginia

WORKSHOPS

2020	Alan Alda Center Science Communication Experience
2020	CUAHSI-iSWGR Snow Measurement Field School
2018	Syracuse University EMPOWER Rwanda Lake Kivu Training Program

SKILLS

Software: ArcGIS • MATLAB • Visual MODFLOW • Adobe Illustrator • Lexis/Westlaw

Laboratory Skills: Dionex ICS-2000 ion chromatograph • Quartz purification for cosmogenic nuclide accelerator mass spectrometry analysis

Field Equipment: Federal snow sampler • GPS snow depth probe • YSI EXO2 multiparameter sonde • YSI handheld acoustic doppler velocimeter • Sontek IQ velocity profiler

PROFESSIONAL MEMBERSHIPS

2009-Present	New York State Bar (admitted to practice)
2016-Present	American Geophysical Union
2016-Present	Geological Society of America